NASA CONTRACTOR REPORT

MEASUREMENT OF NON-CONTINUUM AND TURBULENCE EFFECTS ON SUBSONIC SPHERE DRAG

by Neil A. Zarin

Prepared by
UNIVERSITY OF MICHIGAN
Ann Arbor, Mich.
for Lewis Research Center

NATIONAL AERONAUTICS AND SPACE ADMINISTRATION • WASHINGTON, D. C. • JUNE 1970

1. Report No.	2. Government Accession No.	3. Recipient's Catalog No.
NASA CR-1585		

4. Title and Subtitle	5. Report Date
MEASUREMENT OF NON-CONTINUUM AND TURBULENCE EFFECTS ON SUBSONIC SPHERE DRAG	June 1970
	6. Performing Organization Code
7. Author(s)	8. Performing Organization Report No.
Neil A. Zarin	None
9. Performing Organization Name and Address	10. Work Unit No.
University of Michigan Ann Arbor, Michigan	11. Contract or Grant No. NGR 23-005-003
	13. Type of Report and Period Covered
12. Sponsoring Agency Name and Address	Contractor Report
National Aeronautics and Space Administration Washington, D.C. 20546	14. Sponsoring Agency Code

15. Supplementary Notes

16. Abstract

The drag of spheres, at Mach numbers from 0.10 to 0.57, Reynolds numbers ranging from 40 to 5000, Knudsen numbers as high as 0.060, and turbulence intensities up to 13% was measured in a continuous wind tunnel utilizing a magnetic suspension system. Stainless steel ball bearings having diameters of from 1 mm to 1/4 in. were used as models. The effects of free-stream turbulence, compressibility, and gas rarefaction were observed and compared with existing data wherever possible.

17. Key Words (Suggested by Author(s))	18. Distribution Statement
Sphere drag coefficient Free-stream turbulence Compressibility Gas rarefaction	Unclassified - unlimited

19. Security Classif. (of this report)	20. Security Classif. (of this page)	21. No. of Pages	22. Price*
Unclassified	Unclassified	139	$3.00

*For sale by the Clearinghouse for Federal Scientific and Technical Information
Springfield, Virginia 22151

TABLE OF CONTENTS

LIST OF FIGURES

SUMMARY

The purpose of the present work has been to measure sphere drag under conditions where gas rarefaction, compressibility, and turbulence must be taken into account. A small, vertical, subsonic wind tunnel incorporating a magnetic suspension system has been utilized for this research. With this apparatus, spheres of varying sizes were suspended without support interference; and the drag force on them was measured. Density, Mach number, and turbulence levels were easily varied in the tunnel. Drag data at Reynolds numbers (Re) ranging from 40 to 5000, Mach numbers (M) of from 0.10 to 0.57, Knudsen numbers as high as 0.060, and turbulence intensities up to 13% were attained with the present experimental apparatus. Turbulence is generated either by removing screens from the tunnel inlet section or by placing grids in the test section very close to the spheres. The intensity, spectra, and scales of the turbulence are measured with a hot-wire anemometer. Stainless steel ball bearings having diameters of from 1 mm to 1/4 in. were used as models.

The present experimental techniques have been verified by drag measurements at low turbulence levels and Knudsen numbers in the continuum and near-continuum regimes. The small differences between

the present data and the standard drag curve are attributed to low, but non-negligible, levels of turbulence which exist in the tunnel flow and to compressibility effects.

Sphere drag measurements taken with moderate (0. 4 to 3. 3%) levels of turbulence and scales of the order of or greater than the sphere diameters show that turbulence of these levels and scales produces significant drag increases for Reynolds numbers between 200 and 800. The drag coefficient increases approximately linearly with turbulence level in this range of Re. The data indicate that for a given turbulence level the percentage drag rise due to turbulence decreases with decreasing Re; the C_D increase approaches zero for $Re \leq 100$.

For sphere drag data obtained at turbulence of from 3 to 13%, turbulence scales of the order of or smaller than the sphere diameter, and Reynolds numbers of from 600 to 5000, a very pronounced effect of sphere diameter is evident. At a given Re, C_D increases monotonically with inverse sphere diameter 1/d. Reasons for this behavior are discussed.

The Reynolds numbers at which certain phenomena take place in the sphere flow field are lowered by the presence of free stream turbulence. At moderate turbulence levels, lateral motions of the sphere associated with the oscillating separated region and asymmetric vortex shedding first occur at lower values of Re than in low turbulence streams. At higher turbulence levels, the dip and rise which are present in the

standard drag curve in the range $10^3 < Re < 10^5$ are observed over a much narrower and lower Reynolds number range. The similarity in shape of the present C_D -Re curves to that of the standard drag curve suggests similar flow phenomena.

Present data for $40 \leq Re \leq 200$ and $0.17 \leq M \leq 0.57$ exhibit pronounced non-continuum and compressibility effects. These data are compared with empirical relations and other experimental data found in the literature.

NOMENCLATURE

a	empirically determined constant
a_i	inside radius of magnetic coil
a_o	outside radius of magnetic coil
A	empirically derived constant; also cross-sectional area of sphere
b	empirically derived constant
B	empirically derived constant
B_i	induced flux density in a body
c	empirically derived constant
c_p	specific heat at constant pressure
c_v	specific heat at constant volume
C	empirically derived constant
C_D	drag coefficient, D/q A
C_{D_o}	drag coefficient with zero turbulence
C_p	pressure coefficient, p/q
d	sphere diameter
D	drag force
F_{drag}	drag force
F_z	axial magnetic force
$F(n)$	turbulence spectrum
$g(Re)$	devised functional relation
H_z	magnetic field strength in axial direction
$h(M)$	devised functional relation
I	gradient coil current needed to suspend sphere, thread, weights
I_o	gradient coil current needed to suspend sphere
I_{flow}	gradient coil current with flow
$I_{no\text{-}flow}$	gradient coil current without flow

Kn	Knudsen number, λ/L
ℓ	coil height
L	Eulerian scale of turbulence in the y direction; also characteristic body length
L_x	integral scale in stream direction
M	Mach number; also mesh size
$\mathcal{m}$	molecular speed ratio based on the mean random molecular speed
n	frequency
$N_{Re_c}{}^*$	hypercritical Reynolds number
N_{Re_T}	transcritical Reynolds number
p	static pressure
p_o	stagnation pressure
Δp	differential between stagnation and static pressures
q	dynamic pressure, $(1/2)\ \rho\ U^2$
r	distance from sphere center to a point in flow field
r_o	cylinder radius
R_{cold}	resistance of hot wire without current
R_{hot}	resistance of hot wire with current
Re	Reynolds number, Ud/ν
Re_1	Reynolds number based on conditions behind a normal shock
Re_{lc}	lower critical Reynolds number
Re_M	Reynolds number based on mesh size
Re_{uc}	upper critical Reynolds number
R_x	correlation function
T	stagnation temperature
T_g	gas temperature
T_p	particle temperature

u	fluctuating component of velocity in stream direction
u'	root mean square of the turbulent fluctuations
U	mean flow velocity
v	fluctuating component of velocity
V	volume
w	fluctuating component of velocity
W	weight of sphere, thread, and weights
W_o	weight of sphere
x	distance in streamwise direction; also distance from grid to center of sphere
Δx	strip chart recorder reading for gradient coil current with flow
Δx_o	strip chart recorder reading for gradient coil current without flow
z	coordinate in axial direction
Δz	spacing between coils
α	angle between rear stagnation point and separation circle
γ	ratio of specific heats of gas, c_p/c_v
δ	boundary layer thickness
ϵ	dissipation
λ	molecular mean free path
μ	fluid viscosity
ν	kinematic viscosity
ρ	gas density
σ	dummy variable
ϕ	angle between magnetization vector and solenoid axis

Subscripts and Superscripts

$\bar{(\ )}$	mean value
$(\ )_{comp}$	compressible value
$(\ )_{inc}$	incompressible value

I. INTRODUCTION

Many problems of practical interest require the knowledge of the drag force exerted by a fluid medium upon a particle moving through it. The flight of a weather balloon, the dispersion of aerosol sprays, and the course of pollutents in the air and water are a few examples.

The rapid development of rocket technology in recent years has further emphasized the need for information on particle drag. In advanced solid propellant rockets, metallic constituents are added to the fuel in order to provide increased specific impulse. However, only as much as 90% of the theoretically predicted specific impulse may be realized because of condensed particles of metal oxides or fluorides formed during the combustion process lagging behind the gaseous nozzle flow. For all practical purposes these particles may be considered spherical. In order to assess the influence of these particles it is essential to know the drag characteristics under a variety of conditions.

For a single, smooth sphere in steady, isothermal, non-turbulent, incompressible, continuum flow of an infinite extent, the drag coefficient is well known, having been established by many experiments for the most part. Under the above conditions drag has been found to be a function of Reynolds number alone. The plot of the drag coefficient versus Reynolds number is called the "standard drag curve."

In a rocket nozzle, as in other areas of practical interest, conditions differ greatly from the idealized ones. Carlson and Hoglund[1] and Crowe[2] have computed the gas dynamic trajectories, in terms of relative Mach number and relative Reynolds number*, of typical particles in typical rocket motors (see Fig. 1). These calculations show that large portions of the trajectories lie in flow regimes characterized by non-continuum effects. Parts of these regions are also influenced by compressibility. Both non-continuum and compressibility effects cause drag coefficients to differ from those predicted by the standard drag curve. To date, little particle drag data exist for the rarefied flow regimes of importance to the rocket nozzle problem. A few empirical expressions based on available experimental drag data have been formulated in order to estimate drag; however, additional reliable experimental data are required to verify and, where needed, modify these expressions.

In addition to gas rarefaction and compressibility, free stream turbulence may cause large variations in drag coefficients from those values given by the standard drag curve. Turbulence may strongly influence the Reynolds number at which the sphere boundary layer

---

*The relative Mach number and relative Reynolds number of a particle are based on the relative velocity between the particle and the gaseous nozzle flow.

undergoes transition from laminar to turbulent. It can also affect the drag both above and below this transition point. Some studies have been made of the effects of turbulence on transition and on the drag coefficient above transition[3, 4]. But the results of these tests have not been duplicated by other experimenters. Below the transition Reynolds number, turbulence has been observed to cause a moderate increase in the drag coefficient over that found in non-turbulent flow, but investigation in this area has not been particularly systematic. Thus, there is a need for additional experimental work on the effects of turbulence on sphere drag.

The purpose of the present work is to examine sphere drag under non-idealized conditions where gas rarefaction, compressibility, and turbulence must be taken into account. This research has been carried out in a small, vertical, subsonic wind tunnel, which was designed particularly for this work. The tunnel incorporates a magnetic suspension system capable of suspending spheres of varying sizes and accurately measuring the drag force on them. Density, Mach number, and turbulence levels can be easily varied in the tunnel.

Part II of this report gives background information. The flow field about a sphere and its variation with Reynolds number; analytical and numerical attempts to describe this flow field; the variation of sphere drag with Reynold number in "standard" flow; and the effects of turbulence, compressibility, and rarefaction on sphere drag are discussed.

Part III describes the experimental apparatus and procedures used in this investigation. The wind tunnel, magnetic suspension system, turbulence generation, instrumentation, models, operation procedure, and methods of data reduction are described. The results of this investigation are presented in Part IV and a summary of the conclusions which can be drawn from this research is given in Part V.

II. BACKGROUND TO THE RESEARCH

A. INTRODUCTION

The drag on spheres has been studied for more than two and a half centuries. The first recorded measurements were made in the early eighteenth century by Sir Isaac Newton, who determined fall velocities of spheres dropped both from the dome of St. Paul's Cathedral in London and in columns of water[5]. Numerous sphere drag measurements have been made since these initial ones. Many of these have been noted by Torobin and Gauvin in their comprehensive series of review articles on the fundamental aspects of solids-gas flow[6-11]. In spite of all the work in this area to date, there are many facets which are worthy of further investigation.

The sphere flow field and its variation with Reynolds number are extremely complicated. The mathematical description of this flow phenomenon is very difficult and has been effected only in a few limited situtations. As a result, most current knowledge of flow around spheres has come from experimental studies. Not all of the investigators are in complete agreement. Differences in measurements arise because of the sensitivity of the flow to such factors as surface roughness, free stream turbulence, and wall interference. In situations of

practical interest, these factors may play a dominant role and the actual drag coefficients may vary by an order of magnitude from those predicted by the "standard drag curve."

The discussion in Part II provides a background with which the reader may better interpret and evaluate the significance of the present research.

B. THE SPHERE FLOW FIELD

This section describes the changing sphere flow field with increasing Reynolds number. The results of many experimental investigations, not always in complete agreement, are discussed in brief. More comprehensive treatments of the sphere flow field can be found in the works of Roos[12] and Torobin and Gauvin[7].

For $Re < 0.1$, the flow near the sphere is essentially symmetrical fore and aft. The ratio of inertial to viscous forces is of the order of Ur/ν, where r is the distance from the sphere center to a point in the flow field[13]. Thus, while viscous forces dominate near the sphere, inertial forces increase in importance at large values of r.

For $0.1 < Re < 24$, inertial effects increase in importance near the sphere and the streamline pattern is no longer symmetrical fore and aft[14].

At Re $\approx$ 24, Taneda[15] reports the appearance of a small closed region of separated flow at the rear stagnation point, although investigators disagree as to the value of Re at which this occurs. Differences in free-stream turbulence, means of sphere support, and method of flow visualization can cause variation in the Reynolds number where separation is first observed. The separation is due to the inability of the fluid adjacent to the surface to flow to the rear stagnation point against the adverse pressure gradient and the retarding effect of surface friction. As the Reynolds number increases, a fixed ring vortex grows within the separation bubble and its stability decreases. At Re = 130 the downstream part of the separated region begins to oscillate[15]. This oscillation becomes stronger as Re increases up to a value of about 210, but the laminar wake downstream of the wake stagnation point remains stable.

From $210 < Re < 270$, an asymmetrical separation bubble with a double laminar wake has been observed[16]. Taneda[15], using a flow visualization technique, determined the dimensions of the wake and its development for the range $5 < Re < 300$. The results, which are important for later discussions on the effects of turbulence, are given in Fig. 2.

Discrete vortex loops are shed periodically from opposite sides of the separation bubble in the range $290 < Re < 700$. The Reynolds number at which this first occurs is referred to as the "lower critical

Reynolds number (Re_{lc})." Some investigators feel that Re_{lc} is as low as 200 and others place it at 1000 (see Ref. 17 and 18, respectively). A new ring forms as the unstable one detaches so that there is a periodicity in the wake in this Reynolds number range. Fluctuations in the drag coefficient which are associated with this periodic growth and detachment of vortex rings have been noted by Schmidt[19] and Liebster[20].

The asymmetry of the wake above Re = 210 produces transverse forces on the sphere which cause freely falling or rising spheres to follow zig-zag or helical paths. This phenomenon has been noted by several authors[16, 18-20]. Roos[12] has measured these transverse forces with a strain gage force balance in a tow tank and has found peak-to-peak force coefficients as high as 0.105 at Re $\approx$ 400. Sivier[21] reported that his magnetically suspended spheres underwent large lateral oscillations in the range $300 < Re < 600$, which made drag measurement extremely difficult. He noted that increased levels of free stream turbulence caused the Re_{lc} to occur at values as low as 150.

As Reynolds number is increased above 700, the vortex loops are shed with increasing frequency[16].

In the range $700 < Re < 10,000$, a helical pattern in the wake has been noted by several investigators[22-25] and spheres have been observed falling in spiral paths. These helical wakes may occur at even

higher Reynolds numbers. Hot wire measurements in sphere wakes by Kendall[23] and Winny[24] show fluctuations at two discrete frequencies indicating two types of instabilities. One leads to the overall spiraling motion of the wake while the other produces a higher frequency local rolling up of the separated shear layer into vortices. Comments on similar processes occurring in circular cylinder wakes are given in Ref. 26.

For Reynolds numbers in the range of from 10,000 to 200,000 the vortex loop shedding becomes nearly a continuous process and the wake assumes a turbulent appearance. Fluctuations corresponding to the shedding of vorticity clumps still occur in this regime.

In the range $200,000 < Re < 400,000$, the character of the flow about the sphere changes considerably. The sharp dip in the C_D versus Re curve gives evidence of this changing flow field. The value of Reynolds number at which the steeply falling portion of this curve intersects the C_D value of 0.3 has been defined, by convention, as "the critical Reynolds number."

To distinguish it from the lower critical Reynolds number where vortex shedding first occurs, it will be termed here the "upper critical Reynolds number" (Re_{uc}). The classical description of the flow below and above Re_{uc} is roughly as follows: at subcritical Reynolds numbers the separation occurs on the front of the sphere. With increasing

Reynolds number, transition in the boundary layer moves ahead of the laminar separation point, the now turbulent boundary layer can then withstand a greater pressure rise, and separation moves to the rear of the sphere with a consequent decrease in the drag coefficient. Measurements by Roshko[27], Son and Hanratty[28], and Achenbach[29] on circular cylinders at high Reynolds numbers have given evidence that a slightly modified description is necessary: at subcritical Reynolds numbers the separation is laminar. In the supercritical range there is a laminar separation bubble followed by reattachment and turbulent separation. In the transcritical range the separation is purely turbulent with no separation bubble.

The location of the separation circle varies with Reynolds number, and the value of the drag coefficient is strongly dependent upon it. Taneda[15] has studied the separation position and has found the angle α between the rear stagnation point and the separation circle to increase steadily from a value of zero at Re = 24 to 72^{o} at Re = 450. Garner[30], using soluble spheres and assuming that the separation circle is indicated by the location of minimum mass loss, has found higher values of α than Taneda below Re = 100. Above this value their results are similar. Garner's data show a constant value of α above Re = 500. This result is contradicted by the work of Ermisch[31], who has found, using pressure measurements at the sphere surface, that α increases

steadily from Re = 800 to 26,000. By measuring skin friction on a circular cylinder, Son and Hanratty[28] have found α to increase slowly in the range $5 \times 10^3 < Re < 10^5$. This variation in α may account for the gradual increase in C_D in this range of Reynolds number, although Schiller and Linke[32] suggest that it may be attributed to a moving forward of the point of transition from laminar to turbulent in the separated shear layer. By stimulating the boundary layer of a cylinder with a very fine wire, they have caused the transition point in the separated layer to move closer to the body. This caused a lower base pressure and, hence, an increased drag coefficient.

In summary, the character of the flow field about a sphere as a function of Reynolds number is fairly well known. However, questions remain in the following two areas: the exact Reynolds number where a separated region starts to form and the variation of separation location with Reynolds number.

C. ANALYTICAL FLOW FIELD DESCRIPTIONS

The analytical description of the sphere flow field and the prediction of drag force have not yet been done for a wide range of flow conditions. Closed form solutions are available for only two special cases: (1) Stokes' flow and (2) free-molecule flow. A very good survey of the analytical work on the sphere flow field and drag force up to 1959 is given by Torobin and Gauvin[6]. A brief summary of the work to date is given in this section.

The Stokes' solution for a very slowly moving sphere is obtained by neglecting the inertial terms in the Navier-Stokes equations, reducing them to easily solvable forms. The drag coefficient obtained from the Stokes' solution is 24/Re. This value agrees very well with experimental results up to a Reynolds number of about 0.1. Above this value, the inertia terms become increasingly important and they may no longer be neglected.

Oseen[33] obtained a linear form of the Navier-Stokes equations by writing U + u for u and neglecting terms of the second order in u, v, and w only. A first approximation to Oseen's equations yields $C_D = (24/Re) + 4.5$ for the drag coefficient. Goldstein[34] has obtained a complete solution for the Oseen approximation yielding

$$C_D = \frac{24}{Re}\left(1 + \frac{3}{16}Re - \frac{19}{1280}Re^2 + \frac{71}{20480}Re^3 - \ldots\right)$$

for the drag coefficient. This agrees with experiments to within 1.5% up to a Reynolds number of about 0.90 (Ref. 35).

Kawaguti[36, 37] has obtained an approximate solution to the Navier-Stokes equations in the range $10 < Re < 80$ using the Galerkin method. This involves choosing an approximate form of the stream function made up of various trial functions with unknown parameters. These parameters are then evaluated by using the boundary conditions and a simplified form of the Navier-Stokes equations. Kawaguti's solution

gives drag coefficients which are in excellent agreement with experiments. He has also obtained a value of 51 for a lower critical Reynolds number by perturbing the equations and finding a Re above which the disturbance will increase and below which it will die out.

There have been some attempts to find numerical solutions to the Navier-Stokes equations at specific Reynolds numbers using finite difference techniques[14, 38]. Reasonably good agreement with experiment has been achieved up to Re = 100, but none of the solutions can predict the flow behavior in the near wake.

The flow about a sphere in free-molecule flow, where the molecular mean free path is greater than the sphere diameter, has been treated analytically, and a closed form solution has been obtained (see Ref. 39). The drag coefficients have been computed for the limiting cases of diffuse and specular reflection. In both cases, C_D approaches 2 asymptotically as the molecular speed ratio* increases.

Brooks and Reis[40] have obtained an expression for the drag coefficient of a cylinder at low speed ratios from the continuum to the free-molecule flow regime. Although their analysis includes several gross approximations, their results agree quite well with their experiments. The drag coefficient predicted by their analysis is

*The molecular speed ratio is the ratio of the speed of the object to the most probable molecular speed.

$$C_D = \frac{4}{\sqrt{3}} \frac{1}{\mathcal{M}} \left(1 - \frac{r_o}{\lambda} e^{r_o/\lambda} \int_{r_o/\lambda}^{\infty} \frac{e^{-\sigma}}{\sigma} \, d\sigma \right) + 1 \quad ,$$

where $\mathcal{M}$ is the molecular speed ratio based on the mean random molecular speed, r_o is the cylinder radius, λ is the molecular mean free path, and σ is a dummy variable. A plot of $\mathcal{M}(C_D - 1)$ versus r_o/λ is presented in Fig. 3. The curve for a sphere should be similar and recourse to this form shall be made later.

In summary, analytical and numerical approaches have been able to describe the flow about a sphere for a few very specific cases. Modern high speed computers and improved numerical techniques should extend the scope of these descriptions in the future.

D. SPHERE DRAG IN "STANDARD" FLOW

Many investigators have measured sphere drag using a variety of techniques. They have found that for a single smooth sphere in steady, non-turbulent, isothermal, incompressible, continuum flow of essentially infinite extent, the drag coefficient is a function of Reynolds number alone. A plot of C_D against Re is known as the "standard drag curve." In this section the variation of sphere drag with Reynolds number in "standard" flow will be discussed. Various empirical expressions for the drag coefficient which have been devised to fit available data in restricted Reynolds number ranges will also be noted.

The shape of the standard drag curve has been well determined experimentally for Reynolds numbers ranging from less than 10^{-2} to greater than 10^{6}. This curve is often given as a single line, as in Fig. 4, although one should note that it is simply a "best fit" curve through data which may have considerable scatter. Figure 5 depicts representative "classical" sphere drag data for Reynolds numbers between 10^{1} and 10^{4}. There is a relatively large amount of scatter despite very careful measurements taken under controlled laboratory conditions. Unfortunately, in most situations of practical interest, conditions are far from ideal; and one would expect that the standard drag curve would give only a rough estimate of the drag coefficients found in these cases.

Major contributors of sphere drag coefficient data used in developing the standard drag curve are Allen[41], Arnold[42], Wieselsberger[43], Bacon and Reid[44], Liebster and Schiller[45], Lunnon[18,46], Flachsbart[47], Schmiedel[48], and Millikan and Klein[49]. The results of these investigators have been confirmed by later workers such as Möller[22], Maxworthy[35], and Roos[12]. While this accounting is by no means a complete one, it does mention the more reliable and/or significant contributions to the evolution of the standard drag curve. For a detailed account of the sphere drag literature up to 1960, the reader is referred to the comprehensive work of Torobin and Gauvin[6].

For Reynolds numbers less than about 0.1, experimental drag coefficients agree very well with the Stokes' relation

$$C_D = \frac{24}{Re}$$

In this regime about 2/3 of the drag is due to skin friction and 1/3 is due to pressure or form drag. The inertial terms in the Navier-Stokes equations are negligible in this range.

For $0.1 < Re < 1$ inertial effects increase in importance and the drag coefficient is above that given by the Stokes' drag law. Here, the theoretical expression derived by Oseen[50]

$$C_D = \frac{24}{Re} + 4.5$$

matches the experimentally determined drag values quite well.

In the range $1 < Re < 5 \times 10^3$ the drag coefficient curve decreases more moderately with increasing Reynolds number, reaching a minimum value of about 0.38 at $Re = 5 \times 10^3$. This regime is characterized by the formation of a separated region at the rear of the sphere. The contribution of viscous forces to the total drag decreases in this range, while pressure forces become dominant.

The drag curve rises gradually from its minimum and levels out at a value of 0.47 at $Re = 10^5$. At a Reynolds number of approximately 3×10^5, (Re_{uc}), it drops sharply to a value of about 0.1 for reasons discussed earlier.

For Reynolds numbers above 3×10^5 the drag curve rises gradually. Data in this range are both scarce and disparate. More measurements with greater reliability are needed.

For convenience, several researchers have fitted empirical expressions to the available drag data. These give reasonably good predictions within limited ranges of Reynolds number. A few of these are presented below.

Klaichko[51] found the simple relation

$$C_D = \frac{24}{Re} + \frac{4}{Re^{1/3}}$$

to be reasonably accurate for $Re < 1000$. Putnam[52] has shown that this expression is easily integrated for trajectory calculations.

Schiller and Nauman[53] employed

$$C_D = (24/Re)(1 + 0.15\ Re^{0.687})$$

with good success for $Re \leq 700$, while Langmuir[54] used

$$C_D = (24/Re)(1 + 0.197\ Re^{0.63} + 0.0026\ Re^{1.38})$$

for $1 < Re < 100$.

E. EFFECTS OF TURBULENCE ON SPHERE DRAG

There are many situations of practical importance where the behavior of solid or liquid particles in a gas stream is influenced by turbulence. Because the effects of turbulence on the particle drag

coefficient can be extremely large, it is important that they be understood. Torobin and Gauvin[10], Sivier[21], and others have discussed this problem at great length. This section discusses the effects of turbulence on the flow over spheres. Its effects on cylinders are also discussed when such information adds to the understanding of the sphere problem.

Turbulence can affect the drag coefficient by strongly influencing the Reynolds number at which the sphere boundary layer undergoes transition from laminar to turbulent. It can also affect both subcritical and supercritical drag.

Dryden et al.[55], were the first to study the effects of turbulence on the upper critical Reynolds number Re_{uc} systematically. They found that Re_{uc} decreases monotonically with increasing turbulence intensity for levels up to 4.5%. Their data correlate more closely when Re_{uc} is plotted against $(u'/U)(d/L)^{1/5}$, where u' is the root-mean-square value of the turbulent fluctuations, d is the sphere diameter, and L is the Eulerian scale of turbulence in the y direction. This parameter was derived by Taylor[56], who suggested that the fluctuating pressure gradients which accompany free-stream turbulence are responsible for transition to turbulence.

Torobin and Gauvin[10] have determined the effect on Re_{uc} of relative turbulence intensities as high as 40% using a cocurrent turbulent

flow vertical wind tunnel with an injected particle and a radioactive tracer technique. They find that their data are best described by the relation $(Re_{uc})(u'/U)^2 = 45$. They relate this expression to a theory based on the assumption that transition will occur when the turbulent energy of an incident fluid element is equal to or greater than the viscous damping energy of a fluid element in the boundary layer. They find that an extrapolation of the Dryden data to high turbulence levels agrees with their theory.

In a recent paper, Clamen and Gauvin[4] extend the earlier work of Torobin and Gauvin to the supercritical regime. Their results are shown in Fig. 6. They find that the drag coefficient, after its sharp drop due to transition, rises steeply to a maximum and then drops off more gradually. Different levels of turbulence produce distinct C_D versus Re curves, all having similar shapes. The maxima occur at different Reynolds numbers. These maximum values of C_D increase with increasing turbulence intensity. The Reynolds numbers at which they occur decrease with increasing intensity. After reaching their maxima, the curves converge. The Reynolds number at which the sharply rising portion of the C_D-Re curve at constant intensity intersects the C_D value of 0.3 is defined as the "hypercritical Reynolds number" (N_{Re_c}*); and the Reynolds number at which the maximum in the curve occurs is termed the "transcritical Reynolds number"

(N_{Re_T}). For the range of turbulence intensities measured, Clamen and Gauvin find that $(u'/U)(N_{Re_c}{}^*) = 400$ and $(u'/U)(N_{Re_T}) = 1,040$ best express the relation between turbulence intensity and the hypercritical and transcritical Reynolds numbers, respectively. They find that for turbulence intensities of from 7 to 35% and for $N_{Re_c}{}^* < Re < 3 \times 10^4$, their data can be described to within 15% by the empirical expression:

$$C_D = [3990/(\log Re)^{6.10}] - [4.47 \times 10^5/(u'/U)^{0.97} Re^{1.80}] \quad .$$

The work of Clamen and Gauvin, as well as the earlier work from the same laboratory by Torobin and Gauvin, has not yet been independently verified and should be considered in that light.

Although there have been no detailed investigations of the sphere flow field in the supercritical regime, some deductions can be made from the C_D-Re curves obtained by Clamen and Gauvin and from the work by Roshko on cylinders referred to in Sec. II.B. Clamen and Gauvin suggest that the increase with intensity of the maximum values of C_D obtainable in the supercritical flow regime seen in their results may be associated with the increased vorticity in the wake in the presence of free-stream turbulence. This vorticity, they assert, reduces the extent of the near, or attached, wake by hastening the spatial return to free-stream conditions behind the particle. With the shortening

of the near wake, the main flow is required to close more sharply behind the sphere. A greater lateral pressure gradient is then needed to produce the increased curvature of the streamlines; and, since the ambient free-stream pressure is fixed, there must be a decrease in the pressure at the rear of the particle and, hence, an increased drag. Clamen and Gauvin assert that the decrease in their measured drag values with Reynolds number following the maxima probably reflects a decreasing value of skin friction coefficient with increasing Re, and the convergence of the curves for different turbulence levels brings out the lack of dependence of turbulent skin friction on turbulence intensity. They see a decrease in C_D from 1.5 to .5 with an order of magnitude change in Reynolds number. This is so large that it is improbable that much of it is due to a skin friction decrease. It is known that turbulent skin friction varies as $(Re)^{-1/5}$ (see Ref. 57). If all of the sphere drag were due to skin friction, there would be only about a 40% decrease in C_D with an order of magnitude change in Reynolds number. Roshko neglects skin friction altogether when he computes supercritical drag coefficients for cylinders by integrating their pressure distribution. However, his data are in fairly good agreement with those of Delany and Sorensen[58] which were obtained by force balance methods.

Much work remains to be done to explain the effects of turbulence and Reynolds number on the flow field in the supercritical regime.

In the subcritical range of Reynolds numbers, Sivier[21] reports that moderate ($\leq 8\%$) free-stream turbulence intensities produce a definite increase in C_D for Re $>$ 200, the increase growing with increasing Re. At Re $<$ 200, he has observed little or no change in C_D compared to the C_D's measured at lower turbulence intensities ($\simeq 1\%$). His measurements do not include the scale or spectra of the turbulence, and turbulence intensity was not varied over a very wide range.

In a study of the effects of turbulence on the drag of flat plates placed normal to the flow, Schubauer and Dryden[59] find a steady rise in drag coefficient with free-stream turbulence intensity over a range of from 1 to 3%. This drag rise can be caused only by an enhanced free-stream-wake interaction since the separation location is fixed and skin friction will not influence the plate drag.

Van der Hegge Zijnen[60] has measured the effects of turbulence levels up to 9.3% on the pressure distribution about a circular cylinder at Re = 20,100 and has found that the turbulence decreases the pressure on the rear portion of the cylinder and moves the separation point slightly rearward. The drag coefficient computed from the pressure distribution increases from 1.08 at a low turbulence level to 1.24 and 1.26 at levels of 4.7 and 9.3%, respectively. Van der Hegge Zijnen has not investigated the effects of turbulence scale on the pressure distribution, but he has noted a pronounced scale effect on the heat transfer. He finds that when Reynolds number and turbulence intensity

are kept constant, the heat transfer either increases or decreases with increasing scale ratio L_x/d; the heat transfer shows a maximum when L_x/d is about 1.5 to 1.6. He suggests that this may be due to a resonance which occurs when some "effective" frequency of the turbulence coincides with the frequency of the eddies shed off by the cylinder. When this "effective" frequency is proportional to U/L_x, these frequencies are equal for a constant ratio between the scale of turbulence and the cylinder diameter. Assuming that the resonance is with the energy containing eddies in the turbulent flow and that the turbulence is isotropic, Hinze[61] obtains a ratio of 1.2 which is of the same order as the value found experimentally.

The effects of very intense, free-stream vorticity on the flow field around a cylinder have been observed by Ahlborn[62]. He has photographed the flow about a circular cylinder with and without a grid placed upstream. He finds that when the grid is placed in the flow, the flow field about the cylinder changes drastically from one typical of fairly low Reynolds numbers to one characteristic of much higher Re. The boundary layer separates much further back on the sphere, and the wake is considerably shorter. Similar effects on the flow field about a sphere can be expected with turbulence of sufficient intensity.

In summary, the effects of turbulence on the critical Reynolds number have been determined. The effects on drag in the supercritical range of Reynolds numbers have, likewise, been observed,

although the explanation of these observations is uncertain. These observations have not been independently confirmed, however. In the subcritical range, drag measurements have not been particularly systematic. A moderate drag increase has been observed, but the effects of intensity and scale have not been determined. One phase of the present research has been performed in an attempt to fill this void.

F. NON-CONTINUUM AND COMPRESSIBILITY EFFECTS ON SPHERE DRAG

As mentioned in Part I, there are certain particle-gas flows where the effects of rarefaction and compressibility must be considered. In these cases it is important to know how the drag coefficient varies from that measured in incompressible continuum flow.

The usual measure of the degree of rarefaction is the Knudsen number Kn, which is defined as the ratio of the molecular mean free path of the gas to a characteristic length in the flow field. In some cases this length may be a characteristic dimension of a body immersed in a fluid, such as the diameter of a particle in a rocket exhaust. In others, the length may be the thickness of the boundary layer on an object. The division of gas dynamics into various regimes based on characteristic ranges of values of an appropriate Knudsen number has been proposed by several authors (Ref. 39). The terms

"continuum flow", "slip flow", "transition flow", and "free molecule flow" refer to regimes in which, generally speaking, the density levels are, respectively, ordinary, slightly rarefied, moderately rarefied, and highly rarefied.

For flows where the significant length is the characteristic length of a body, the Knudsen number can be approximated by the ratio of the Mach number to the Reynolds number, M/Re. For flows where a boundary layer exists in the usual sense, the characteristic dimension of importance is the boundary layer thickness δ. Since for a laminar boundary layer

$$\frac{\delta}{L} \sim \frac{1}{\sqrt{Re}} \quad ,$$

the corresponding Knudsen number is given by

$$Kn \sim \frac{M}{\sqrt{Re}} \quad .$$

Continuum flow for large Reynolds numbers occurs for $M/\sqrt{Re} \ll 1$. On the other hand, for very small Reynolds numbers, where the body length is the characteristic dimension, $M/Re \ll 1$ is the criterion for continuum flow. As the flow becomes more rarefied, the layer of gas immediately adjacent to a solid surface is no longer at rest but has a finite tangential velocity. The term "slip flow" is thus appropriate for flows of small, but not negligible, Knudsen number. Although the change from the continuum to the slip

regime is gradual, the slip flow regime is generally defined by the following limits:

$$0.01 < \frac{M}{\sqrt{Re}} < 0.1 \quad , \quad Re > 1$$

$$0.01 < \frac{M}{Re} < 0.1 \quad , \quad Re < 1 \quad .$$

For Reynolds numbers of the order of 100 or less, viscous effects on the sphere flow field will be quite large. For $Re > 100$, the above definition of the slip flow regime indicates that for slip flow the Mach number must be in a range where compressibility effects become important ($M > 0.1$). Thus, slip will occur in coincidence with either strong viscous or compressibility effects. For this reason, the effects of rarefaction and compressibility should be considered together.

For extremely rarefied flows, the mean free path is much greater than a characteristic body dimension. Under these circumstances, no boundary layer is formed and molecules reemitted from the body do not collide with free stream molecules until far from the body. Here the flow phenomena are governed mostly by molecule-surface interactions. This regime is called "free-molecule flow" and is generally defined by

$$\frac{M}{Re} > 3 \quad .$$

The transition regime is that range between the slip and free-molecule ranges where surface collisions and free-stream molecular collisions are of roughly equal importance, and analysis becomes quite difficult. Most of the available information in this range is empirical.

The effects of compressibility on sphere drag in laminar, continuum flow, for $10^4 < Re < 10^5$, are shown in Fig. 7. In the subsonic range, below the critical Mach number*, there is a gradual increase of the drag coefficient with increasing Mach number. This increase is believed due to increasing forebody and base pressure drags which counteract a slightly decreasing skin friction drag[63]. Above the critical Mach number there is a sharp drag increase due to the localized shock waves causing earlier flow separation and, hence, increased base drag[64].

Following the sharp drag rise there is a slight dip at about M = 0.8. This dip is most likely due to "a favorable interaction between the local supersonic field of flow existing at and behind the location of the cylinder's [sphere's] maximum thickness, and the flow pattern within its wake"[63]. Following this dip, the drag coefficient rises to

---

*The critical Mach number is defined as that free-stream Mach number at which regions of sonic and/or supersonic flow first appear in the flow field.

maximum of about 1.0 at a Mach number between 1.5 and 2.0. At higher Mach numbers it decreases slowly to its hypersonic asymptote of 0.92. At hypersonic Mach numbers, most of the drag is due to the forebody pressure distribution[63].

Recent ballistic range tests with spheres by Goin and Lawrence[65] indicate effects of compressibility at Mach numbers as low as 0.20, particularly at Reynolds numbers above 10^3.

The effects of rarefaction begin to occur when the mean free path is of the order of the boundary layer thickness on the body. Physically, a velocity slip condition exists at the body surface. For wedges or flat plates, skin friction will be reduced by a factor of the order of $M/\sqrt{Re}$ (Ref. 66). On spheres, a similar skin friction reduction is likely. The importance of this reduction will, of course, vary with Reynolds number since the contribution of friction drag to total drag also varies.

A second effect of velocity slip may be more important than the skin friction reduction. At Reynolds numbers where the flow is separated from the rearward face of the sphere, the velocity slip condition may lead to a boundary layer which can carry further against the adverse pressure gradient at the rear of the sphere, delaying separation and reducing the base drag.

Experimental data in the incompressible rarefied regime are extremely limited. Millikan[67] has measured the drag coefficients of small oil drops at Reynolds numbers in the Stokes' flow range. His Knudsen numbers are in the range from 0.25 to 67; that is, from the transition to the free molecule flow regimes. He has obtained an empirical correction formula to the Stokes' drag law which is given by

$$F_{drag} = 3\pi \mu \, dU \Big/ \left[1 + \frac{\lambda}{d}\left(A + B\, e^{-C(d/\lambda)}\right)\right] ,$$

where μ is the fluid viscosity; d is the sphere diameter; U is the particle velocity; λ is the mean free path; and A, B, and C are empirically determined constants. For the range $.25 < \lambda/d < 67$, he found $A = 1.728$, $B = 0.580$, and $C = 0.625$. Millikan's formula has been used in some empirical sphere drag expressions which will be discussed later.

Goin and Lawrence[65], in their work mentioned above, report drag measurements in the ranges $.20 < M < .98$ and $200 < Re < 10,000$. Some of these results fall in the slip flow regime, but the overriding effects of compressibility make it difficult to determine any rarefaction effect. Goin and Lawrence compare their data to those of Lunnon[18] and Wieselsberger[43] and find that their $M = .20$ curve differs from the earlier works by a maximum of 5%. It should be noted that Goin and Lawrence indicate Wieselsberger's data with a single curve extending down to a Reynolds number of about 200. Wieselsberger's actual data points extend down to a Reynolds number of only 790, and they have greater than 5% scatter.

It is clear that more work is necessary to obtain drag coefficient data in incompressible rarefied flow at Reynolds numbers above the Stokes' flow regime.

In the supersonic, rarefied flow regime there are only limited experimental data available. Kane[68] has obtained experimental values for C_D over the range $2.05 < M < 2.81$ and $15 < Re < 768$. He finds no effect of Mach number in this range and proposes an empirical formula for C_D in the form:

$$C_D = \left(0.97 + \frac{1.32}{\sqrt{Re_1}}\right)\left(1 + \frac{1.0}{\sqrt{Re_1}}\right)^2 ,$$

where Re_1 is the Reynolds number based on the sphere diameter and flow conditions behind a normal shock. Additional data in the supersonic, rarefied regime have been provided by Aroesty[69], Skreekanth[70], and May and Witt[71], and others. They are in substantial agreement with those of Kane. The effect of wall-to-free-stream temperature ratio on rarefied sphere drag has also been studied[72]. In Fig. H, 17a of Ref. 39, Schaaf and Chambré compare Kane's data and empirical relation with Millikan's empirical formula for incompressible ($M \cong 0$), rarefied flow, presented above. This comparison shows that at Reynolds numbers above 60, where pressure drag is relatively more important than skin friction drag, the compressible drag is

substantially greater (almost double at Re = 400) than the incompressible prediction. At Re $<$ 60, the effects of rarefaction on the viscous drag have presumably become sufficient to drop the supersonic value below the incompressible value.

At least two empirical relations based on available experimental drag data have been formulated in order to estimate drag in flow regimes where experimental data are not available. One such relation which has been suggested by Carlson and Hoglund[1] is

$$C_D = \frac{24}{Re}\left[\frac{(1 + 0.15\ Re^{0.687})\left[1 + e^{-(0.427/M^{4.63})} - (3.0/Re^{0.88})\right]}{1 + (M/Re)(3.82 + 1.28\ e^{-1.25\ Re/M})}\right] .$$

This covers a Knudsen number range from continuum to free-molecule, a Mach number range from incompressible to supersonic, and a Reynolds number range of from less than 10^{-2} to 10^{5}. It is based on (1) Millikan's empirical correction to the Stokes' drag law, (2) the incompressible "standard drag curve", and (3) a compressibility correction based on experimental variation of drag coefficient with Mach number at high Reynolds numbers. Unfortunately this equation fails both to give the free-molecule flow values for M $>$ 0.5 and to fit the experimental data for supersonic flow. Moreover, for M $>$ 0.5, it does not conform with the theoretically predicted trends that C_D be independent of Re in free-molecular flow and that C_D decrease monotonically with Reynolds number as the transition regime is approached.

Crowe[73] presents a much more complicated empirical expression which produces a better fit to both the available data and analyses and provides reasonable trends with Mach number and Reynolds number for Re $<$ 100 and M $<$ 2. His expression is:

$$C_D = \left(C_{D_{inc}} - 2\right) \exp\left\{- 3.07\ (\gamma)^{1/2}\ (M/Re)\ g\ (Re)\right\}$$

$$+ \frac{h(M)}{(\gamma)^{1/2}\ M} \exp\ (-Re/2M) + 2 \quad ,$$

where $C_{D_{inc}}$ is the drag coefficient for a sphere in incompressible flow, γ is the ratio of specific heats of the gas c_p/c_v, and g (Re) and h(M) are the devised functional relations

$$\log_{10} g\ (Re) = 1.25\ [1 + \tanh\ (0.77 \log_{10} Re - 1.92)]$$

and

$$h(M) = \left\{2.3 + 1.7\ [T_p/T_g]^{1/2}\right\} - 2.3 \tanh\ (1.17 \log_{10} M) \quad .$$

T_p and T_g are the particle and gas temperatures, respectively.

Crowe's equation is based on (1) theoretical results for free-molecule flow under the assumption of diffuse reflection of molecules; (2) Millikan's empirical formula for incompressible, rarefied flow; and (3) experimental results for incompressible and supersonic flow.

Both Carlson and Hoglund's, and Crowe's expressions were derived primarily to provide predictions for drag coefficients in ranges where no experimental data exist. As reliable data become available, they should be compared with the above predictions, and changes in the formulae should be made if necessary.

G. CONCLUSIONS

The background of the sphere drag problem has been discussed above. The character of the flow field about a sphere as a function of Reynolds number is fairly well known. There is, however, some question as to the exact Reynolds number where a separated region starts to form. There is also some uncertainty concerning the variation of the separation circle location with Reynolds number.

Analytical or numerical descriptions of the sphere flow field have given successful agreement with experiment only in the cases of continuum flow with $Re \leq 100$ and in free molecule flow. More work is needed to extend the scope of these descriptions.

The variation of drag coefficient with Reynolds number for a single smooth sphere in steady, non-turbulent, isothermal, incompressible, continuum flow has been well determined by experiment except for very high Reynolds numbers ($> 10^6$). Drag measurements in this range would be extremely useful.

The effects of turbulence on the critical Reynolds number have been observed. The effects on drag in the supercritical range of Reynolds numbers have, likewise, been determined, although the explanation of these observations is open to some uncertainty and independent confirmation of these works would be desirable. In the subcritical range, a moderate drag increase with turbulence has been observed, but measurements have not been particularly systematic. The effects of intensity and scale of turbulence have not been determined.

Various empirical relations have been devised to estimate the effects of gas rarefaction and compressibility on sphere drag in flow regimes where experimental data are not available. Since these relations are often applied to flow regimes vastly different from those used in deriving these relations, more experiments are called for to fill the gaps in available data.

III. EXPERIMENTAL APPARATUS AND PROCEDURE

A. APPARATUS*

1. Wind Tunnel

The wind tunnel used in this research is a small, vertical subsonic tunnel with variable Mach number and density capability. It may be run continuously at Mach numbers from 0.10 to 0.85 with stagnation pressures from 3 to 100 mm Hg. The tunnel is axisymmetric and has a nominal test section diameter of 2 in. A schematic drawing of the tunnel is shown in Fig. 8 and a photograph of it is given in Fig. 9.

During operation, room air passes through a fiberglass filter and then through the upstream throttling valve which regulates the stagnation pressure. The air then passes through the inlet pipe and into the diffuser-screen section. Here, various combinations of fine mesh screens and/or coarse grids are used to raise or lower the turbulence level of the incoming air to desired levels. A maximum of 8 fine-mesh screens may be used in this section for low turbulence tests, and any or all of these screens may be removed for testing at higher turbulence levels.

From the diffuser-screen section, the air passes through the settling-contraction section and into the uniform diameter test section. In addition to the above method of varying turbulence level, the test

*The wind tunnel and magnetic suspension system were designed by Sivier[21]. Modifications made by this author are discussed in this section.

section can be fitted with a thin-walled cylindrical screen holder for locating turbulence generating screens very close to the suspended spheres. Turbulence generation will be discussed further in Section III.A.3. The test section is made of Plexiglas tubing, 2 in. I.D. by 1/4 in. wall. It is fitted with three 3/4 in. diameter, optically flat windows, 90^{o} apart, at the sphere axial position. Two of these windows are for the model position sensor light beam and the third is for viewing the model by means of a low power microscope. The side of the test section opposite the viewing window contains five static pressure orifices arranged axially at 1 in. intervals, starting in the plane of the window centers. The orifices are 0.100 in. in diameter. An entrance port, located 2 1/2 in. below the center of the viewing window, is used for installing total head pressure, static pressure, and hot wire probes.

The downstream throttling valve is located just below the test section. When choked, this valve controls the test section Mach number by fixing the area ratio between the test section and the throttling valve throat. This valve can be operated with the tunnel running. After passing through the throttling valve, the air enters piping connected to the laboratory vacuum system.

With the exception of a few steel bolts, the entire wind tunnel and supporting structure is made of non-magnetic materials to prevent distortion of the magnetic field generated by the solenoid system.

2. Magnetic Suspension System

The magnetic support-and-balance system used in the present research has been designed especially for the wind tunnel described in Section III.A.1. It is a one-dimensional system consisting of two basic subsystems: (a) the electromagnets and (b) the magnetic force control system. In the present system, the drag and gravity forces on the model act vertically downward with the axial magnetic force acting to balance them. Natural radial stability is provided by properly locating the model along the axis of the solenoids. The two basic subsystems will be described below. Details of their design will be found in Ref. 74 and 75.

a. The Electromagnets

It is shown in Appendix A of Ref. 21 that the axial magnetic force on a ferromagnetic body located on the axis of a solenoid is given approximately by the expression

$$F_z = V B_i \frac{\partial H_z}{\partial z} \cos \phi \quad ,$$

where V is the volume of the body, B_i is the induced flux density in the body, $\partial H_z/\partial z$ is the axial gradient of the axial component of magnetic field strength, and ϕ is the angle between the magnetization vector and the solenoid axis. The system described here is designed to produce and control this force in order to hold the model in a fixed axial location. If the intensity of magnetization of the model (B_i) is held constant, the axial force (F_z) is a linear function of $\partial H_z/\partial z$. In the present system B_i is held constant by magnetizing the body in a steady, uniform field produced by a large pair of solenoids. These are independent of a second, much smaller, pair of solenoids which create the controllable field gradient necessary for the support of the body.

The solenoids generating the uniform field are in a configuration known as a Helmholtz pair. This consists of two coils arranged with coincident axes in such a manner that the field in the immediate vicinity of the geometric center of the pair is uniform, for all practical purposes. The properties and design of Helmholtz coil pairs are discussed in Ref. 76. The dimensions of the Helmholtz pair used in the present system are as follows:

a_i = inside radius = 3.0 in.

a_o = outside radius = 6.27 in.

ℓ = coil height = 3.0 in.

Δz = spacing between coils = 1.62 in.

The conductor material in the coils is 1/4 in. O.D. by 0.030 in. wall copper tubing, with a 1/32 in. thick polyvinyl chloride insulating coating. This tubing may be used at pressures up to 500 psi and temperatures up to 200°F.

Cooling water is supplied to the field coils by a 500 psi, 2 gpm, piston pump. There is a 500 psi pressure drop across each coil at a flow-rate of 1 gpm. The coils are connected in parallel to the cooling water supply.

The field coils are powered by the Gas Dynamics Laboratories DC power supply. This can provide up to 1200 amps at 120 volts, with either current or voltage automatically controlled. The coils produce a uniform field of 2000 oersted when operated with a current of 265 amps at 65 volts. At a cooling water flow rate of 1 gpm per coil, the above operating conditions produce a water temperature rise of 50°F. Thus, the operating temperature of the coils is well below the 200°F limit of the tubing insulation.

As mentioned above, it is necessary to have a field gradient to suspend the spheres. For this purpose, a pair of small gradient coils are located within the larger field coils (see Fig. 10). A gradient coil pair was chosen rather than a single gradient coil for the following two reasons. First, the field produced by the gradient coil changes with load on the model and, thus, if only one coil is used, the magnetization of the model changes. With two gradient coils having

opposing fields, the field due to the coils at the model location is much smaller, and the effect on the model's magnetization is reduced. Second, the field gradients are additive when the coils are in opposition, so that each coil need produce only half of the required gradient. The power requirement for each coil is reduced by a factor of four, so that the total power needed for the two coils is about half that needed if only one coil were used. This reduction in power eliminated the need for cooling the gradient coils. The one disadvantage of using two gradient coils is that there is a decrease in radial stability. For the configuration used, this amounts to a 40% reduction. The dimensions of the gradient coils used in the present system are as follows:

a_i = inside radius = 1.5 in.

a_o = outside radius = 2.25 in.

ℓ = coil height = .75 in.

Δz = spacing between coils = 1.0 in.

The coils are wound from No. 20, single filament, cement-coated magnet wire and are self-supporting. Each has a resistance of 4.5 ohms.

The suspension of a sphere without aerodynamic load, with a 2000 oersted uniform field, requires a current of .95 amps through the two coils connected in series. The voltage drop across the pair is 8.5 volts. The total load is limited to approximately 3 times the

model weight because of a heat dissipation problem from the coils. Since the relationship between magnetic force and coil current is linear, the maximum coil current is set at 3 amps.

Power for the gradient coils is provided by a 48 volt, 6 amp, regulated DC power supply.

The gradient coil design is discussed more fully in Appendix B or Ref. 21.

b. Magnetic Force Control System

The vertical magnetic force is directly proportional to the product of the model magnetization B_i and the axial gradient of the axial component of magnetic field strength $\partial H_z/\partial z$ (see Sec. A. 2. a, above). During a run, B_i is held fixed within 1% by maintaining a nearly constant current in the Helmholtz field coils. (Changes in B_i due to variations in gradient coil current or model position are negligible.) The magnetic force is regulated by controlling $\partial H_z/\partial z$ through the control of the gradient coil current.

The control system is a closed-loop, feed-back system that includes, in addition to the model and gradient coils, (1) an optical model position sensor, (2) a compensator, and (3) a gradient coil current controller. These three components are discussed below. A block diagram of the system is shown in Fig. 11.

(1) Optical Model Position Sensor. A sketch of the optical model position sensor is presented in Fig. 12. The light source is a PR-12, 6 volt flashlight bulb. Originally, a smaller bulb was used, at a lower voltage, but a more intense light was needed to suspend the .0394 in. diameter spheres. The light from the bulb is collimated by a lens and projected through the test section windows.

The beam is then partially blocked by a light mask. The portion of the beam passing through the mask is then refocused by another lens and split in half horizontally by a prism. Each half falls on small photovoltaic cells located near the focal points.

In operation, the prism is adjusted so that the beam is split approximately in half by equalizing the outputs of the two light sensors. When the sphere is located so that its shadow is split in half by the prism, the sensor outputs are equal. Vertical movement of the sphere from this null position results in unequal sensor voltage outputs, with the sign of the difference between them indicating the direction of sphere movement. This voltage difference is the error signal which is supplied to the compensator circuit.

Originally, several light masks were made, with the opening about equal to the sphere diameter in height and about three diameters in width. It was found in practice that the smaller spheres could be suspended successfully with the light mask designed for the 1/4 in.

sphere, so that only the largest mask is used now. The larger horizontal dimension of the mask opening allows the sphere to move laterally without affecting the vertical control performance.

(2) Compensator. The purposes of the compensator are to provide sufficient positive stability to the entire control loop to offset the vertical motion instability of the model/magnetic force portion of the loop and to provide the necessary control to eliminate model sag under increasing aerodynamic load. The first function is accomplished by providing error-rate control. The compensator output is related to the magnitude and sign of both the input error signal and the rate of change of this signal. The second function is accomplished with a long time-constant, error-integrating circuit in the compensator. The integrator output is the time integral of the input error. The compensator output is the sum of the error, the error rate, and the integrator output. With this system, steady-state input errors always tend toward zero. The integrator time constant is about 0.1 sec, which is about two orders of magnitude greater than the rest of the control loop. Thus, the integrator does not affect system response to rapidly varying loads.

The design of the compensator is discussed further in Ref. 75. A circuit diagram is shown in Fig. 13.

(3) Gradient Coil Current Controller. The circuit diagram of the gradient coil current controller is shown in Fig. 14. It is a solid-state,

three stage power amplifier using the compensator output to control the gradient coil current. The controller is capable of regulating the coil current from zero to three amps and has a rise time of 10 μsec. The circuit shown in Fig. 14 is not the same as originally presented in Ref. 75. Two changes were made to improve its performance. One change was to lower the input impedance of the controller, rendering it less sensitive to small input voltage fluctuations. This change reduced the ripple in the gradient coil current from 10 to 2% and eliminated the small vertical model oscillations which had adversely affected the drag data[21]. The second change was to replace two of the germanium transistors in the original controller with silicon transistors having greater stability and current handling capacity.

3. Turbulence Generation

Two methods of generating moderate to high levels of free-stream turbulence have been used in the present research. The first consists of removing from one to seven fine mesh screens from the diffuser-screen section and/or placing a grid consisting of 1/4 in. copper strips spaced 3/4 in. apart in that section. One disadvantage of generating turbulence in this manner is that the scale of the turbulence with respect to sphere diameter is rather large. Another is the difficulty in duplicating the present results without an identical facility. In spite of these two disadvantages, drag measurements at turbulence levels up to about 4% have been made using this method.

A second means of producing free-stream turbulence is to locate coarse square-mesh grids in the test section upstream of the sphere. The turbulence generated by this method has a much smaller scale than that produced by the first method and drag data can be obtained at much higher fluctuation levels. In addition, grid turbulence is more easily duplicated in different facilities. The grids are cemented to thin aluminum rings with epoxy cement. The rings can then be screwed to a thin-walled aluminum grid holder sleeve which fits into the test section. The sleeve reduces the test section diameter from 1.98 in. to 1.75 in. and locates the grids approximately 3/4 in. from the sphere center. Three different grids have been used: 8 x 8 x 0.030 in., 10 x 10 x 0.025 in., and 16 x 16 x 0.011 in. The grid holder sleeve and grid rings are photographed in Fig. 15. Figure 16 is a sketch showing the grid holder sleeve in place in the test section. Drag measurements at turbulence intensities as high as 13% have been made using the grids for generating turbulence. Results of turbulence level and energy spectrum measurements will be presented in Part IV.

4. Instrumentation

a. Pressure Measurement

A schematic drawing of the pressure measuring system is shown in Fig. 17. The settling chamber pressure is measured on two Wallace and Tiernan, aneroid-type, absolute pressure gauges having ranges of

from 0-20 and 0-100 mm Hg, respectively, and nominal precisions of 1/3% of full scale each. These gauges have been calibrated to an accuracy of $\pm$ 1/4% of full scale for the 0-20 mm Hg gauge and $\pm$ 1/3% of full scale for the 0-100 mm Hg gauge.

The differential between the test section wall static pressure and the settling chamber pressure has been measured on a Meriam precision, slant tube micromanometer (Model A-750) filled with Dow Corning No. 200 (5 centistoke viscosity) silicone fluid. The variation of the fluid specific gravity with temperature has been measured and this has been accounted for in reducing the data. The micromanometer has a mechanical precision of better than .001 in. in column height; but, because of time lags in response to small pressure fluctuations, the actual reading accuracy is estimated as $\pm$ .002 in. of fluid.

When screens are used in the test section to produce turbulence and drag measurements are being taken, the Mach number cannot be determined by direct pressure measurements. Instead, the total pressure and static pressure behind the screens are measured with probes before any drag measurements are made. These values are plotted against plenum chamber pressure for each screen and throttling valve setting. Then, when drag measurements are being made, the plenum chamber pressure is recorded and the static and total pressures are determined graphically. From these the Mach number can be determined by using the isentropic flow relations.

b. Drag Measurement

The vertical magnetic force is directly proportional to gradient coil current if the model magnetization B_i is held constant (see Sec. A.2.a). Hence, if the model weight and the gradient coil currents necessary to support the sphere under flow and no-flow conditions are known, the drag force can be calculated as follows:

$$F_{drag} = (\text{sphere weight}) \times \frac{I_{flow} - I_{no\text{-}flow}}{I_{no\text{-}flow}} \quad .$$

The currents are determined by measuring the voltages across a precision shunt with a Mosley Model 7100B strip chart recorder having a Model 17501A preamplifier. This instrument has a nominal accuracy of 0.2% of full scale.

The performance of the drag measurement system has been verified by the following procedure: a sphere with a very fine thread cemented to it is weighed and suspended. The gradient coil current is measured and then known weights are hooked onto the thread. The current is noted with each weight addition. The results are plotted as $(I - I_o)/I_o$ versus $(W - W_o)/W_o$, where I is the current needed to suspend the sphere, thread, and weights; I_o is the current needed to suspend the sphere alone; W is the weight of the sphere, thread, and weights; and W_o is the weight of the sphere alone. Two typical calibration curves are shown in Fig. 18. The maximum deviation from linearity is less than 1.4%.

c. Turbulence Measurement

The test section free-stream turbulence level has been measured with a DISA miniature hot wire probe, type 55A25, having a platinum plated tungsten wire approximately .040 in. long and .0002 in. in diameter. This probe is operated in the constant current mode using a Flow Corporation Model HWBII hot wire anemometer. This set provides compensation for wire thermal lag up to 100 kHz. It includes a square wave calibrator for setting the wire compensation. The hot wire current can be measured to $\pm$ .125 ma using a null balancing system and a precision potentiometer. The hot wire is operated at a fixed resistance ratio (R_{hot}/R_{cold}) of 1.4. The root-mean-square value of the voltage fluctuations is measured on a Flow Corporation Model 12A1 Random Signal Voltmeter. The turbulence spectrum is determined using a Tektronix Type IL5 Spectrum Analyzer plug-in module and a Tektronix Type 551 dual-beam oscilloscope. The output of the spectrum analyzer is recorded on a Mosley Model 7100B strip chart recorder.

5. Spheres

The spheres used in the present research are all commercial precision stainless steel ball bearings made of type 440-C stainless steel. Two grades have been used. Grade 5 has a surface finish of 0.7 μ in. rms and its diameter is held to 50 μ in. with a sphericity

of within 5 μ in. Grade 25 has a surface finish of 1.5 μ in. rms, a diameter held to .0001 in., and a sphericity of within 25 μ in. The drag measurements have shown no measurable difference between the two grades and they have been used interchangeably. Nominal sphere diameters used are 1 mm (.03937 in.), 1/16, 1/8, 3/16, and 1/4 in. Sphere weights have been determined to within 10^{-4} gms on a Mettler precision balance.

B. PROCEDURE

1. Operation of the Experiment

The tunnel is opened by raising the tunnel inlet assembly a few inches and rolling it on a pair of rails away from the test section and downstream sections of the tunnel, which are fixed to the floor of the laboratory. Then, with the magnetic support system operating, the model is inserted into the test section from the upstream end using a magnetic insertion probe (Fig. 19). The steel rod in the center of the probe is magnetized by the field of the Helmholtz coils, holding the sphere against the non-magnetic tip of the probe. The steel rod is positioned so that its tip does not touch the sphere. The model insertion procedure is described in the following paragraphs.

A jig is placed over the open test section to position the insertion probe precisely with respect to the tunnel centerline. The probe is

placed in the jig so that the sphere just enters the light beam of the optical model position sensor which passes through the test section. During this procedure, the integrator is uncoupled from the compensator circuit. The model is released from the probe by withdrawing the steel rod from the insertion probe. The model drops from the probe tip and is easily caught and held by the magnetic support system. The integrator is then coupled to the compensator circuit. If turbulence generating screens are to be used in the test section, the screen and screen holder sleeve are put in position at this time.

The tunnel inlet assembly may then be repositioned over the test section and the tunnel evacuated by opening the downstream valve to the vacuum system. The no-flow value of the gradient coil current is measured at this time. With the downstream throttling valve set to give the desired Mach number, the upstream throttling valve may be opened and the settling chamber pressure set to some predetermined value. This value is recorded along with the differential Δp between it and the test section static pressure, the gradient coil current, and the stagnation temperature. The settling chamber pressure may then be set to a new value and the above mentioned data again recorded. This process is repeated until all the desired data at the specific Mach number for that sphere are obtained. Then, the downstream valve to the vacuum system is closed, the tunnel is bled to atmospheric pressure and opened, and the sphere is removed.

2. Data Reduction

a. Drag Data

The majority of the drag data has been reduced on a Royal Precision Model LGP-30 console computer. A program has also been written in Fortran IV for the IBM Model 360/67. The input data are the stagnation pressure (p_o), corrected for instrument calibration and/or screen pressure drop; the differential between test section static pressure and stagnation pressure (Δp); the strip chart recorder readings for the gradient coil current with and without flow (Δx and Δx_o); the stagnation temperature (T); and the sphere weight and diameter.

The data reduction procedure is as follows: first, the pressure measurements are converted to the same units. Then, the Mach number is determined from the ratio $\Delta p/p_o$ by using the isentropic flow relation for Mach number as a function of $\Delta p/p_o$. Next, M is used to obtain the dynamic pressure (q) from the relation

$$q = 1/2\, \gamma p M^2 \quad ,$$

where $p = p_o - \Delta p$ and γ is the ratio of specific heats (c_p/c_v). The drag force is computed using the strip chart recorder readings and the sphere weight (W) from the relation

$$D = W \frac{\Delta x - \Delta x_o}{\Delta x_o} \quad .$$

The drag coefficient is then calculated from the expression

$$C_D = \frac{D}{qA} \quad ,$$

where A is the cross-sectional area of the sphere.

Reynolds number is calculated from the definition

$$Re = \frac{\rho\, Ud}{\mu} \quad ,$$

where ρ is computed from the perfect gas law at test section static conditions and μ is computed from the Sutherland viscosity law.

The following quantities are tabulated in the computer output; Mach number, Reynolds number, drag coefficient, stagnation pressure, static pressure, and velocity.

b. Turbulence Data

If u, the component of turbulent motion in the direction of the main stream in a wind tunnel at a fixed point, is resolved into harmonic components, the mean value of u^2 may be regarded as being the sum of contributions from all frequencies. If $\overline{u^2}\, F(n)\, dn$ is the contribution from frequencies between n and n + dn, then

$$\int_0^\infty F(n)\, dn = 1 \quad .$$

F(n) plotted against n is one form of what is known as the spectrum of the turbulence.

Velocity fluctuation intensities and turbulence spectra have been measured as described in Sec. 4.c, above. Correlation functions R_x are then computed numerically from the spectra by using the cosine Fourier transform relation

$$R_x = \int_0^\infty F(n) \cos (2\pi\, n x/U)\, dn$$

These, in turn, are integrated numerically to obtain longitudinal integral scales from the definition:

$$L_x = \int_0^\infty R_x\, dx \quad .$$

The computation of the correlation functions and the numerical integration of these to yield integral scales are programmed in Fortran IV for the IBM Model 360/67. The results of the turbulence measurements will be presented in Section IV.

IV. EXPERIMENTAL RESULTS AND DISCUSSION

A. TURBULENCE MEASUREMENT RESULTS

1. Turbulence Levels

From moderate to high levels of free-stream turbulence have been achieved either by varying the number of screens within the diffuser-screen section and placing a copper grid in it or by placing coarse wire grids in the test section close to the sphere (see Sec. III.A.3, above). The method used to measure turbulence levels is described in Sec. III.A.4.c. Figure 20 depicts results of measurements for the first method of turbulence generation. In these curves the Mach number is approximately equal to 0.17. They are typical of the curves for other Mach numbers. The variation of turbulence level with stagnation pressure p_o is essentially linear for a given screen configuration. The lowest turbulence levels were achieved with seven screens in the inlet section. This configuration was used for the low turbulence tests.

Higher turbulence levels were obtained with the grids placed in the test section. Figure 21 shows typical results at $M \approx 0.22$ using this method of generating turbulence. The sharp rise in the curves at low p_o corresponds to a wire Reynolds number of approximately 60, the value of Re where vortex shedding is first observed on cylinders[77]. After the sharp rise, the turbulence intensity levels off to a relatively

constant level for the 16 x 16 x 0.011 in. screen. For the 10 x 10 x 0.025 in. and the 8 x 8 x 0.030 in. screens, the curves dip slightly and then rise gradually with increasing p_o. Dryden et al.[55] have made extensive measurements of turbulence behind grids and have found no systematic variation of turbulence level with varying flow conditions at given distances from their grids. The smallest Reynolds number (based on wire diameter) of their tests is greater than the Reynolds numbers of the present measurements. It is possible that at higher Reynolds numbers the variation of u'/U with p_o would disappear.

Dryden et al.[55] have also obtained an empirical expression for the turbulence level at varying distance behind grids. This expression is

$$\frac{U}{u'} - \left(\frac{U}{u'}\right)_o = \frac{c}{b} \log_{10}\left(1 + \frac{b}{a}\frac{x}{M}\right) ,$$

where $(U/u')_o$, a, b, and c are empirically determined constants and x/M is the ratio of distance from the grid to the mesh size. Dryden made measurements with grids of several different sizes and obtained a different set of constants for each. Predictions have been obtained for the present measurements based on average values of the constants from Dryden's work. These are shown as the broken line graphs in Fig. 21. As p_o increases, the present data approach the predictions for turbulence level based on Dryden's formula. At

p_o = 70 mm Hg these data are within 10% of the estimates. It should be noted that Dryden's measurements were made at higher Reynolds numbers and greater values of x/M than in the present tests.

2. Turbulence Spectra and Scales

There are several characteristics of the free-stream turbulence that must be established if reproducible information is to be obtained from studies of the effects of turbulence on sphere drag. The intensity level, spectrum, and the scale of the turbulence are three of the more important characteristics. Information on the scale of turbulence is important for another reason: the relationship between the sphere size and the turbulence scale may provide insight into the mechanism by which the turbulence affects the flow around the sphere.

The turbulence intensity measurements are described in Sec. 1, above. The scale can be determined indirectly from information on the spectrum (see Sec. III. B. 2. b, above). The spectrum describes how the turbulent energy is distributed with frequency.

Measurements of the spectrum of the turbulence in the present wind tunnel have been made at several different flow conditions for both methods of turbulence generation. The procedure is described above in Sec. III. A. 4. c. Figure 22 depicts several representative spectra taken at certain typical flow conditions. They have been normalized as described in Sec. III. B. 2. b, above. These curves are

compared to lines of - 5/3 slope in order to determine whether there is agreement with Kolmogoroff's hypothesis concerning a universal equilibrium range[78]. This range would exist at high Reynolds numbers where the turbulence is statistically in equilibrium and uniquely determined by the parameters ϵ and ν (the dissipation and the kinematic viscosity, respectively). The range is termed "universal" because the turbulence in it is independent of external conditions, and any change in the effective length scale and time scale of this turbulence can only be a result of the effect of the parameters ϵ and ν. Turbulence in this range is termed "locally isotropic".

It is not surprising that the present curves do not show good agreement with the - 5/3 power law since the Reynolds numbers for these data are lower than those proposed for this hypothesis. Sato[79] has measured the one-dimensional spectrum at various distances behind a square mesh grid and has found that the Kolmogoroff spectrum applies only in a very restricted frequency range, if at all. His mesh Reynolds numbers Re_M are about 1.7×10^4. Liepman et al.[80], have obtained similar results for Re_M of the order of 10^4. Better agreement is obtained for higher Reynolds numbers ($Re_M = 3 \times 10^5$), however[81]. In the present tests, for the turbulence generated with grids in the test section, the maximum mesh Reynolds number is about 1200. It is not possible to define a mesh Reynolds number for the turbulence

generated by removing screens from the diffuser-screen section. If a Reynolds number based on the test section diameter is used, the maximum value of the Reynolds number is still only about 14,000.

Small peaks are observed at frequencies of approximately 38, 52, and 58 kHz in most of the spectra. Since the peaks are found at the same frequencies regardless of flow velocity or method of turbulence generation, they are most likely due to some factor other than flow phenomena. In all cases, these peaks account for only a very small part of the total turbulent energy.

Correlation functions have been computed numerically from the spectra by using the cosine Fourier transform relation. These, in turn, have been integrated numerically to obtain longitudinal integral scales (see Sec. III. B. 2. b).

Table I presents the integral scales at certain values of Mach number and stagnation pressure for turbulence generated by changing the number of screens or placing a copper grid in the diffuser-screen section. The length scales are, with one exception, greater than or equal to 1/4 in., the largest diameter of the spheres used in the present tests. No systematic variation of the scales with Mach number is noted. With no screens in the inlet section, at $M = 0.17$, the scale size decreases with increasing stagnation pressure. This change is accompanied by an increase in turbulence intensity (see Fig. 20). No large

TABLE I

Configuration in Diffuser-Screen Section	Mach Number, M	Stagnation Pressure, P_o (mm Hg)	Integral Scale, L_x (inches)
No screens	.10	40	.45
Copper grid	.10	40	.40
2 screens	.10	40	.13
No screens	.17	20	.61
No screens	.17	30	.50
No screens	.17	40	.47
No screens	.17	50	.33
No screens	.17	60	.25
Copper grid	.17	40	.41
No screens	.25	40	.50
Copper grid	.25	40	.68

TABLE II

Screen	Mach Number, M	Stagnation Pressure, P_o (mm Hg)	Integral Scale, L_x (inches)
8 x 8 x .030 in.	.14	40	.13
10 x 10 x .025 in.	.13	40	.12
16 x 16 x .011 in.	.11	40	.13
8 x 8 x .030 in.	.23	40	.13
10 x 10 x .025 in.	.22	40	.13
16 x 16 x .011 in.	.21	40	.04
8 x 8 x .030 in.	.33	40	.05
10 x 10 x .025 in.	.32	40	.25
16 x 16 x .011 in.	.31	40	.10

differences in scale are noted between the turbulence obtained with no screens in the inlet section and that obtained with the copper grid. With two screens in place, the scale is substantially smaller.

The scales of the turbulence created by placing screens in the test section for typical Mach numbers and stagnation pressures are given in Table II. In this table in all but one case, the scales are smaller than or equal to 1/8 in., the smallest sphere size used in the turbulence studies. The difference in scale size relative to sphere diameter for the two different methods of producing turbulence may be one cause for differences which appear in the drag measurements. These will be discussed in a later section.

B. SPHERE DRAG RESULTS

1. Low Turbulence, Continuum Data

In order to verify the sphere drag measurements made under "non-standard" conditions (e.g. turbulent or non-continuum flow) in the present facility, it was first desirable to obtain data under conditions as close as possible to "standard" ones and to compare these with the standard drag curve. Drag data for smooth spheres at low turbulence levels with Knudsen numbers in the continuum and near-continuum regime ($M/\sqrt{Re} < 0.025$) are presented in Fig. 23 and 24, for Mach numbers of 0.17 and 0.23, respectively. The diameters

of the spheres used in these measurements were 1/16, 1/8, 3/16, and 1/4 in. The standard drag curve is also shown as a reference in these figures. The present data agree closely with the standard drag curve, falling only about 3% above it at Re = 100 and 8% above it at Re = 4000. The scatter in the present data is approximately 4%. There are no systematic differences in the data due to sphere size, stagnation pressure, or turbulence level over the ranges observed. Mean curves representing the data of Sivier[21] are also shown in Fig. 23 and 24. His data were obtained in the same tunnel as the present tests, prior to modifications of the gradient coil current controller. These modifications eliminated the vertical jitter of the spheres which was observed in Sivier's tests. The present data lie considerably closer to the standard drag curve than the earlier results. The remaining difference is probably due to the small, but not negligible, turbulence level in the tunnel (discussed further in the next section) and to a small compressibility effect. Hoerner[63] suggests that for high subcritical Reynolds numbers, and Mach number below the critical Mach number (< 0.6), the pressure coefficient on a blunt body is modified by compressibility as follows:

$$C_{p_{comp}} = C_{p_{inc}} (1 - M^2)^{-0.3}$$

For Re $>$ 1000, where the drag is largely pressure drag, the total drag coefficient would be expected to vary in a like manner. For Mach numbers 0.17 and 0.23, compressibility would be expected to increase the drag over the incompressible values of 0.9 and 1.6%, respectively. Thus, some of the difference between the present data and the standard drag curve is due to the effect of compressibility.

The scatter in the present data is largely due to random fluctuations in the field coil current and, at the lower Mach numbers and stagnation pressure levels, to uncertainty in the pressure and current measurements. The current fluctuations were caused by variation in the AC line voltage to the Gas Dynamics Laboratories DC power supply. The scatter in C_D due to errors in pressure and current measurements varies with Mach number, stagnation pressure level, and sphere size. The spread in C_D for maximum expected measurement uncertainty for a 3/16 in. diameter sphere at a nominal Mach number of 0.17 is shown in Fig. 25. For the lower Reynolds numbers the spread is quite large. This trend is typical of the scatter for other Mach numbers and sphere sizes. The spread shown in Fig. 25 is primarily due to the uncertainty in the measurement of the gradient coil current. For smaller spheres the largest part of the scatter is due to uncertainty in the measurement of Δp, the differential between the static and stagnation pressures.

The good agreement between the present data and the standard drag curve and the low scatter attest to the reliability of the experimental technique and the absence of any large systematic errors.

2. Turbulent Flow Data

Previous experiments on turbulent flows around blunt bodies indicate that free-stream turbulence can produce significant changes in the base pressure and, hence, drag coefficient. Increases in drag coefficient for flat plates perpendicular to the free stream must be attributed to effects of the turbulence on the wake of the plates, since separation is fixed at the edges of the plates and there is no skin friction contribution to the drag force[59]. One physical explanation of the effect of turbulence on the wake is the fact that turbulence reduces the extent of the separated region behind the body so that the flow in the main stream must turn at a sharper angle. There must be a greater pressure difference between the outer flow and the base region to produce the increased curvature in the streamlines; and, since the free-stream pressure is fixed, the base pressure must be lower.[4] Another explanation is that the laminar-turbulent transition point of the separated layer shifts forward towards the body affecting the vorticity transfer and dissipation in the wake and, hence, the form drag.[32] In both explanations, the turbulent free stream acts on the periphery of the wake to create a lower pressure within. The ratio of the wake

periphery to its cross-sectional area gives some indication of the ability of the turbulence to affect the base flow and, consequently, the drag coefficient. For a sphere, the periphery and cross-sectional area are proportional to the diameter and its square, respectively. Thus, the ratio of the two varies as 1/d. As 1/d increases, the effect of turbulence on the base flow should be greater. It is conceivable that the scale of the turbulence also has an effect. Experiments with cylinders in turbulent flow[60] have shown that when Re and u'/U are kept constant, there is a value of the ratio of turbulent scale to diameter where the heat transfer from the body reaches a maximum. A resonance between energy containing eddies in the free stream and eddies shed from the cylinder has been suggested as a reason for the heat transfer maxima.

Two different methods of turbulence generation have been used in obtaining sphere drag measurements in turbulent flow (see Sec. III.A.3). Since these two methods produce turbulence of generally different levels and scales, the drag data for each method will be presented separately.

Drag data have been obtained at turbulence levels of from 0.4 to 3.3% and Reynolds numbers of from approximately 200 to 800 by varying the number of screens in the diffuser-screen section and placing a copper grid in it. The scale of the turbulence which is obtained by this method is of the order of, or greater than, the diameter of the

spheres tested (see Sec. A. 2). Figure 26 depicts the drag coefficient as a function of turbulence level for certain values of Reynolds number from 200 to 800. These data points have been obtained from plots of C_D versus Re at different turbulence intensities. It is evident from this figure that moderate levels of turbulence produce significant drag increases for the range of Reynolds number shown. A heightened interaction between the turbulent free stream and the flow in the base region causes a lowered base pressure and, thus, an increased base drag.

The percentage drag increase as a function of Reynolds number for different turbulence levels is graphed in Fig. 27. These curves clearly show the decreasing influence of turbulence with decreasing Reynolds number. They indicate that turbulence would have little effect on the drag coefficient for Re $\leq$ 100, for intensities below 3%. Sivier[21] noted a similar trend for turbulence intensities up to 8%. His data can be compared with the present data only qualitatively since he did not specify his exact turbulence levels. One reason for the decreasing influence of turbulence with decreasing Re is the smaller and more stable separated region on which the turbulence can act. Figure 2 shows that the downstream extent of the base flow region decreases very rapidly for Re $<$ 150. Another reason for the decrease is the thicker viscous layer about the sphere and separated region which the turbulence cannot penetrate.

It was mentioned in Sec. IV. B. 1 that the small, but non-negligible, level of turbulence in the wind tunnel may have been partly responsible for the differences between the present data and the standard drag curve. The bottom curve in Fig. 27 shows that a 1% turbulence level causes approximately a 6% increase in the drag coefficient over values predicted by the standard drag curve. At the higher Reynolds numbers of the present "low turbulence" tests, turbulence levels were of the order of 1%.

In addition to its effect on base pressure, turbulence alters the Reynolds numbers at which certain phenomena take place in blunt body flow fields. For spheres in turbulent flows, experiments have shown that turbulence lowers the upper[10, 55] and lower[21] critical Reynolds numbers. Torobin and Gauvin[10] relate the lowering of Re_{uc} to the ability of the turbulent eddies to overcome the viscous damping forces set up by the velocity gradients at the sphere surface. Their theory predicts that transition will occur at a constant value of the parameter $[(u'/U)^2 \, Re]$ and they empirically determine this value to be 45. In the present tests, turbulence levels and Reynolds numbers were not high enough to reach this value. However, changes were observed in the lower critical Reynolds number. At low turbulence levels, lateral motions of the sphere associated with the oscillating separated region and asymmetric vortex shedding are first observed at Re = 350. At

turbulence levels in the range of from 1 to 3%, the lateral motions appear at a Reynolds number of about 200. The oscillations are less violent than those observed at lower turbulence levels. No effect of sphere size has been observed in the data obtained by the first method of turbulence generation.

Drag coefficient data also have been obtained with turbulence generated by placing grids in the tunnel test section very close to the spheres. This method has been used to obtain drag measurements at turbulence levels of from 3 to 13% and Reynolds numbers of from approximately 600 to 5000. The scale of the turbulence using this method is generally smaller than the sphere diameters used ($0.16 < L_x/d < 2.0$) (see Table II, p. 59). Typical plots of C_D versus Re for different Mach numbers, screen mesh sizes, and sphere diameters are presented in Fig. 28a through 28e. No systematic variation of the drag coefficient with Mach number is apparent for the range of Mach numbers of these measurements ($0.13 < M < 0.33$). However, a very pronounced effect of sphere diameter is evident. At a given Reynolds number, the drag coefficient is greater for smaller sphere diameters. For example, in Fig. 28a at Re = 2000, the drag coefficient for the 1/8 in. diameter sphere is 14.8% greater than the C_D value for the 1/4 in. diameter sphere. This drag variation with diameter is smaller at the beginning and end of the range of Reynolds numbers used in these tests.

This trend is particularly noticeable in Fig. 28a and 28b. The Reynolds number range does not extend high enough to predict whether the diameter effect disappears for Re $>$ 5000. In Fig. 29 values of drag coefficient at certain specific Reynolds numbers are plotted as a function of the inverse of the sphere diameter (1/d). For the range of 1/d shown, the drag coefficient increases monotonically with this parameter. Figure 29 clearly shows the diameter effect mentioned at the beginning of this section. At very large or small values of 1/d, a decrease in this effect might be expected; however, for the range of 1/d of the present tests, this trend was not observed. It is conceivable that the scale of turbulence also has an effect; but, for the range of scale size in the present tests, no systematic changes are apparent. The reasons for a diameter effect occurring for only one of the two methods of turbulence generation are not clear. Although the scales of the turbulence were different in the two cases, there was not enough overlap in the ranges of Reynolds number and turbulence intensity to separate out a scale size effect.

As mentioned above, turbulence alters the Reynolds number at which certain phenomena occur in the sphere flow field. An example of this effect is shown in Fig. 30 where the C_D-Re curves for M = 0.21 and the 16 x 16 x 0.011 in. screen are shown together with the portion of the standard drag curve for $5 \times 10^2 < Re < 2.5 \times 10^5$. The expected

value of Re_{uc} based on the prediction of Torobin and Gauvin[10] for a turbulence level of 4.5% is also given in this figure. The similarity of shape of the present data curves to that of the standard drag curve suggests similar flow phenomena. However, these phenomena occur at lower Reynolds numbers for the flow with turbulence. Similar turbulence effects also can be seen by comparing Fig. 28b through 28e with the standard drag curve.

3. Rarefied Flow Data

Because of the lack of experimental sphere drag coefficient data in certain ranges of Mach number and Reynolds number, various elaborate empirical relations based on available data and theories have been devised. One area where there is a scarcity of data is in the subsonic, compressible, slip flow regime. The present data have been obtained to help fill this void.

Present data showing the effects of compressibility and gas rarefaction are shown in Fig. 31. The data were obtained with smooth spheres having diameters of 1 mm (0.03937 in.) or 1/16 in. The stagnation pressure for these measurements was always less than 10 mm Hg and, consequently, the turbulence levels were very low (see bottom curve, Fig. 20). Drag coefficient is plotted as a function of Mach number for certain values of Reynolds number ranging from 40 to 120. The data points shown were obtained from graphs

of C_D versus Re at different Mach numbers. As shown in Fig. 31, the range of Knudsen number ($M/\sqrt{Re}$) for each curve is within the slip flow regime ($0.01 \leq M/\sqrt{Re} \leq 0.1$). The lower Reynolds number curves show a smaller increase with Mach number than the higher Reynolds number curves. For Re = 40 there is almost no drag increase with Mach number, while for Re = 120, the drag coefficient at M = 0.57 is nearly 8% greater than the value at M = 0.17. This is due to an increased effect of slip at the lower Reynolds numbers where a larger portion of the total drag is caused by skin friction. The effect of compressibility on the form drag is still present at the lower Reynolds numbers, but here the form drag accounts for a smaller part of the total drag. The relationship between Reynolds number and amount of increase in C_D with Mach number was observed previously by Kane[68] for supersonic sphere drag. He compared his data at Mach 2.5 with an empirical prediction by Millikan[67] for subsonic, incompressible flow. The supersonic data fell above Millikan's prediction for higher Reynolds numbers ($Re > 60$) but fell below it for lower ones, presumably for the reason mentioned above.

Figure 32 is a comparison of present data, the empirical predictions of Carlson and Hoglund[1] and Crowe[73], and the incompressible values from the standard drag curve. Drag coefficient is plotted as a function of Mach number for Reynolds numbers of 40, 60, and 100.

For the ranges of Re and M shown, this figure clearly shows the superiority of Crowe's empirical formula for predicting both the absolute value of the drag coefficient and its trend with increasing Mach number. Crowe's predictions differ from the present data by approximately 5.3% at Re = 40 and 1.7% at Re = 100.

In Fig. 33, present data for Reynolds numbers of 150 and 200 are compared with the predictions of Carlson and Hoglund[1], and Crowe[73], data of Goin and Lawrence[65], and Sivier[21], and values from the standard drag curve. As in Fig. 31 and 32, drag coefficient is plotted against Mach number. Again, Crowe's empirical formula predicts the trend and absolute value of the current data better than Carlson and Hoglund's. Goin and Lawrence's data for Re = 200 fall below the present data and the graphs from the three predictions. For M = 0.20 their measurement lies about 6% below the incompressible standard drag curve value. Their drag values increase with increasing Mach number showing compressibility effects.

Sivier's results for Re = 150 and 200 are given in Fig. 33 by mean curves which he drew through his data points. The trend for these curves does not agree with that of the present data or of Goin and Lawrence's data. This may be due to the considerable scatter in his actual data points.

An attempt has been made to correlate the present continuum and non-continuum data with the variables $\mathcal{M}(C_D - 1)$ and r_o/λ suggested by Brooks and Reis[40] (see Fig. 3). The data can be approximated by a straight line over the range of r_o/λ covered in this investigation. These data do not extend far enough into the non-continuum regime to detect the leveling off shown in Fig. 3.

In summary, the present non-continuum drag results are well represented by an empirical expression formulated by Crowe. Effects of both compressibility and gas rarefaction are evident in the data. Data by Goin and Lawrence for Re = 200 exhibit a trend with Mach number similar to that of the present data, but they fall below both it and the standard drag curve continuum values. Knudsen numbers up to 0.06 have been achieved with the present measurements. Data at higher values are desirable but are beyond the capabilities of the present wind tunnel and magnetic suspension system.

V. SUMMARY AND CONCLUSIONS

A review of the literature has revealed a scarcity of sphere drag data in the subsonic slip flow regime where both non-continuum and compressibility effects are important. A dearth of drag measurements in turbulent flows at subcritical Reynolds numbers has also been noted. The purpose of the present work has been to examine sphere drag under these non-idealized conditions where gas rarefaction, compressibility, and turbulence must be taken into account. An extensive experimental program has been carried out in order to fulfill this objective. A small, vertical, subsonic wind tunnel incorporating a magnetic suspension system has been utilized for this research. Before studying the effects of non-standard conditions, certain modifications were made in the suspension system and the instrumentation was carefully calibrated. Methods for generating turbulence were developed and hot-wire measurements were made to determine the characteristics of this turbulence. Drag measurements were then obtained under near-standard conditions in order to verify the experimental technique. Finally, sphere drag data were obtained under non-standard conditions. The results have been studied and compared with existing data and empirical predictions wherever possible. Physical explanations have also been given for most of the current observations. The major aspects and findings of this research investigation are summarized below:

1. Accurate sphere drag measurements under non-standard flow conditions using a conventional wind tunnel incorporating a one-component magnetic suspension system have been made at Reynolds numbers ranging from 40 to 5000, Mach numbers of from 0.10 to 0.57, Knudsen numbers as high as 0.060, and turbulence intensities up to 13%. The scatter in the present data is approximately 4%. It is largely due to random fluctuations in the field coil current and, at the lower Mach numbers and stagnation pressure levels, to uncertainty in the pressure and current measurements. For the low Mach number, low Knudsen number, and low turbulence cases, the data agree closely with the standard drag curve, falling only about 3% above it at Re = 100 and 8% above it at Re = 4000. This discrepancy is attributed to a low, but non-negligible, level of turbulence which exists in the tunnel flow and to compressibility effects.
2. The sphere drag measurements taken with moderate (0.4 to 3.3%) levels of free-stream turbulence and turbulence scales of the order of or greater than the sphere diameter show a significant drag increase with turbulence level for Reynolds numbers between 200 and 800. The drag coefficient increases approximately linearly with turbulence level in this range of Re. The drag rise is attributed to a heightened interaction between the turbulent free stream and

the flow in the base region, which cause a lowered base pressure and, thus, an increased base drag. The data indicate that for a given turbulence level, the percentage drag rise due to turbulence decreases with decreasing Reynolds number. Results show that turbulence would have little effect on the drag coefficient for $Re < 100$ for intensities below 3%. One cause of the decreasing influence of turbulence with decreasing Re is the smaller and more stable separated region on which the turbulence can act. Another cause is the thicker viscous layer about the sphere and separated region which the turbulence cannot penetrate. No effect of sphere diameter is evident in this data.

3. For sphere drag data obtained at turbulence levels of from 3 to 13%, turbulence scales of the order of or smaller than the sphere diameter, and Reynolds numbers of from 600 to 5000, a very pronounced effect of sphere diameter is evident. At a given Reynolds number, the drag coefficient is greater for smaller sphere diameters. This drag variation with diameter is smaller at the beginning and end of the range of Reynolds numbers used in the tests. Values of drag coefficient at certain specific Reynolds numbers are found to increase monotonically with the inverse sphere diameter 1/d. The ratio of the wake periphery to its cross-sectional area gives an indication of the ability of the turbulence to affect

the base flow, and this ratio varies as 1/d. The reasons for a diameter effect occurring for only one of the two methods of turbulence generation are not clear, although it may be attributable to the scale of turbulence. However, there was not enough overlap in the ranges of Reynolds number and turbulence intensity for the low and high intensity cases to separate out a scale effect.

4. The Reynolds numbers at which certain phenomena take place in the sphere flow field are lowered by the presence of free-stream turbulence. At low turbulence levels, lateral motions of the sphere associated with the oscillating separated region and asymmetric vortex shedding are first observed at Re = 350. At turbulence levels in the range of from 1 to 3%, the lateral motions appear at a Reynolds number of about 200.

   At higher turbulence levels, the dip and rise which are present in the standard drag curve in the range $10^3 < Re < 10^5$ are observed over a much narrower and lower Reynolds number range. The similarity in shape of the present C_D-Re curves to that of the standard drag curve suggests similar flow phenomena. However, these phenomena occur at lower Reynolds numbers for the flows with turbulence.

5. Present data for Reynolds numbers ranging from 40 to 200, Mach numbers of 0.17 to 0.57, and Knudsen numbers in the slip flow

regime exhibit pronounced effects of compressibility and gas rarefaction. Graphs of C_D versus Mach number for certain values of Reynolds number show a smaller increase with Mach number for the lower values of Re. This trend is due to an increased effect of slip at the lower Reynolds numbers where a larger portion of the total drag is caused by skin friction. The effect of compressibility on the form drag is still present at the lower Reynolds numbers, but there the form drag accounts for a smaller part of the total drag.

6. Predictions of drag coefficient based on an empirical relation formulated by Crowe[73] agree very well with present data in the subsonic, slip flow regime. An empirical relation formulated by Carlson and Hoglund[1] and data obtained by Sivier[21] and Goin and Lawrence[65] differ somewhat from the present data.

While a great deal has been learned from the present investigation, there are still areas of the sphere drag problem which require further research. In "standard" flow, drag data in the supercritical regime is scarce and disparate. In turbulent flow, additional investigation is needed on the effects of diameter and turbulence scale for subcritical Reynolds numbers. Results from prior studies of the effects of turbulence on the upper critical Reynolds number and on drag in the

supercritical regime require independent confirmation. The present studies on non-continuum and compressibility effects could profitably be extended to higher Knudsen and Mach numbers.

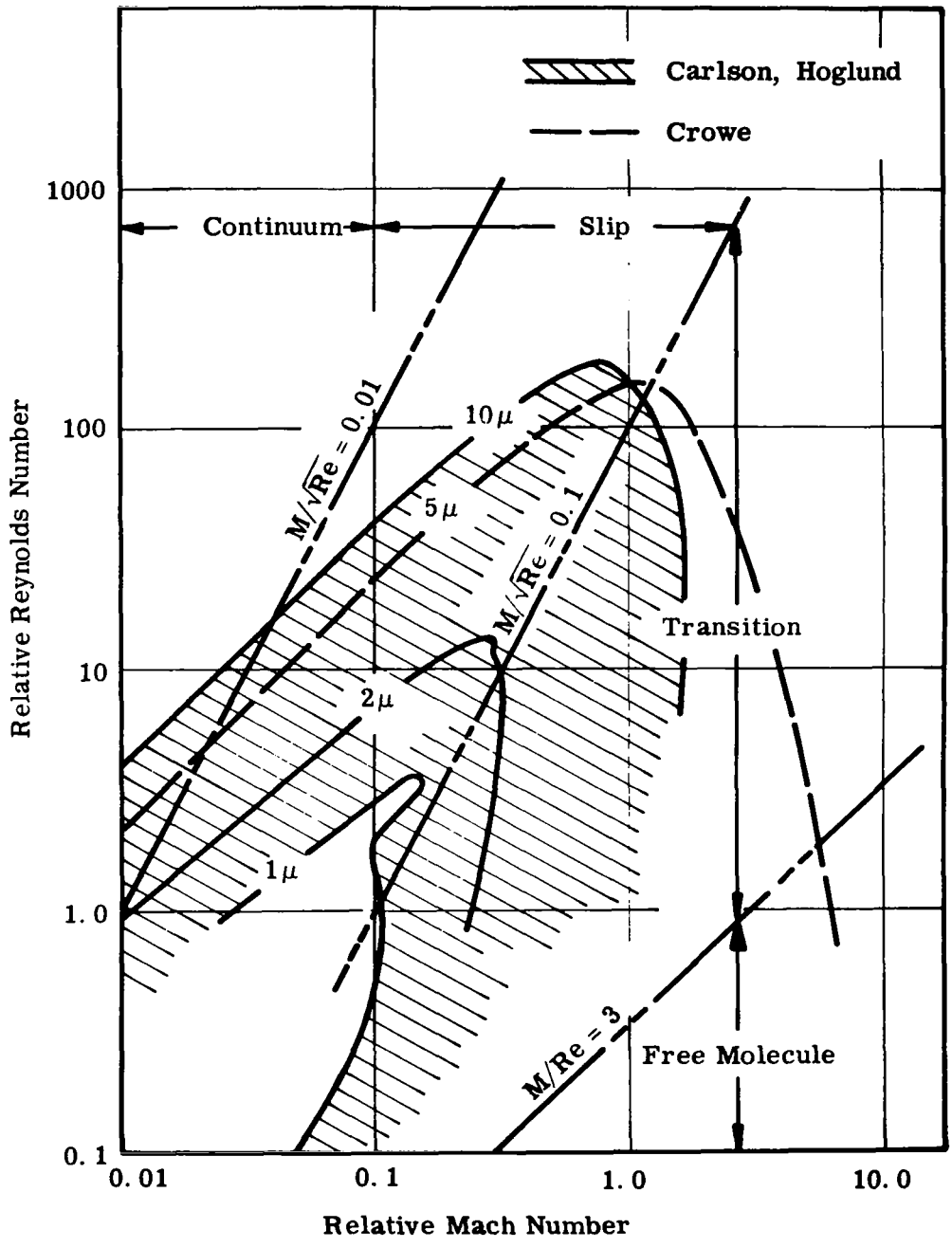

Figure 1. Typical Particle Gas Dynamic Trajectories

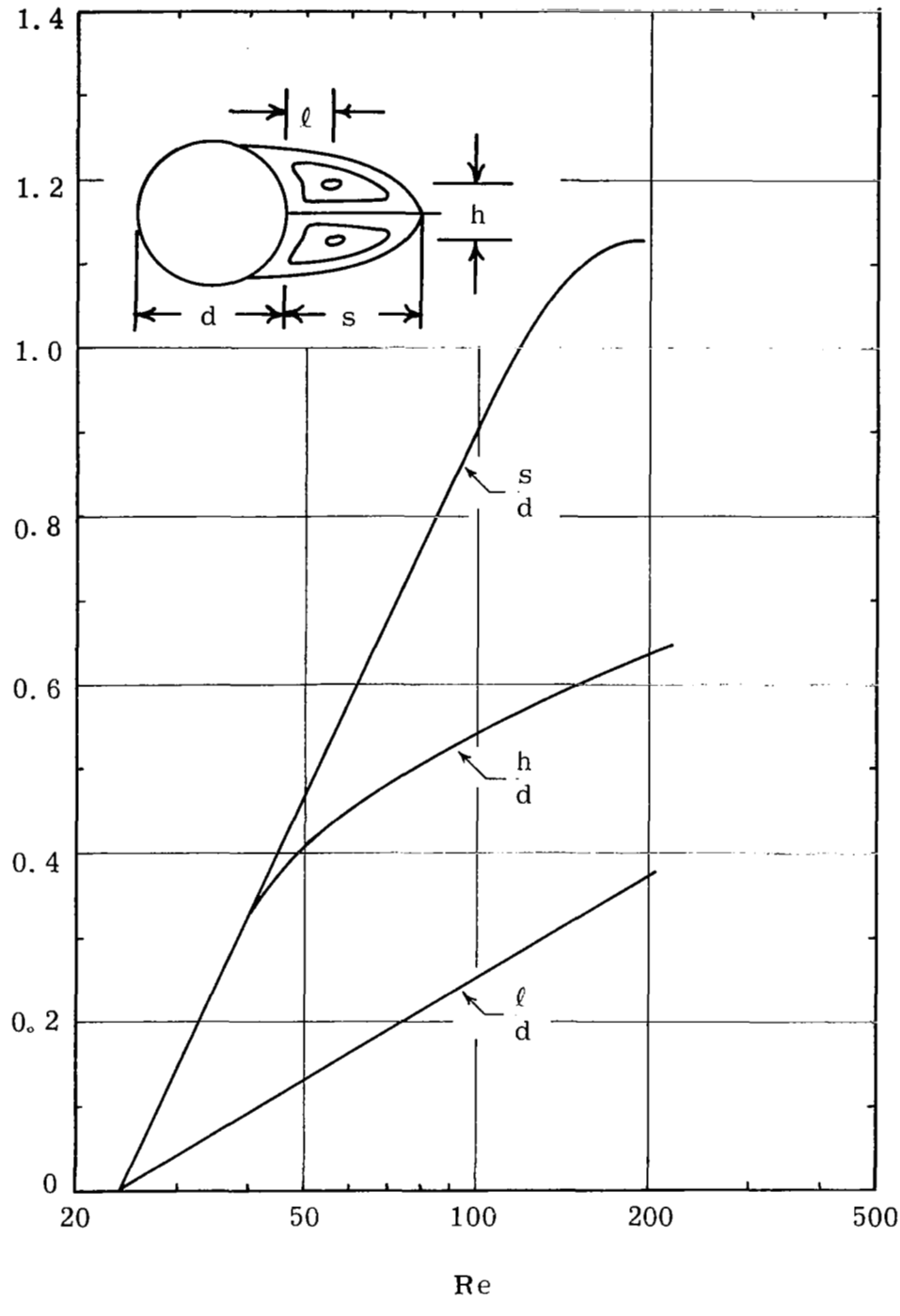

Figure 2. Sphere Wake Dimensions as a Function of Reynolds Number (Taneda)

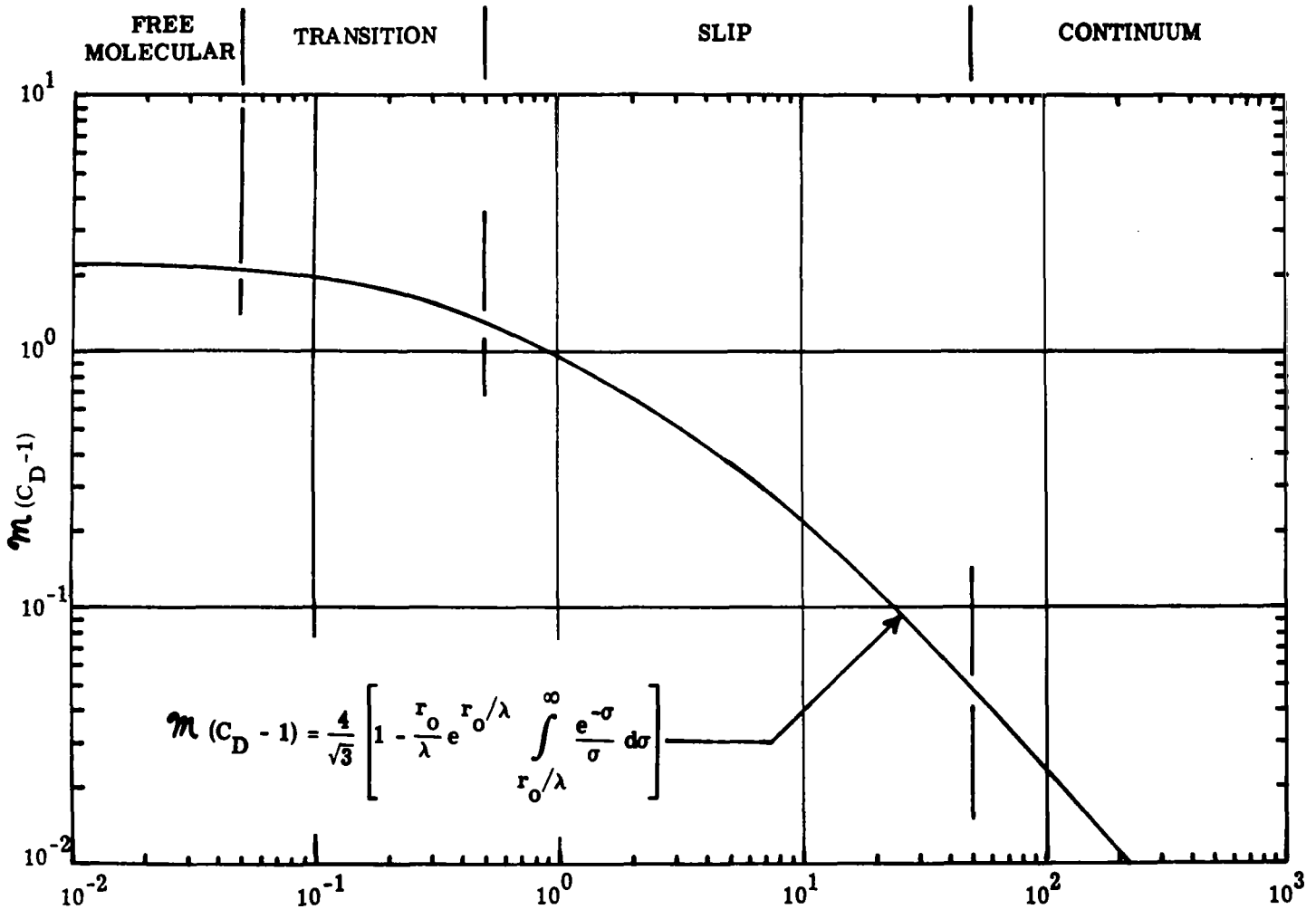

Figure 3. Relationship between $\mathcal{M}(C_D\text{-}1)$ and r_o/λ for a Cylinder (From Brooks, Reis)

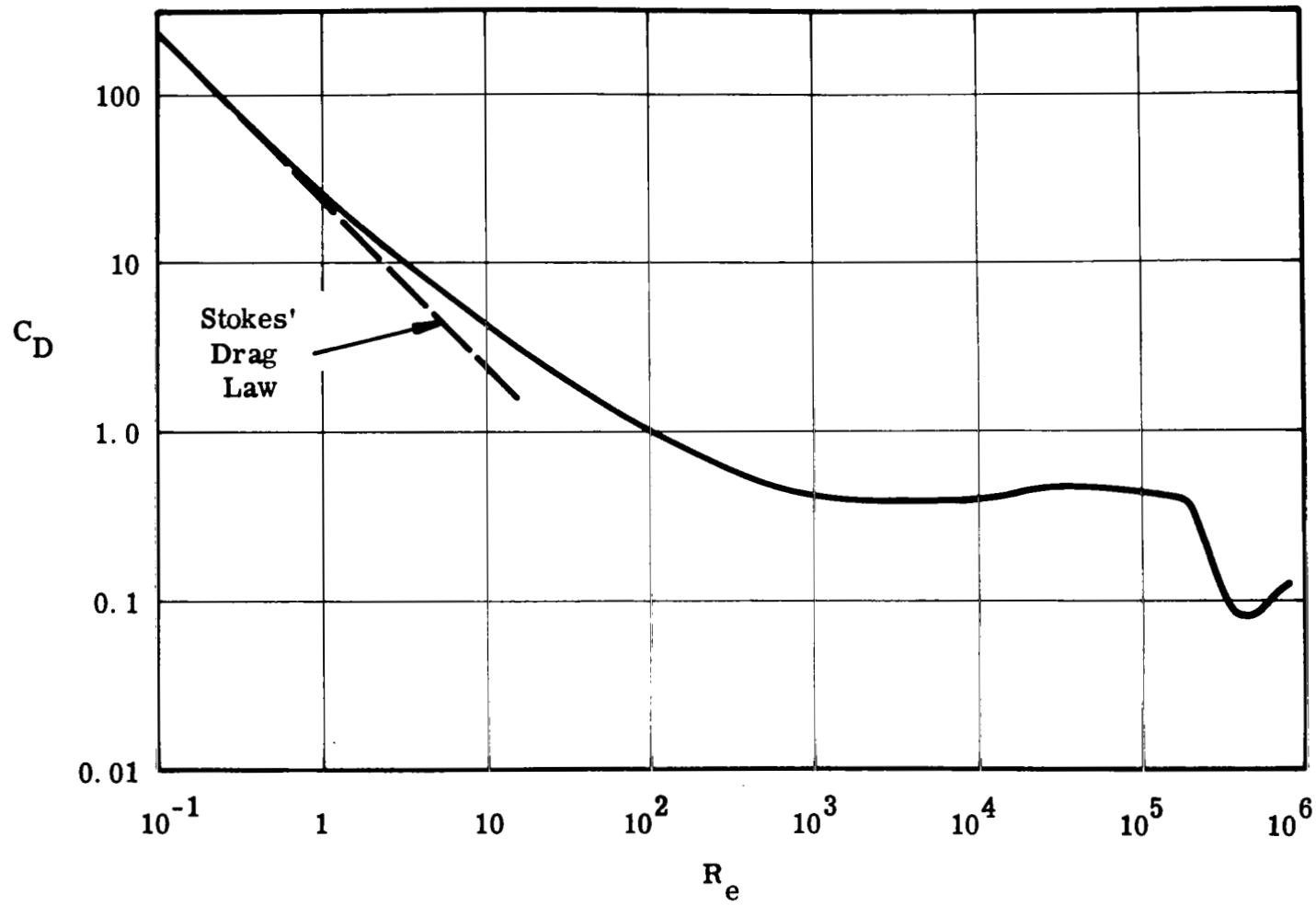

Figure 4. Standard Curve of Sphere Drag Coefficient

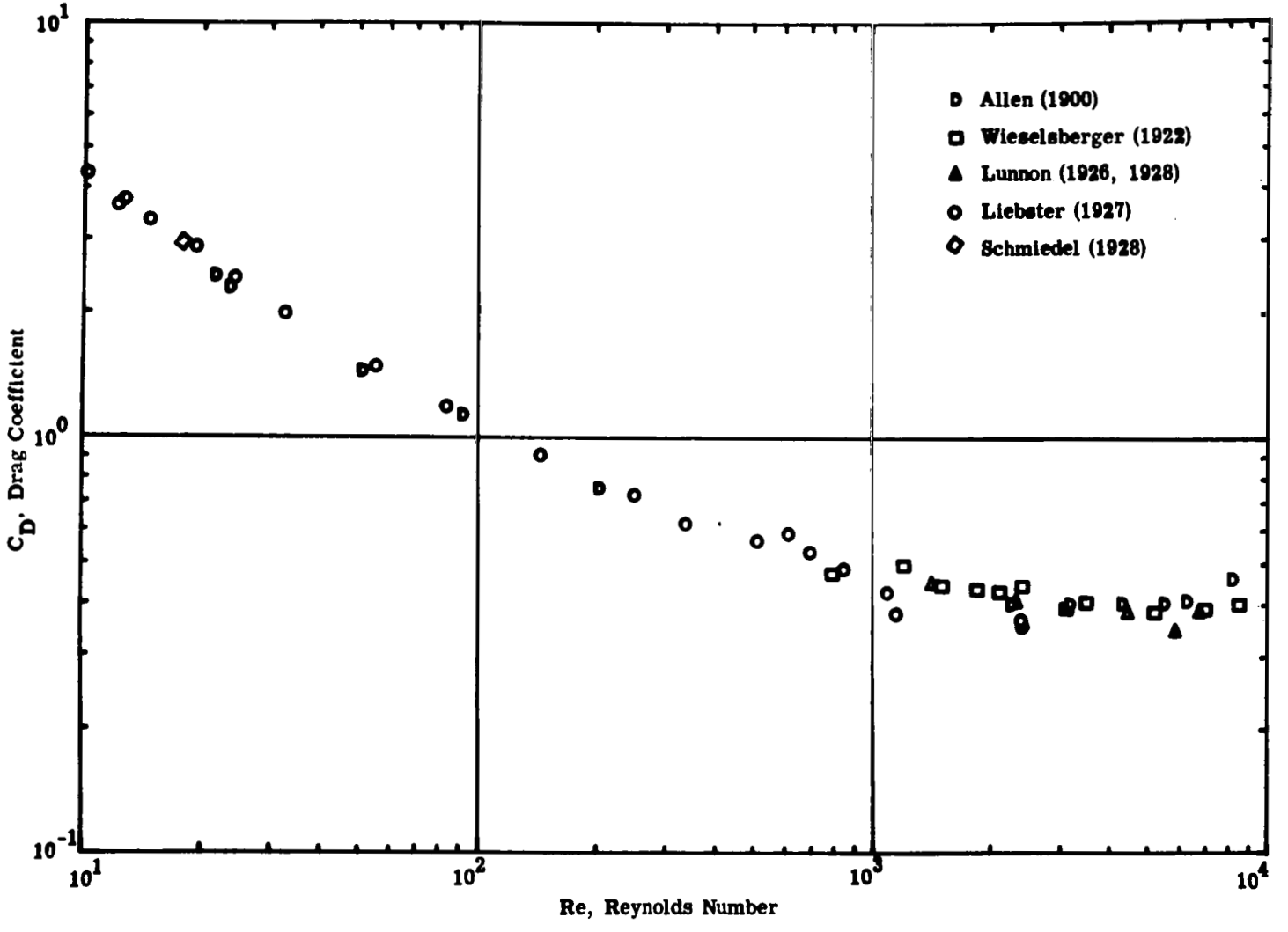

Figure 5. Sphere C_D-Re Relationship: Classical Data

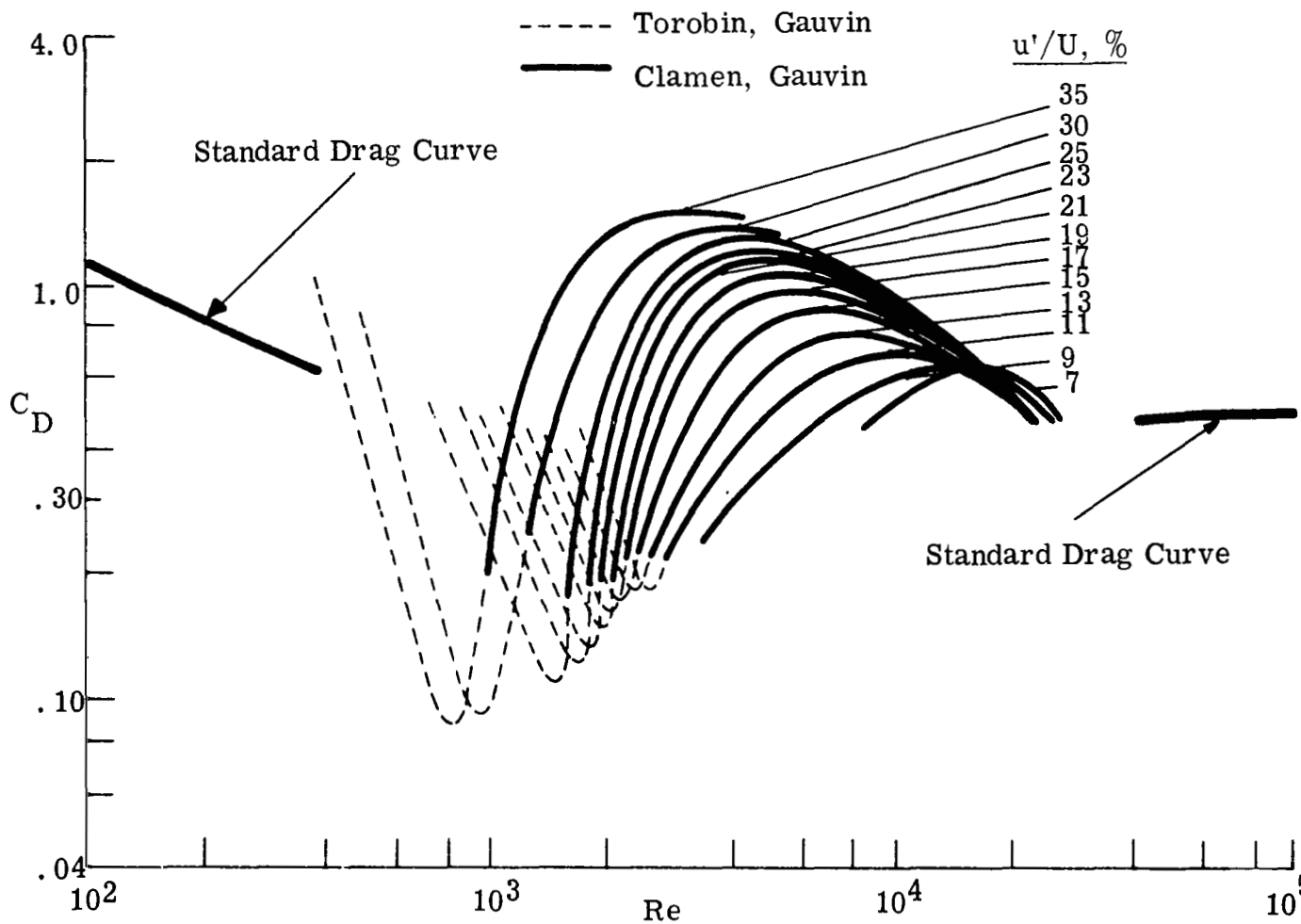

Figure 6. Effect of Turbulence on Critical and Supercritical Sphere Drag (from Clamen and Gauvin)

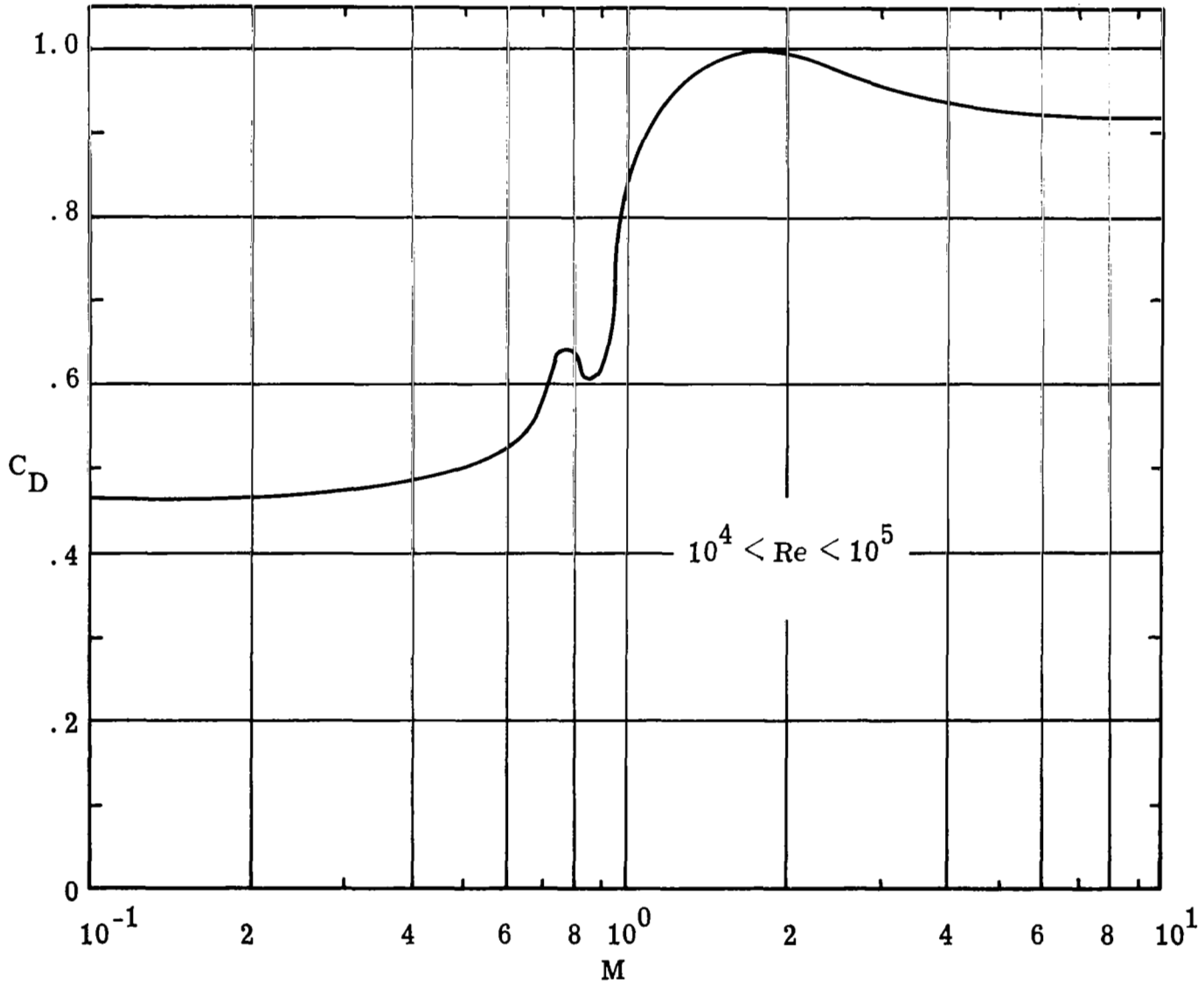

Figure 7. Effect of Compressibility on Sphere Drag (from Hoerner)

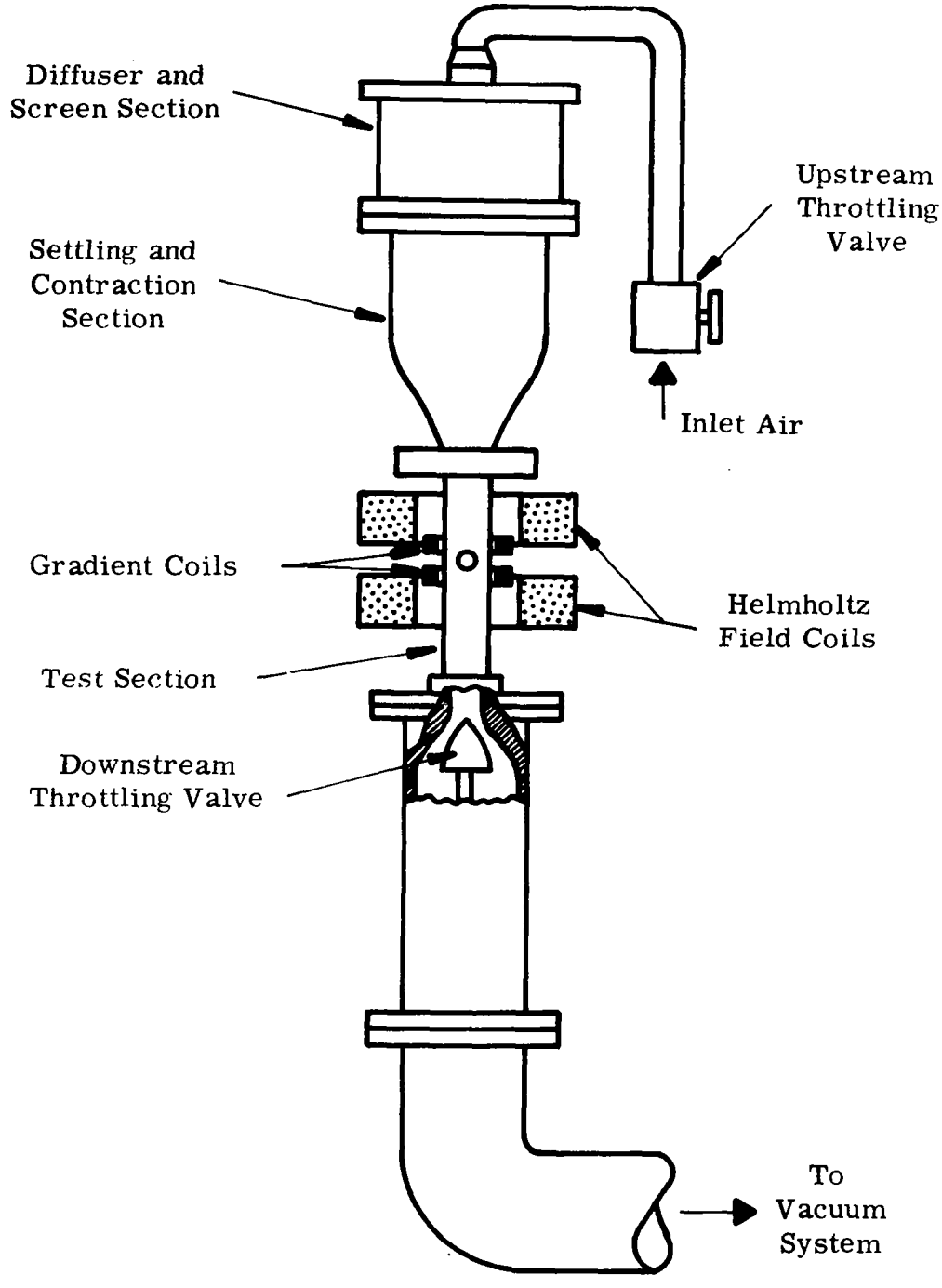

Figure 8. Sketch of Wind Tunnel

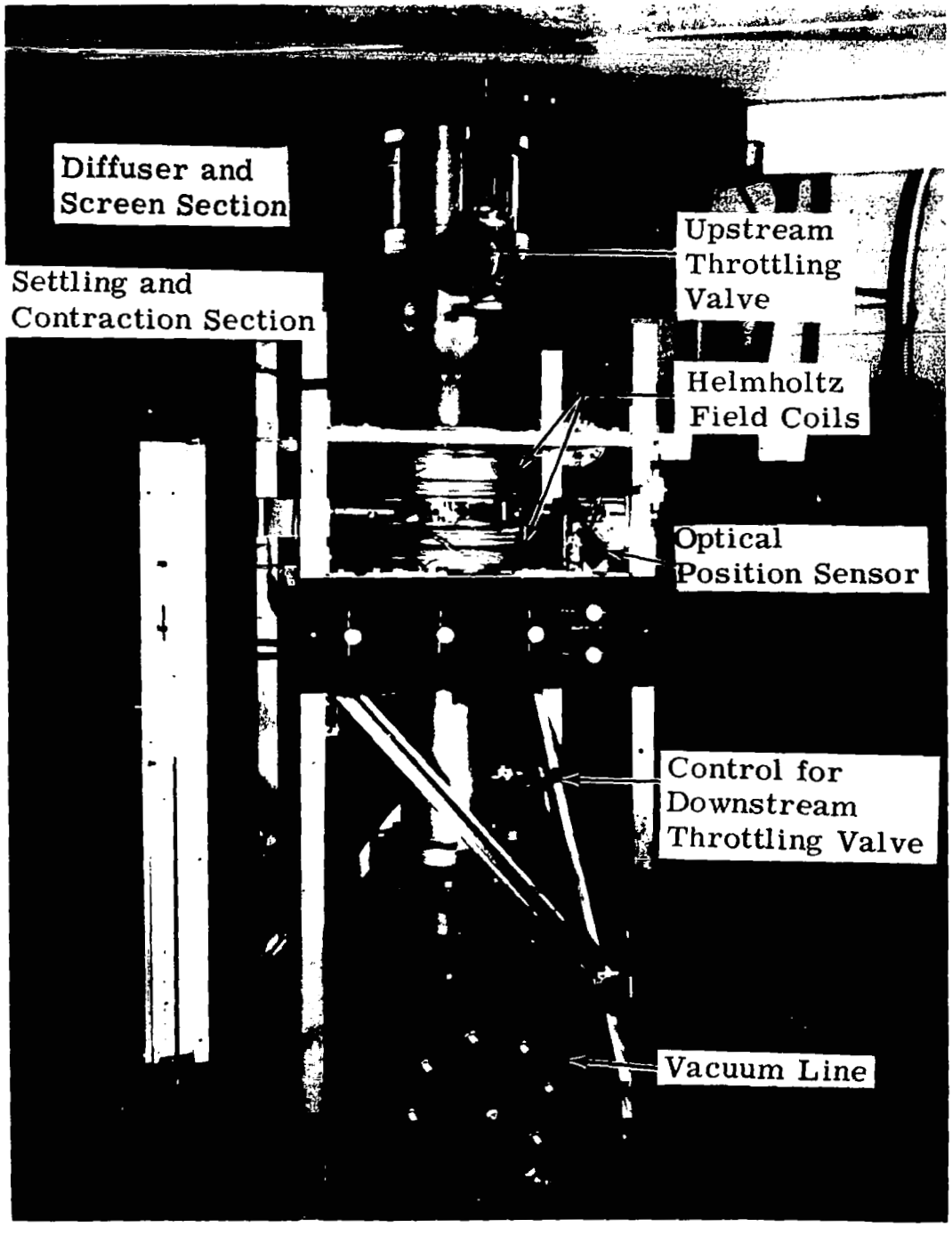

Figure 9. Photograph of Wind Tunnel

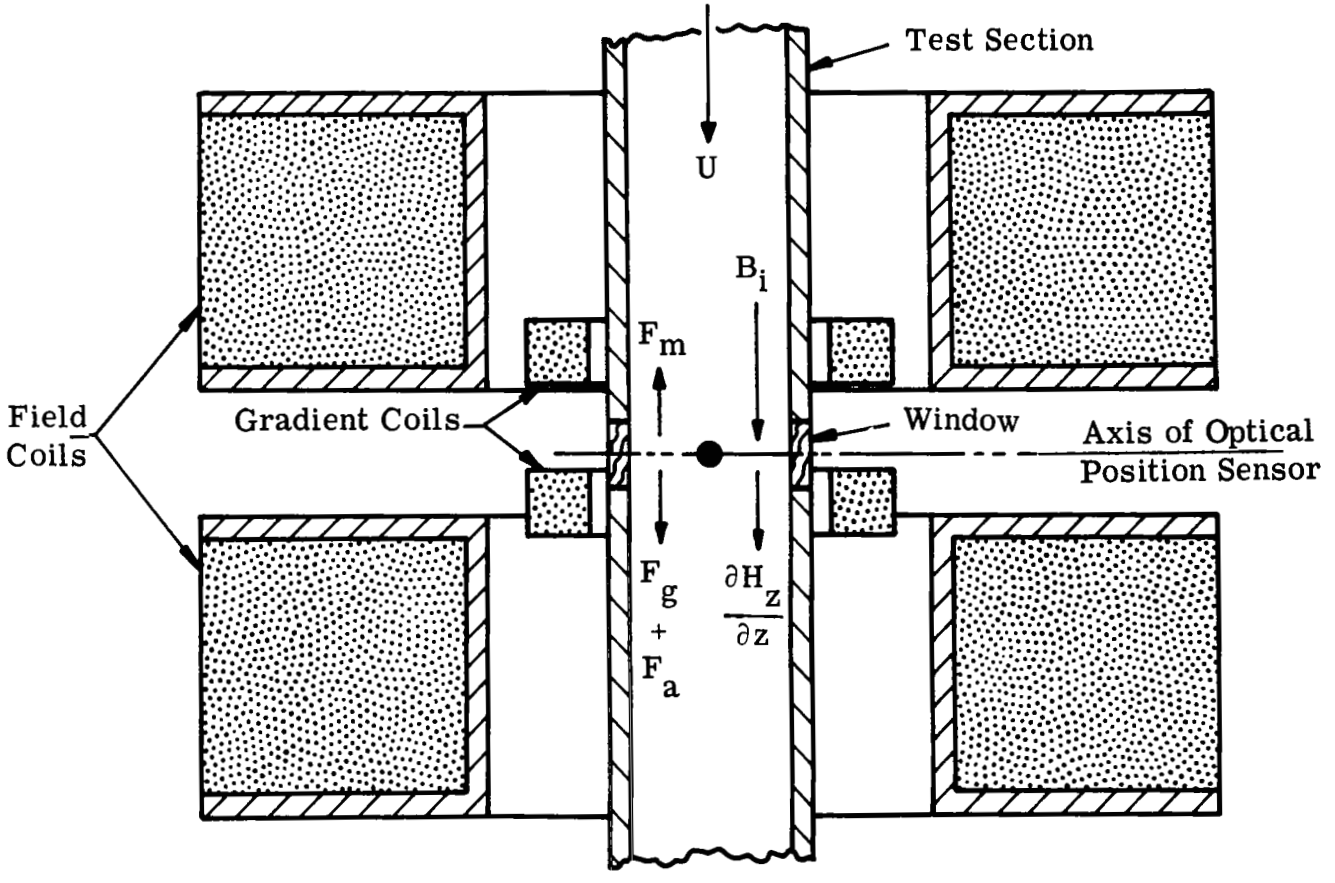

Figure 10. Sketch of Magnetic Coils and Test Section Assembly.

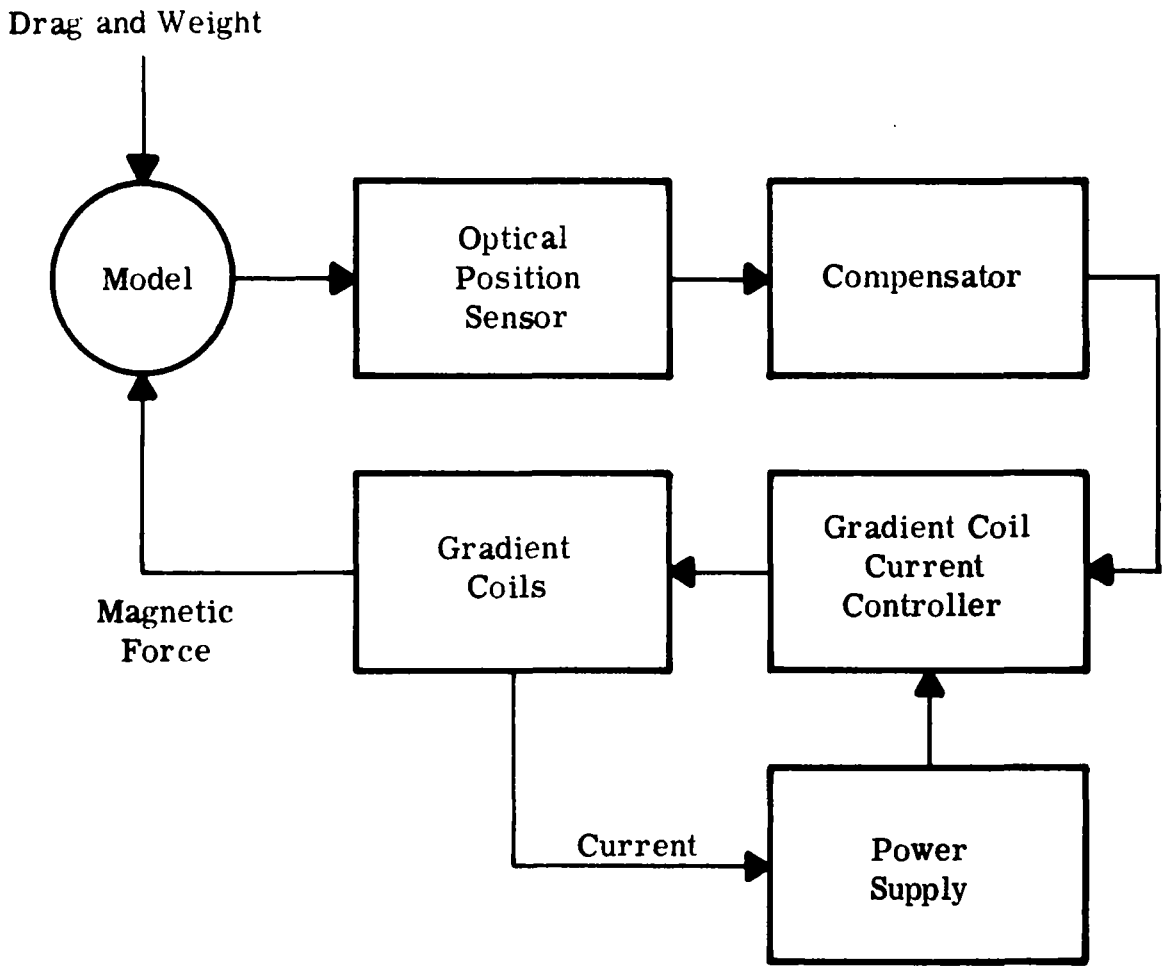

Figure 11. Block Diagram of Magnetic Force Control System.

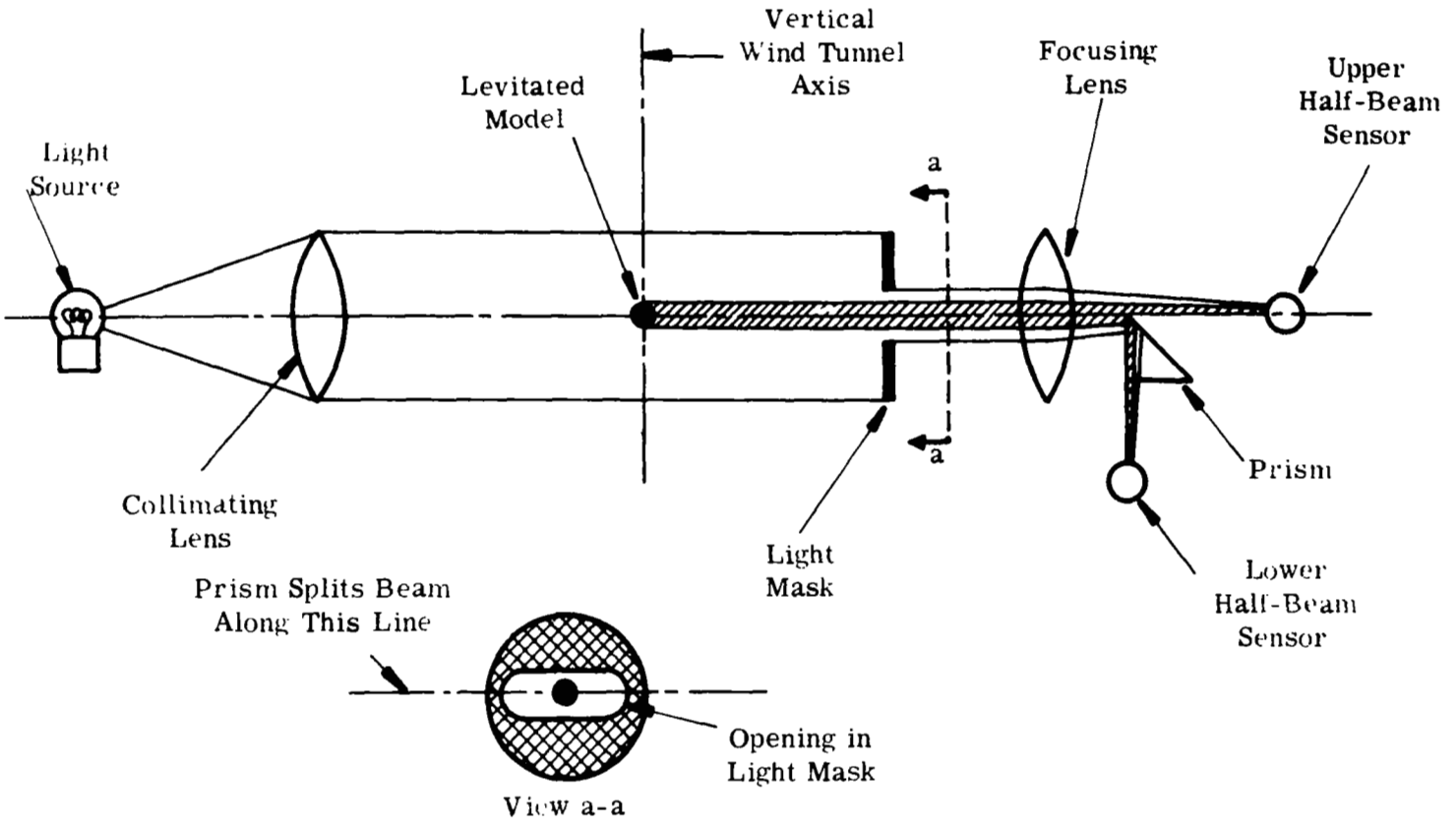

Figure 12. Sketch Showing Optical Model Position Sensor Operation

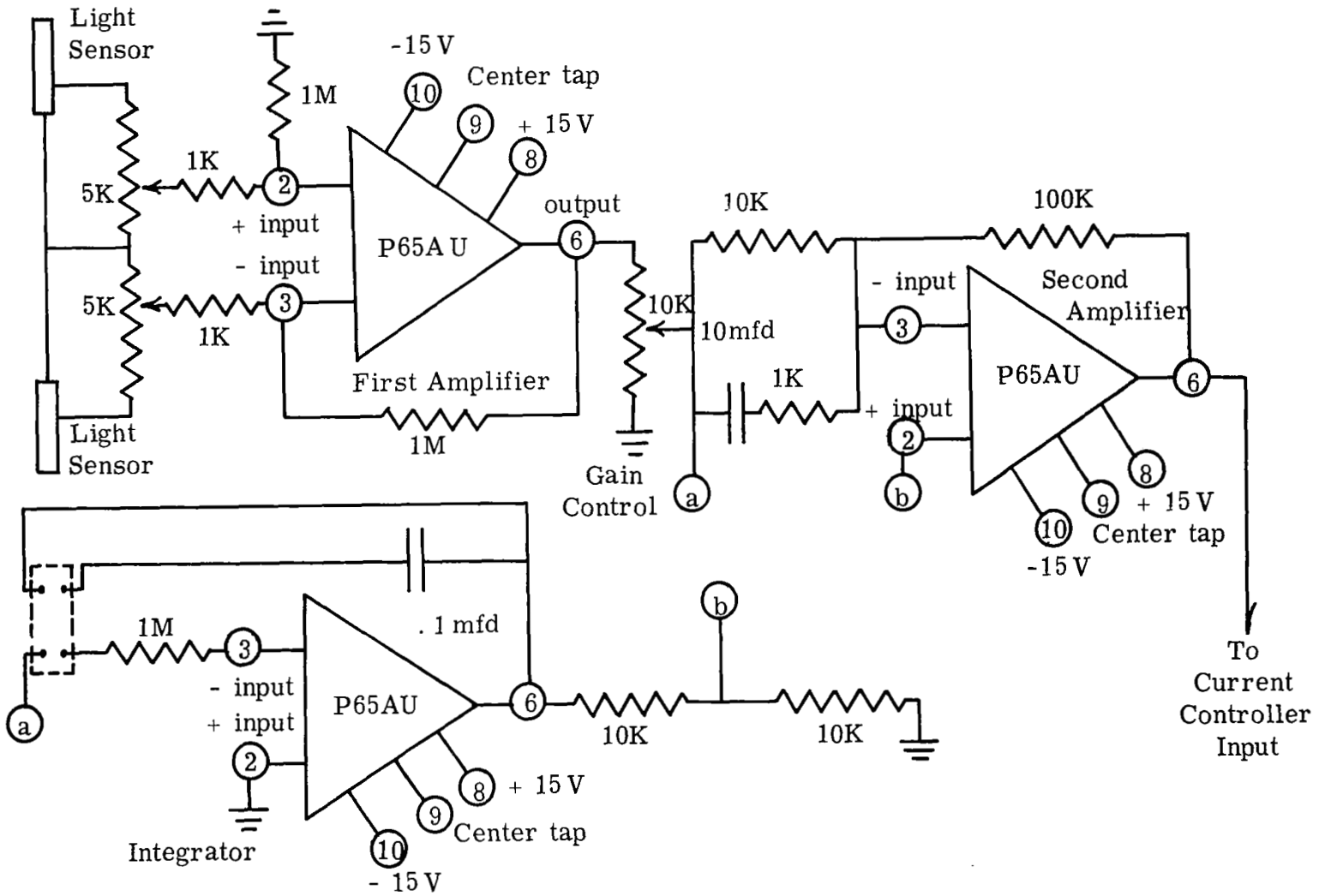

Figure 13. Compensation Unit Circuit

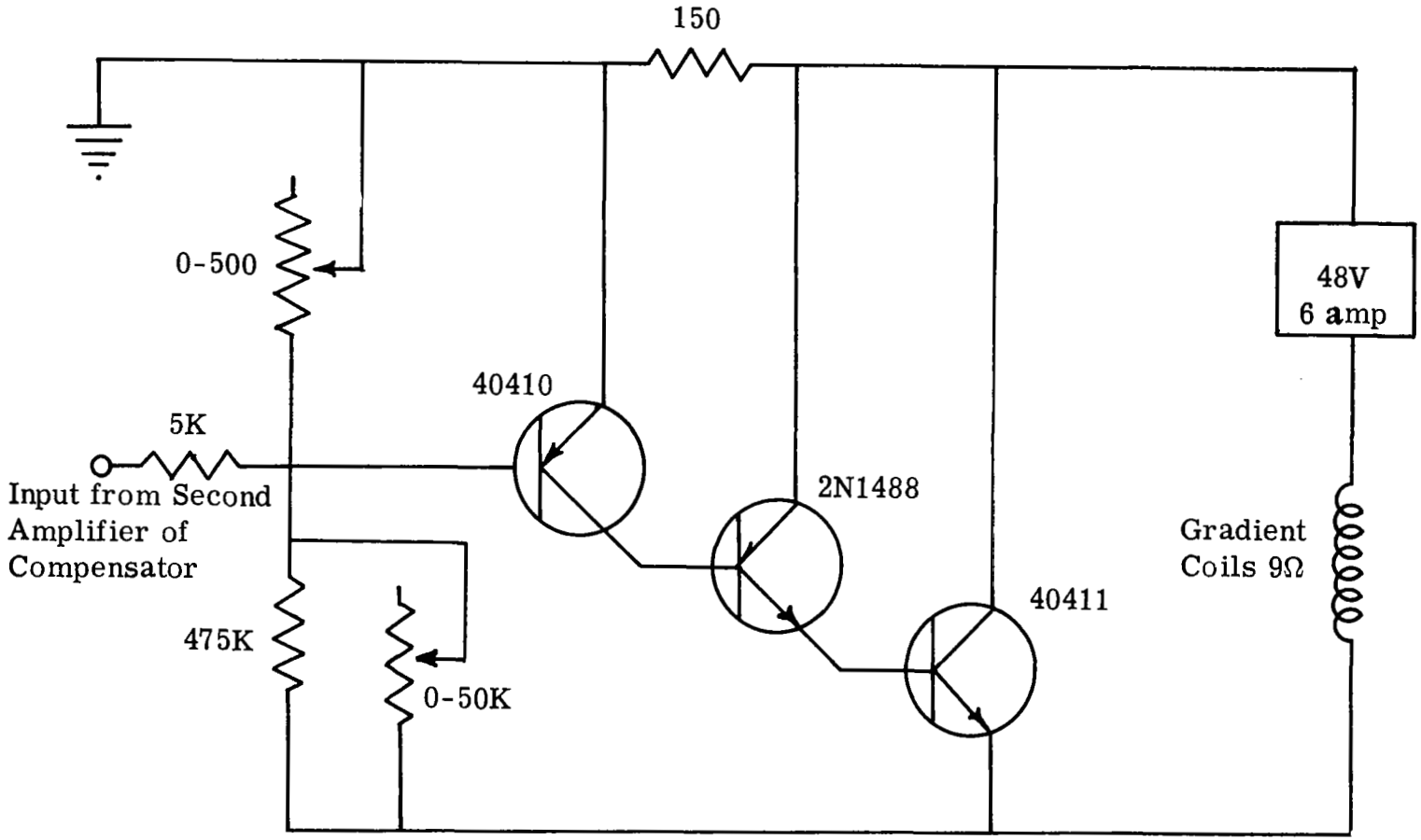

Figure 14. Current Controller Circuit

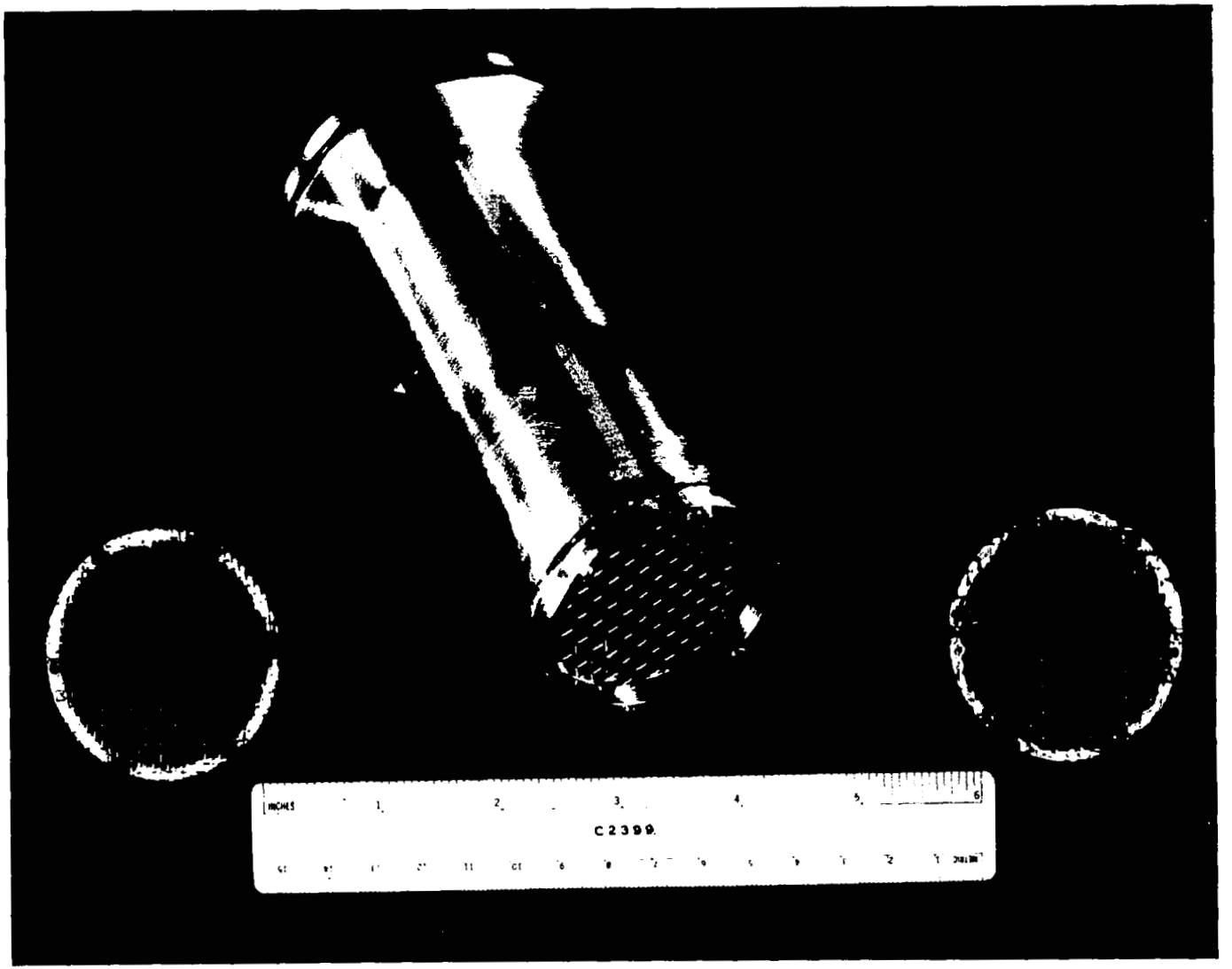

Figure 15. Photograph of Grid Holder Sleeve and Grid Rings

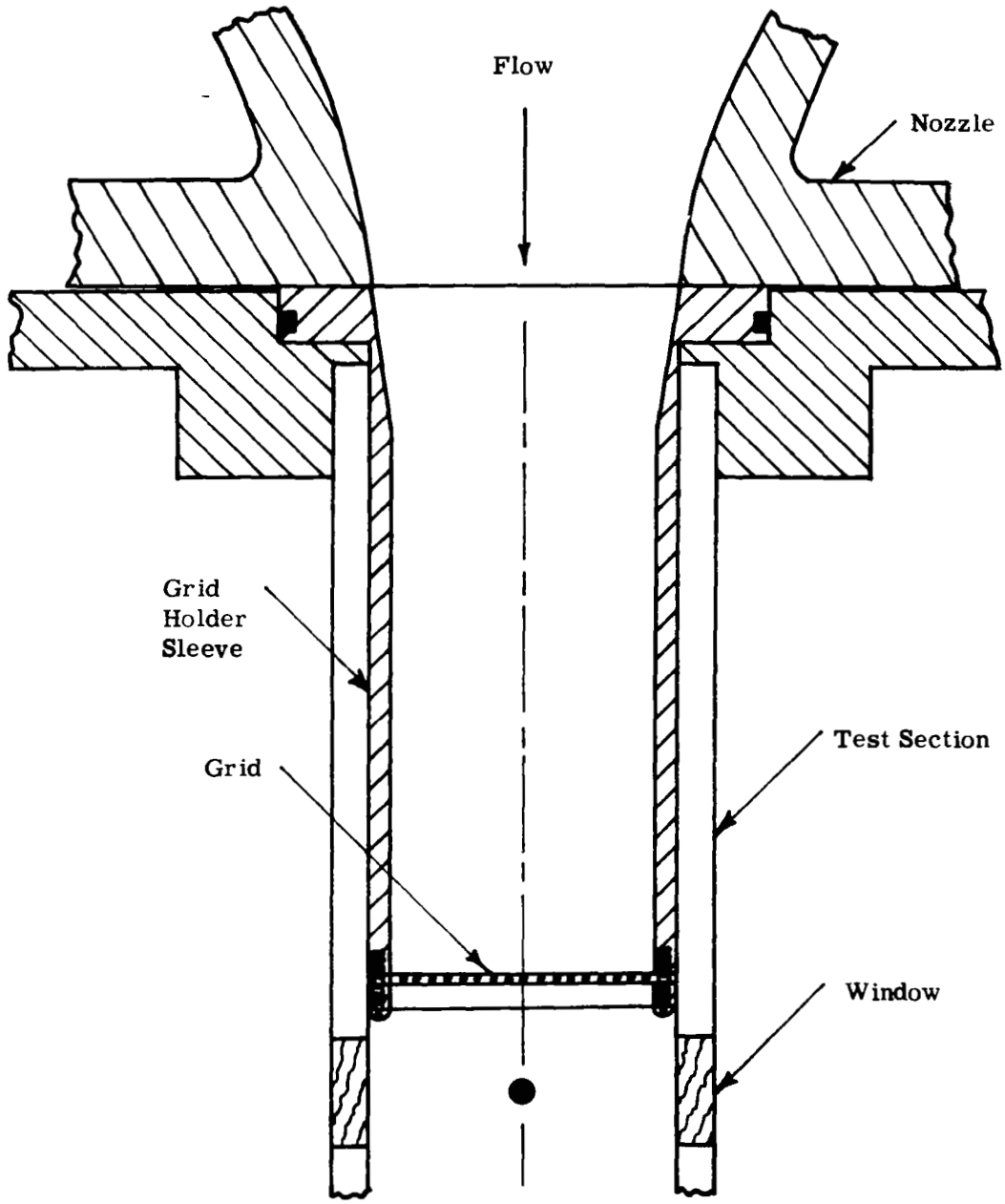

Figure 16. Sketch of Grid Holder Sleeve in Test Section

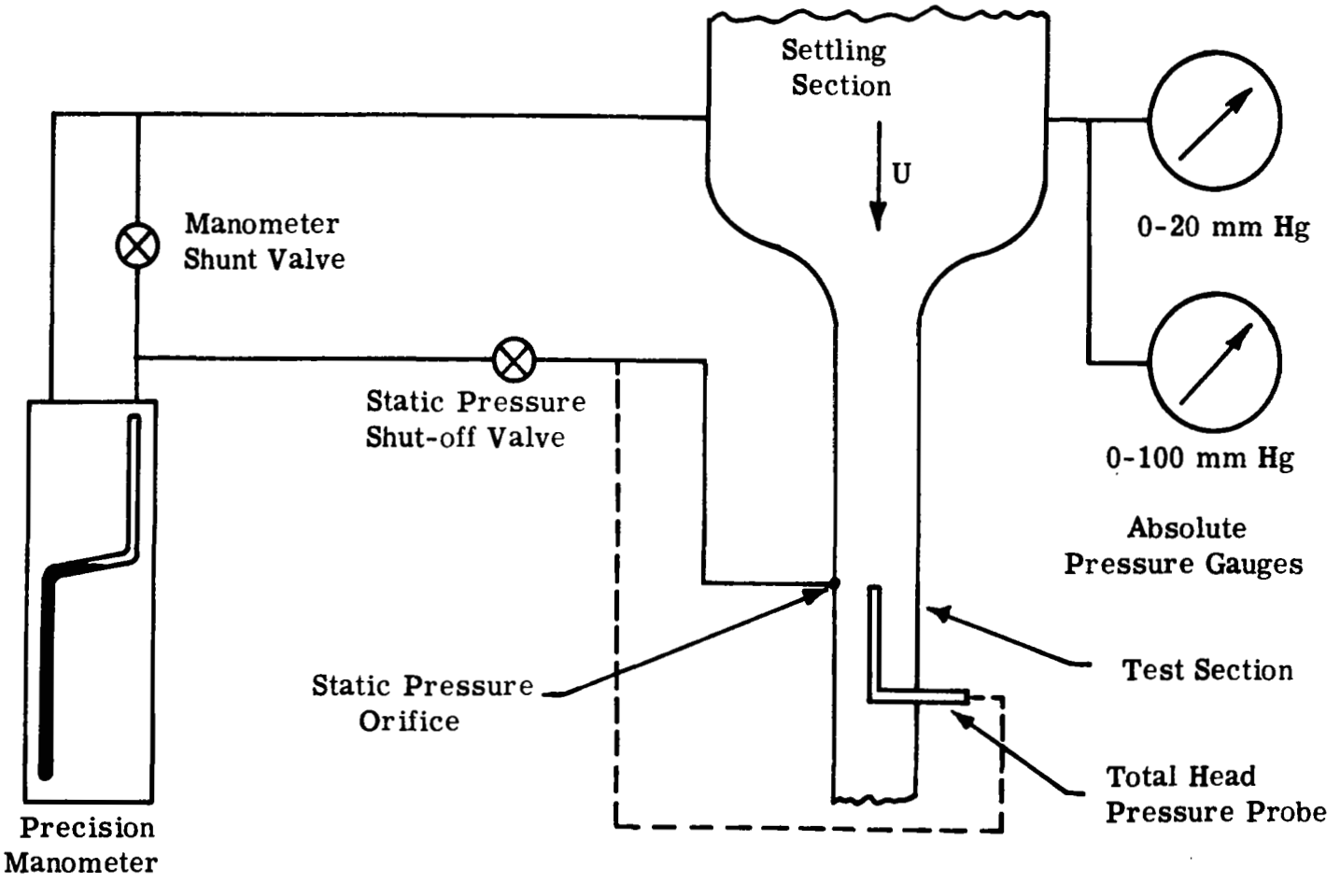

Figure 17. Sketch of Pressure Instrumentation System

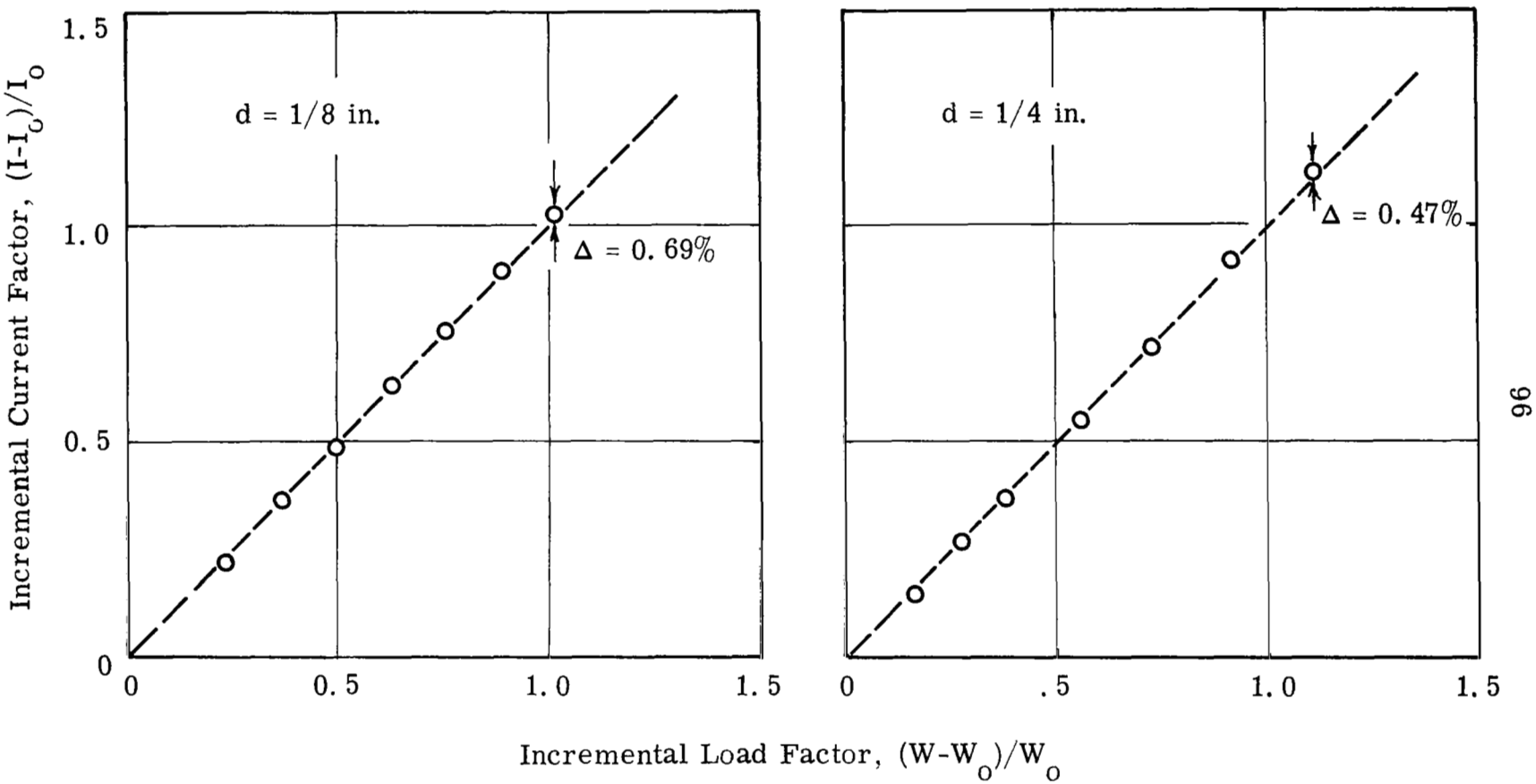

Figure 18. Load Calibration of Magnetic Suspension System

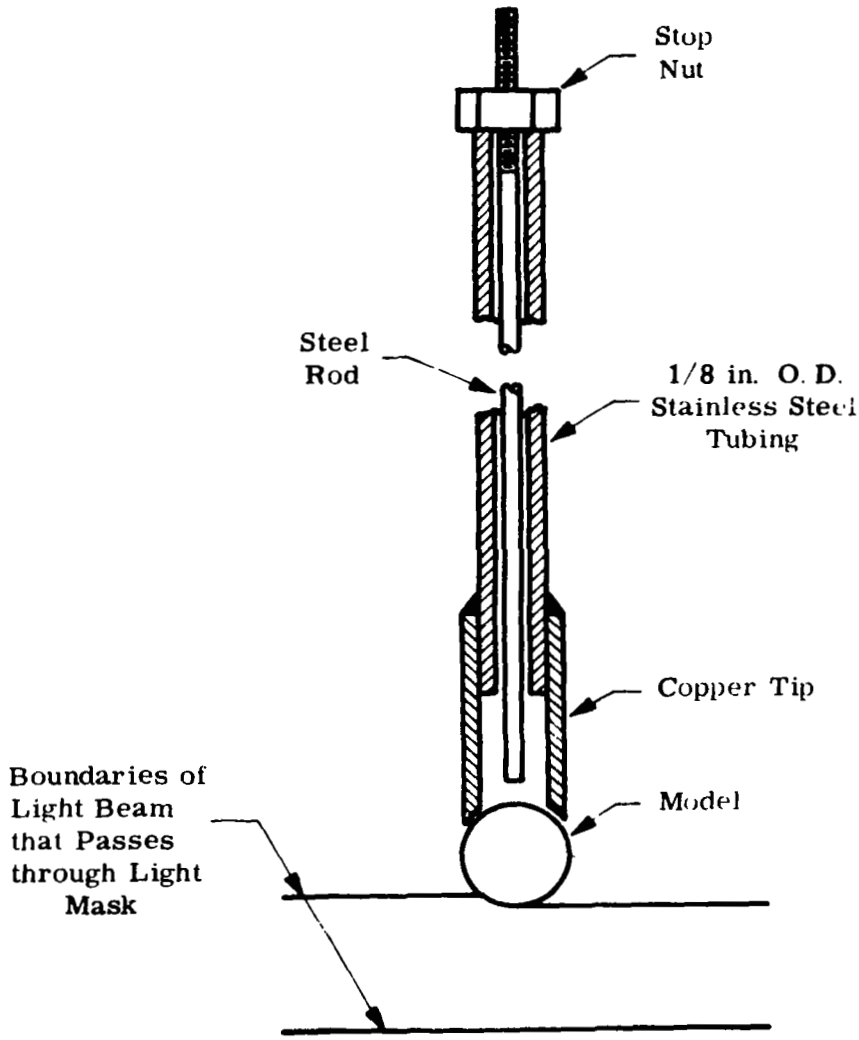

Figure 19. Sketch of Magnetic Model Insertion Probe

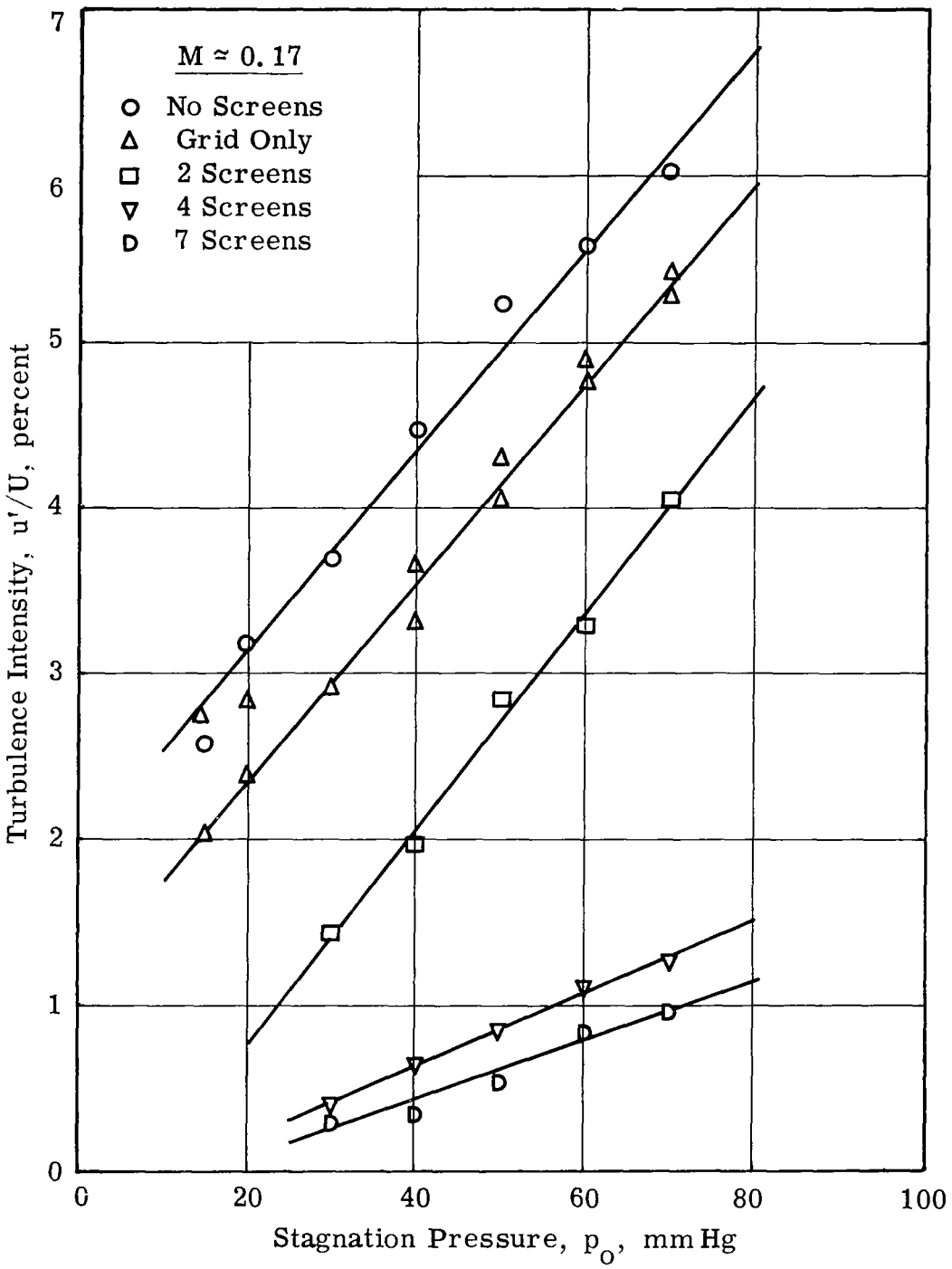

Figure 20. Test Section Turbulence Intensity

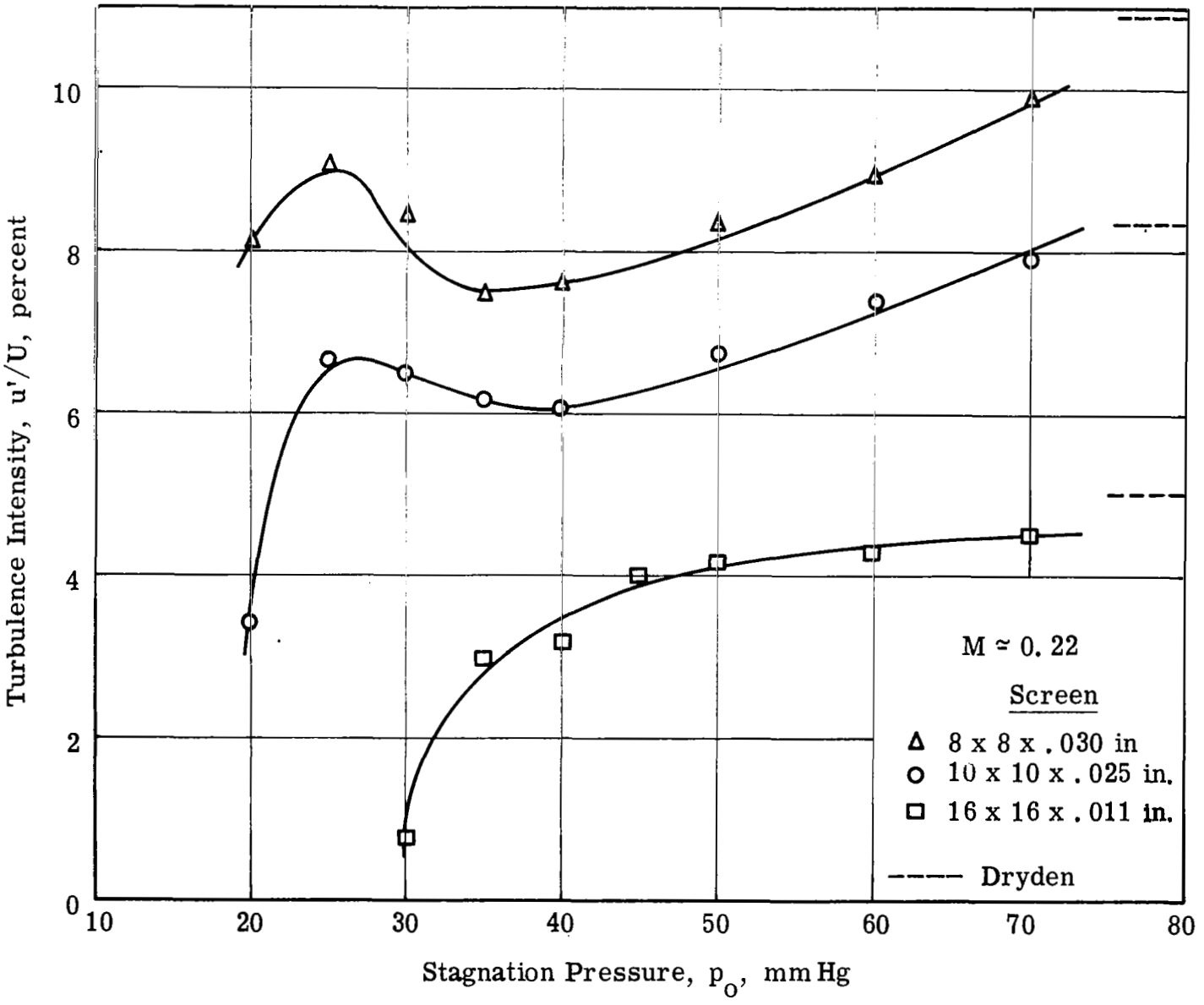

Figure 21. Test Section Turbulence Intensity

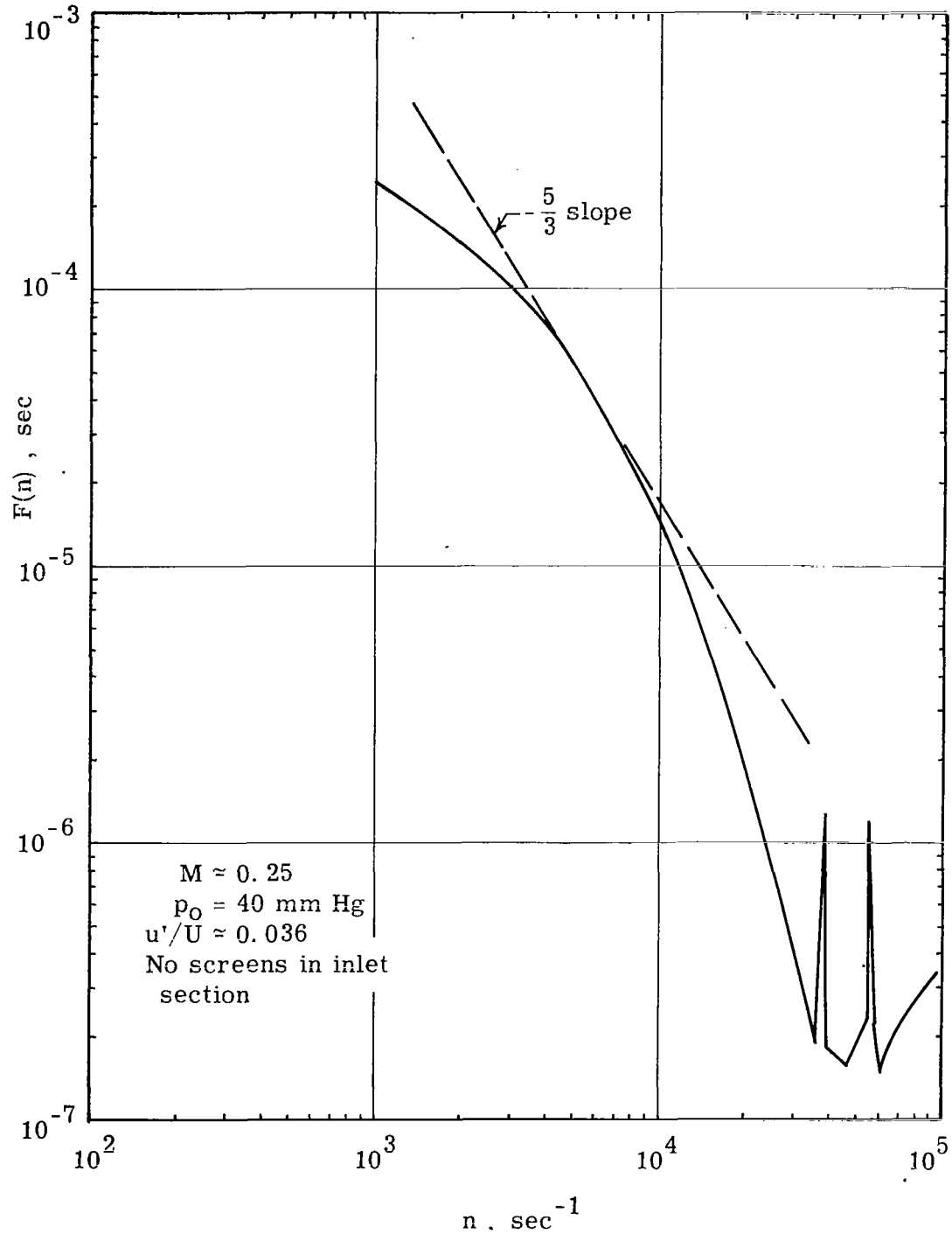

Figure 22a. Turbulence Spectrum; M ≈ 0. 25, No Screens in Inlet Section.

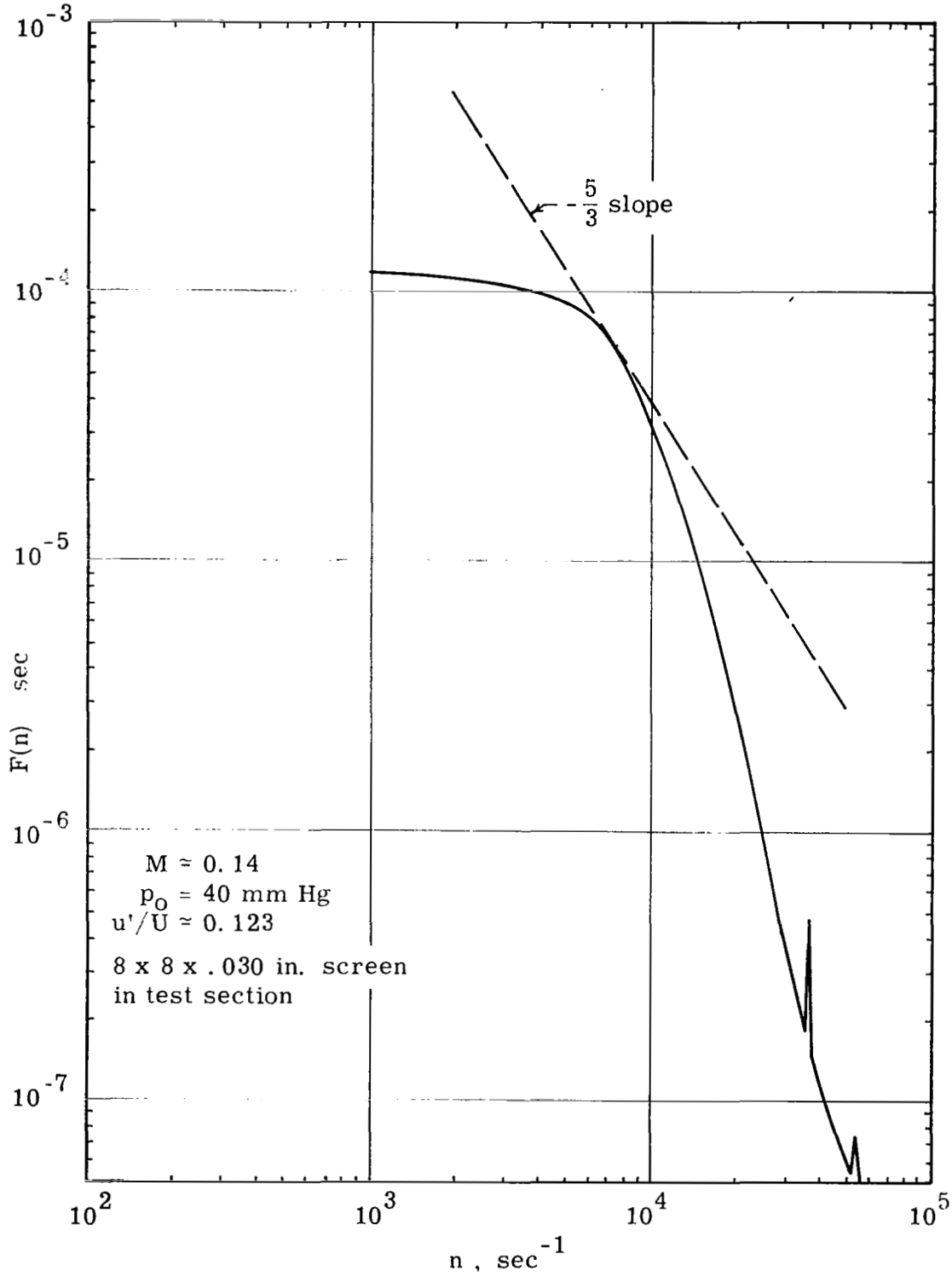

Figure 22b. Turbulence Spectrum; M ≈ 0.14, 8 x 8 x .030 in. Screen in Test Section

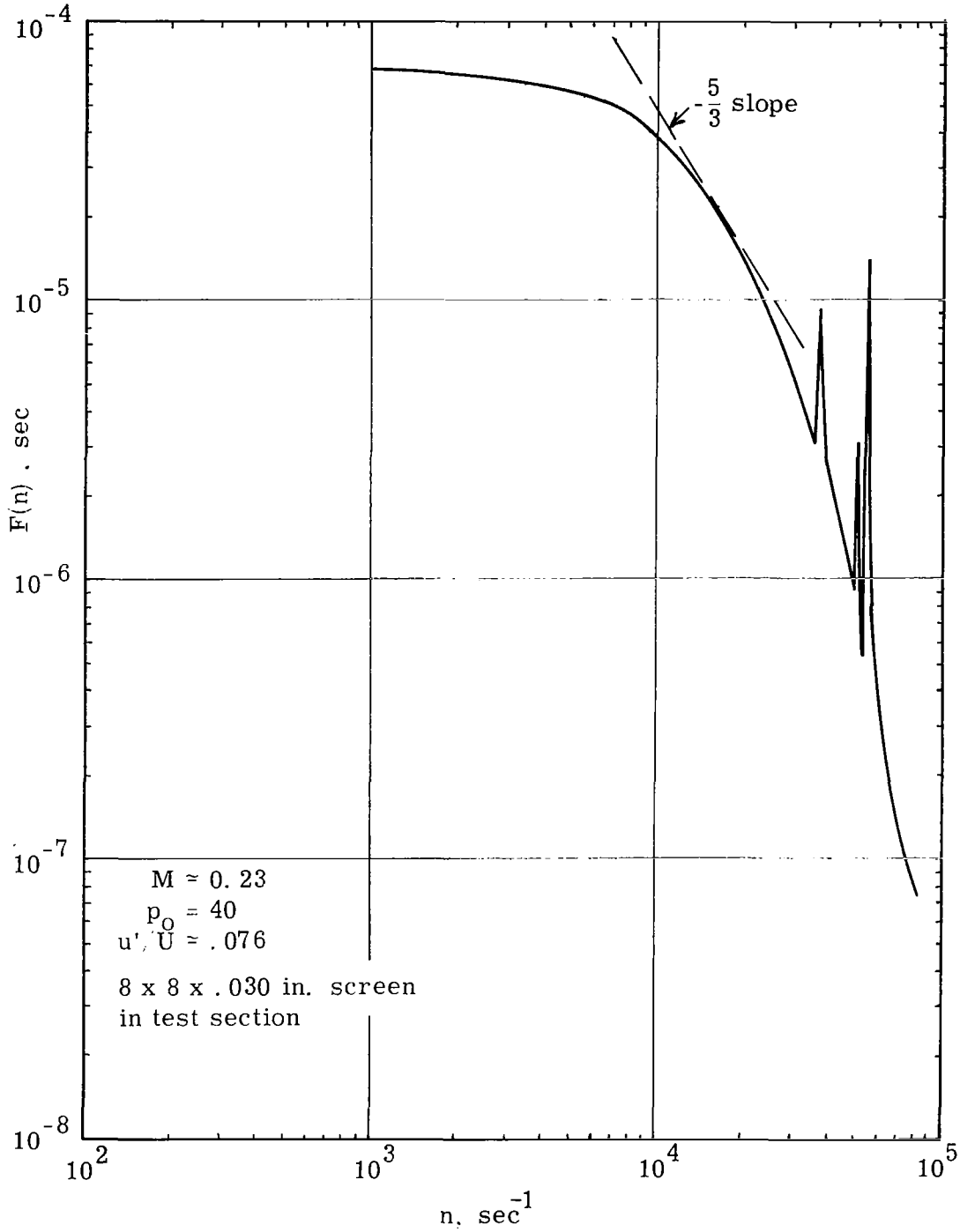

Figure 22c. Turbulence Spectrum; M ≈ 0.23, 8 x 8 x .030 in. screen in Test Section

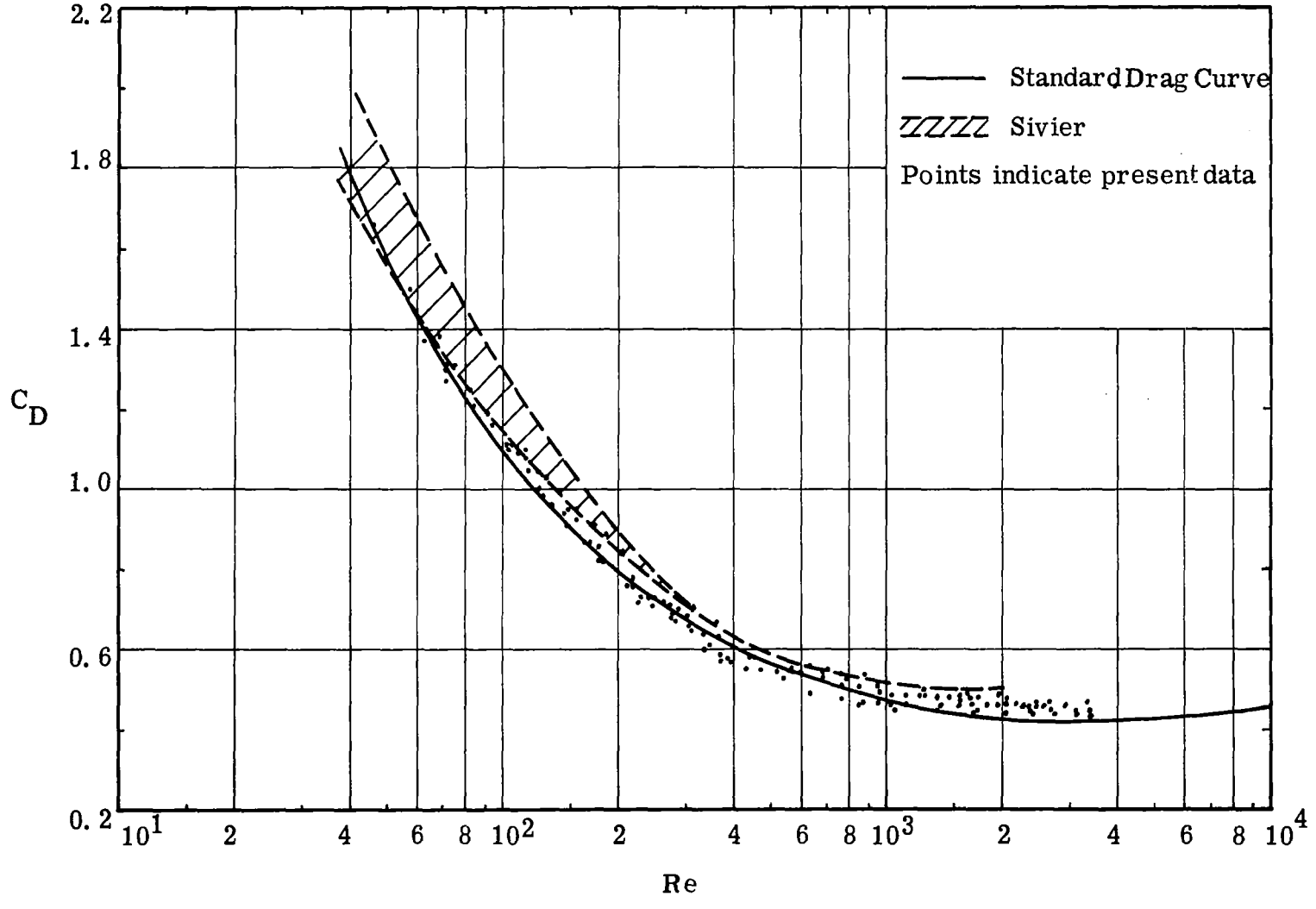

Figure 23. Sphere Drag Coefficients; M ≈ 0.17, u'/U < .012

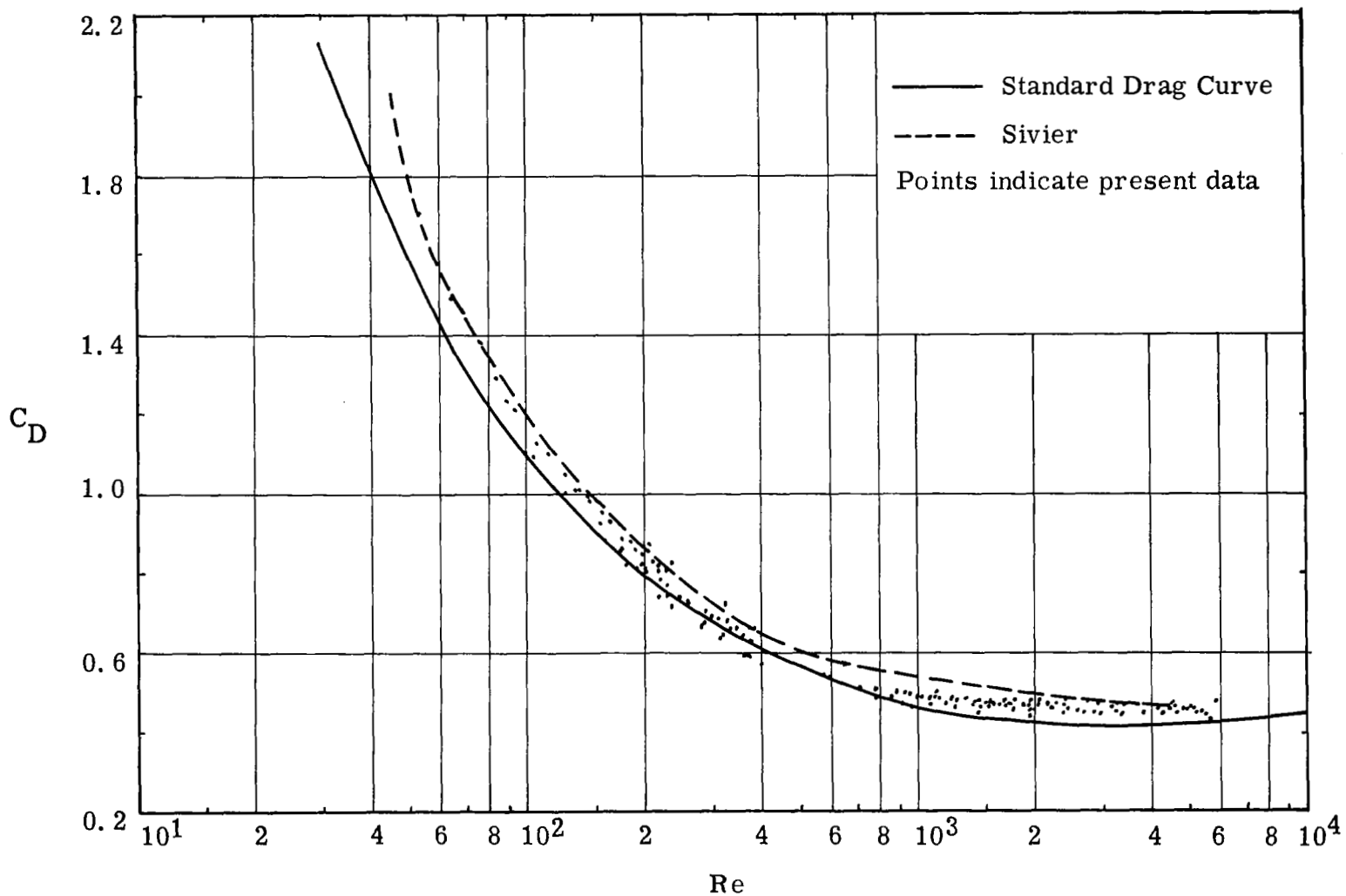

Figure 24. Sphere Drag Coefficients; M ≃ 0.23, u'/U < .01

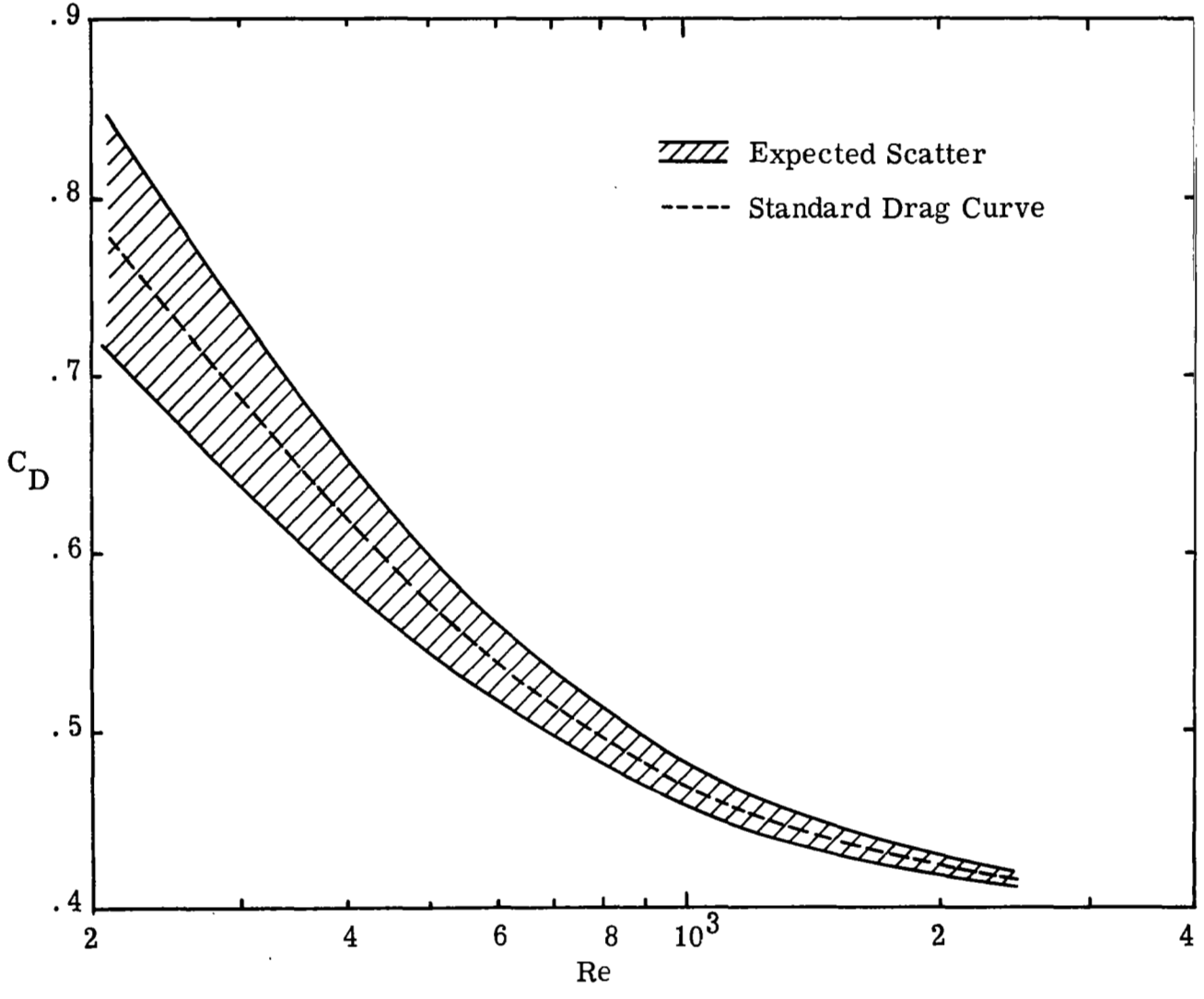

Figure 25. Maximum Expected Scatter due to Measurement Uncertainty; M ≃ 0.17, d = 3/16 in.

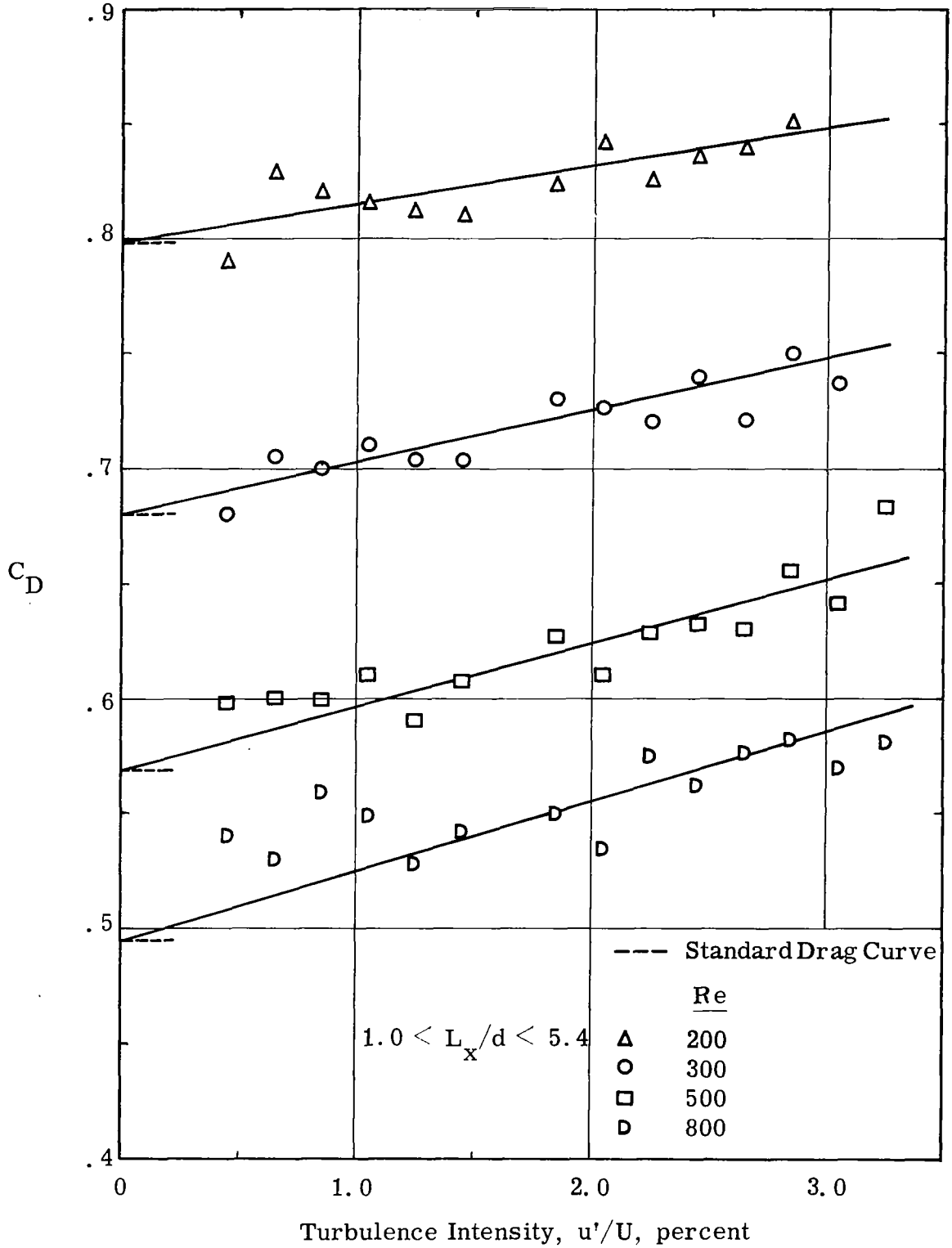

Figure 26. Drag Coefficient of Spheres in Turbulent Flow

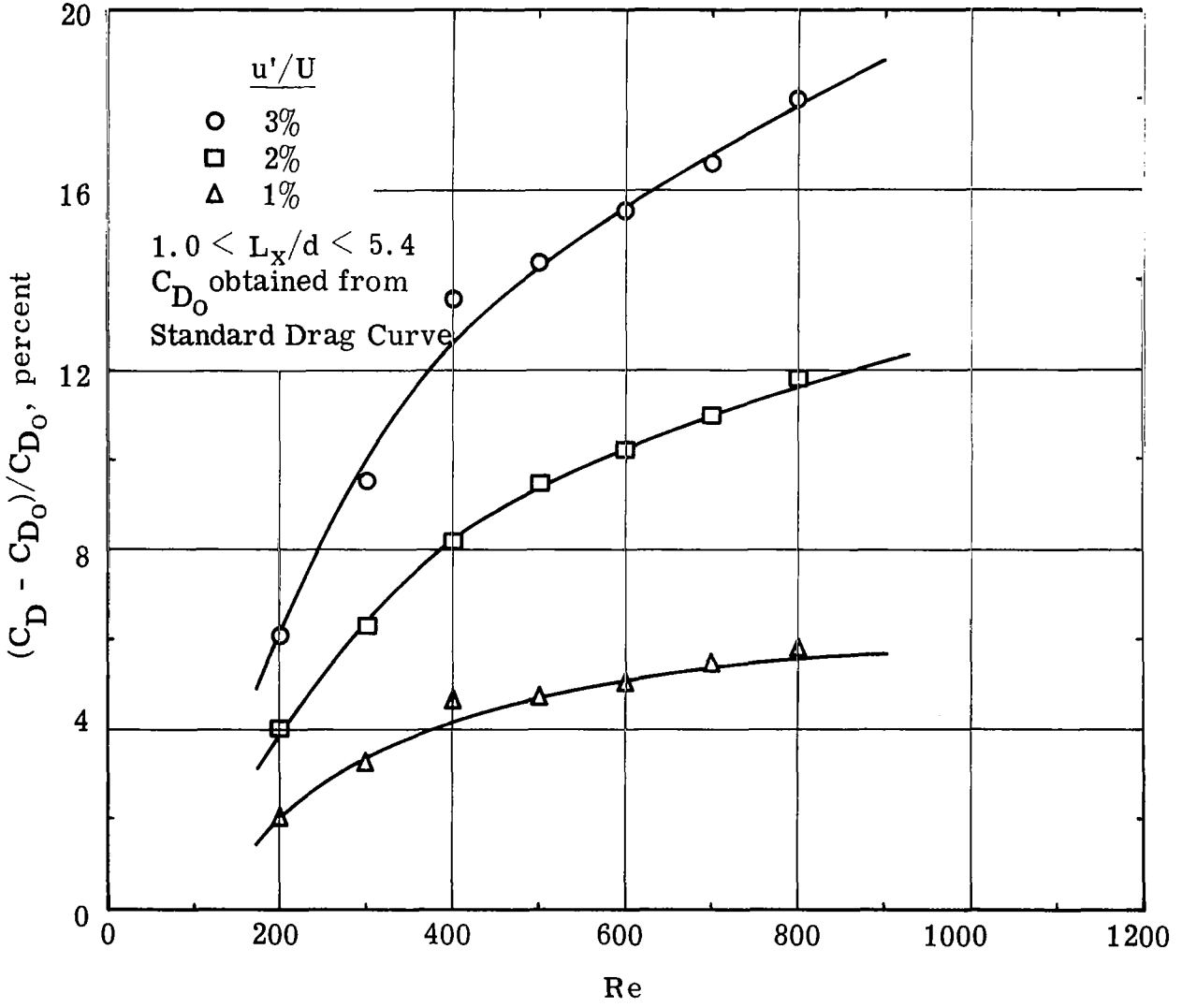

Figure 27. Correlation of Turbulent Drag Rise with Reynolds Number

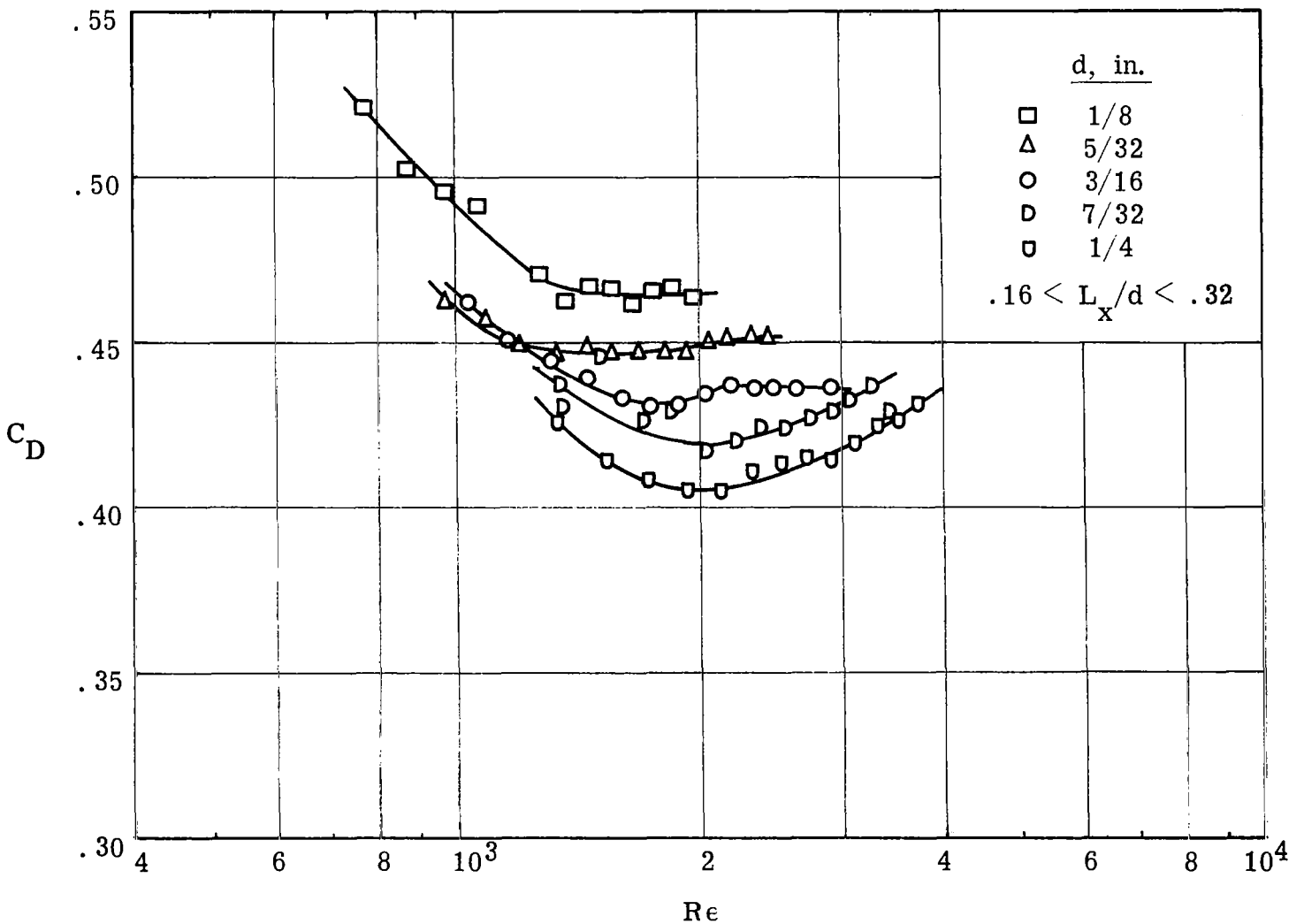

Figure 28a. Drag Coefficient of Spheres in Turbulent Flow; M ≈ 0.21, $.030 < u'/U < .045$

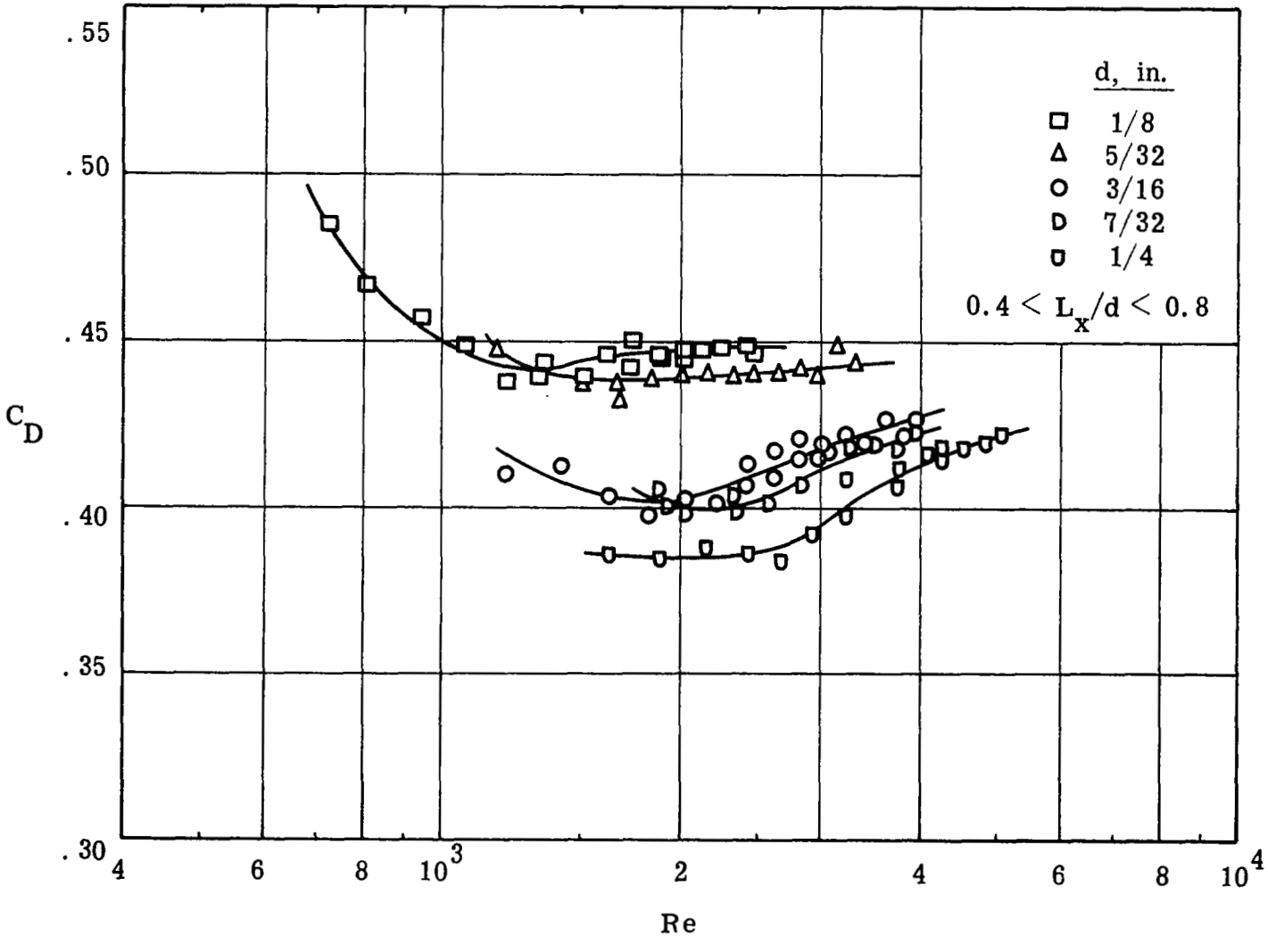

Figure 28b. Drag Coefficient of Spheres in Turbulent Flow; M ≈ 0.31, $.054 < u'/U < .070$.

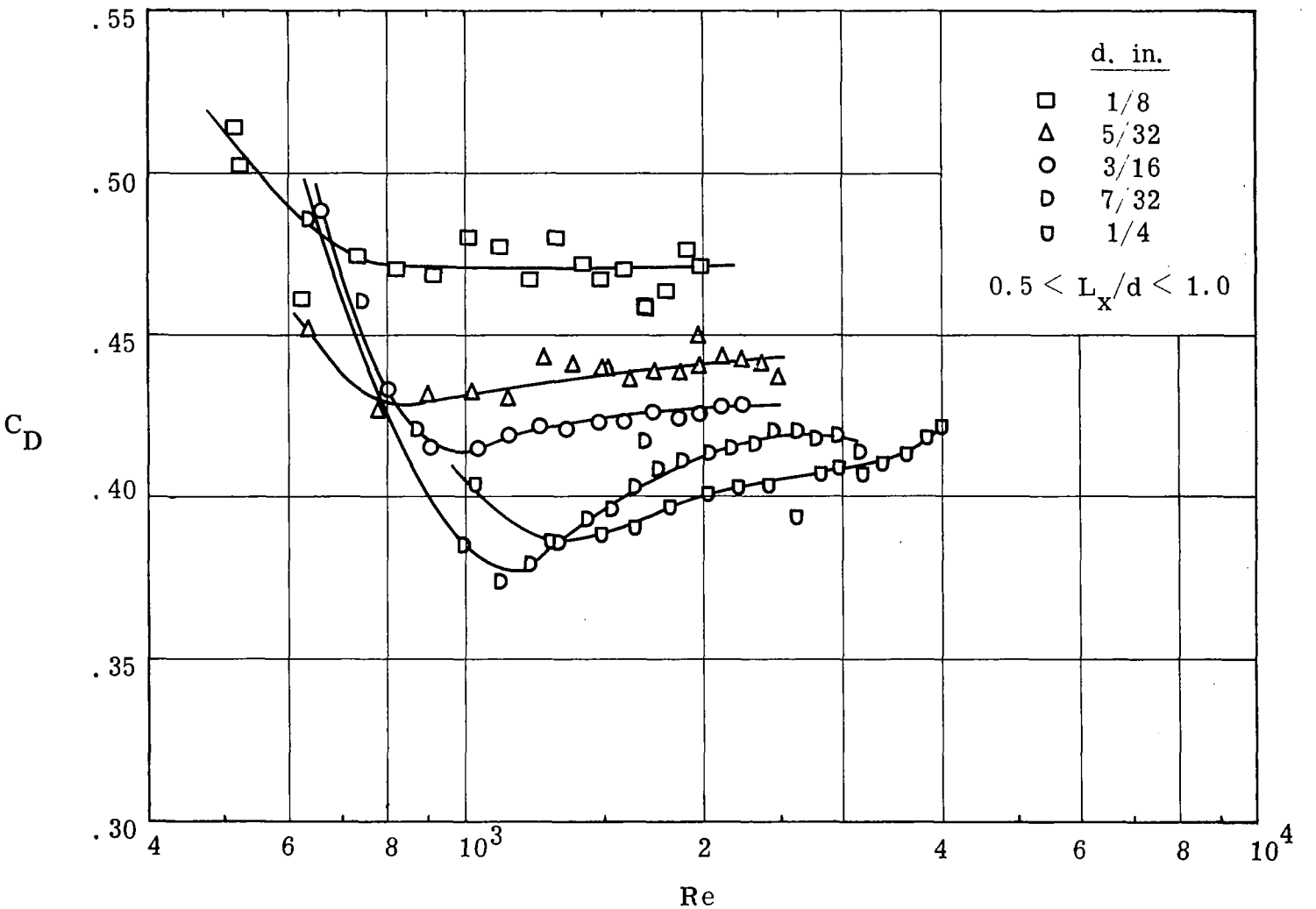

Figure 28c. Drag Coefficient of Spheres in Turbulent Flow; $M \approx 0.22$, $.058 < u'/U < .079$.

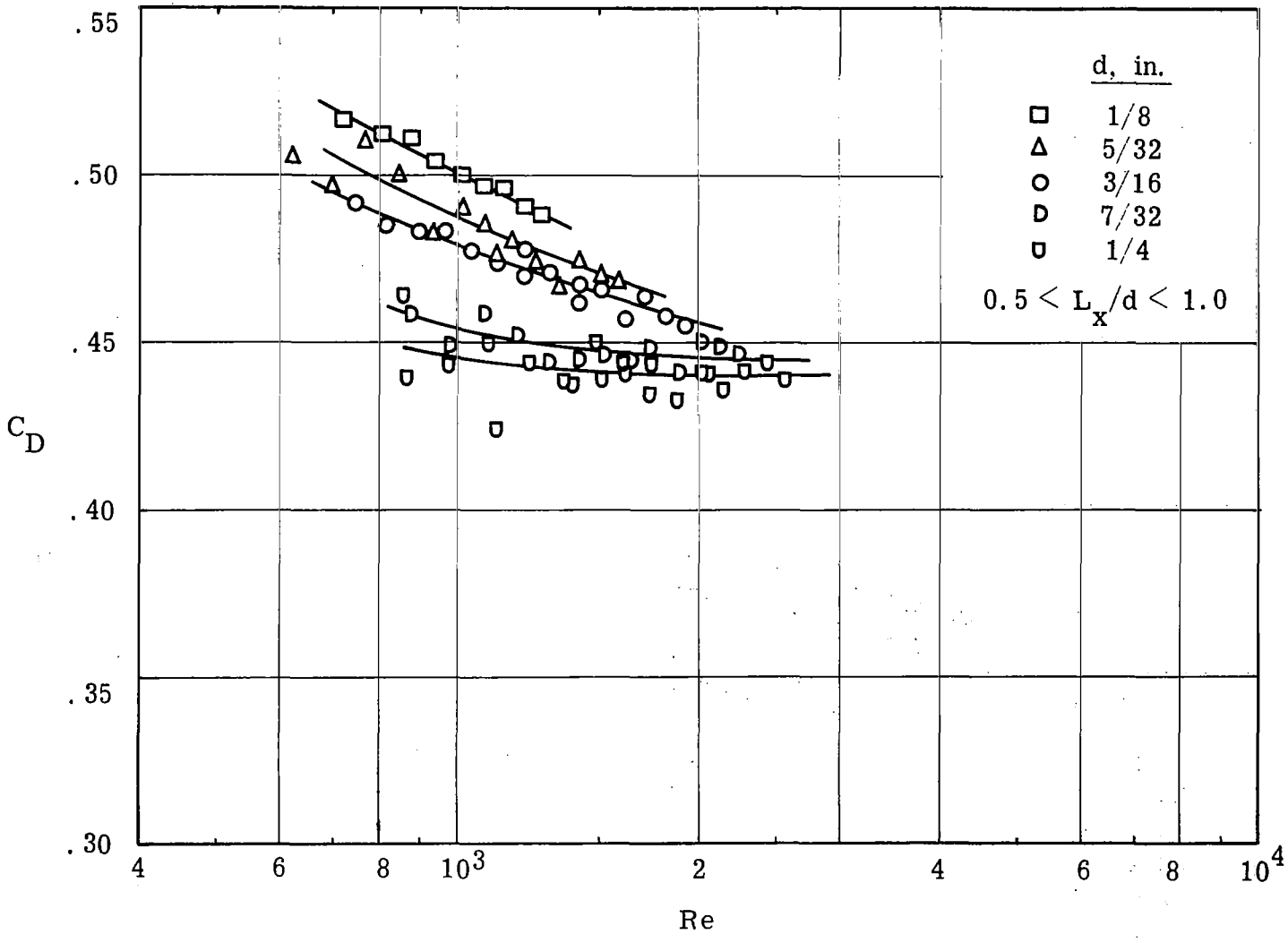

Figure 28d. Drag Coefficient of Spheres in Turbulent Flow; M ≈ 0.13, $.085 < u'/U < .089$.

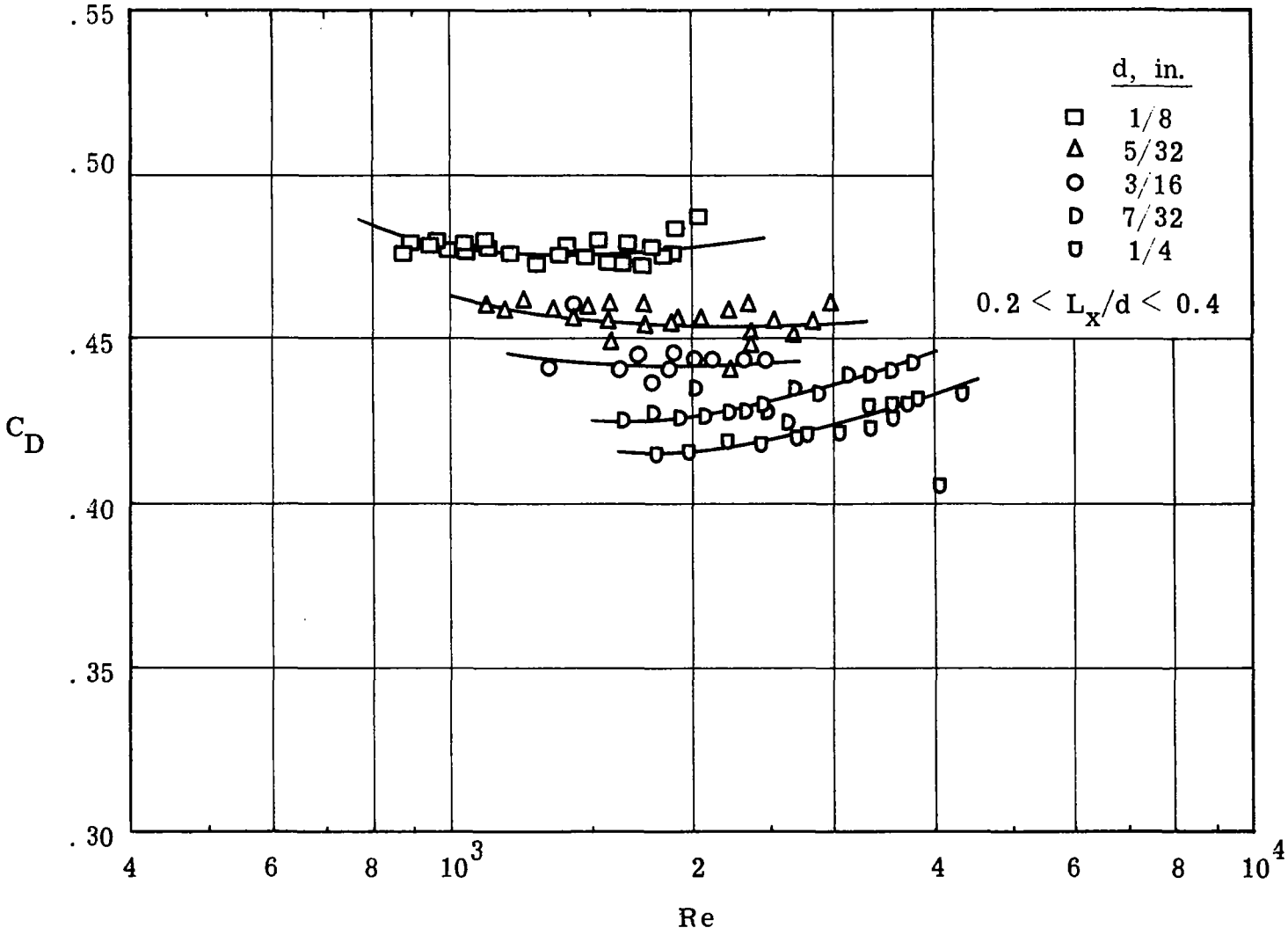

Figure 28e. Drag Coefficient of Spheres in Turbulent Flow; $M \approx 0.33, .088 < u'/U < .13$.

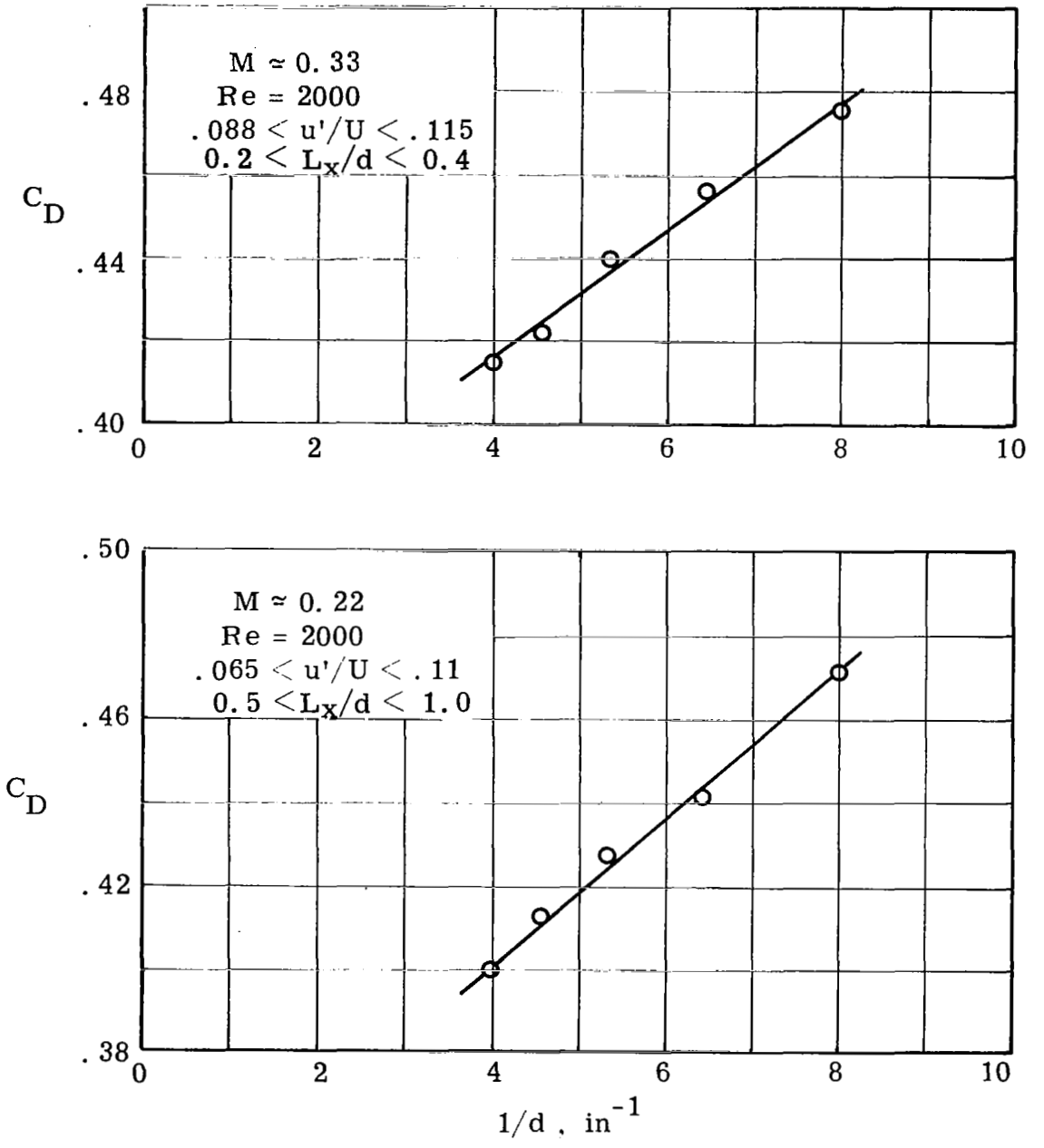

Figure 29. Effect of Sphere Diameter on Drag Coefficient

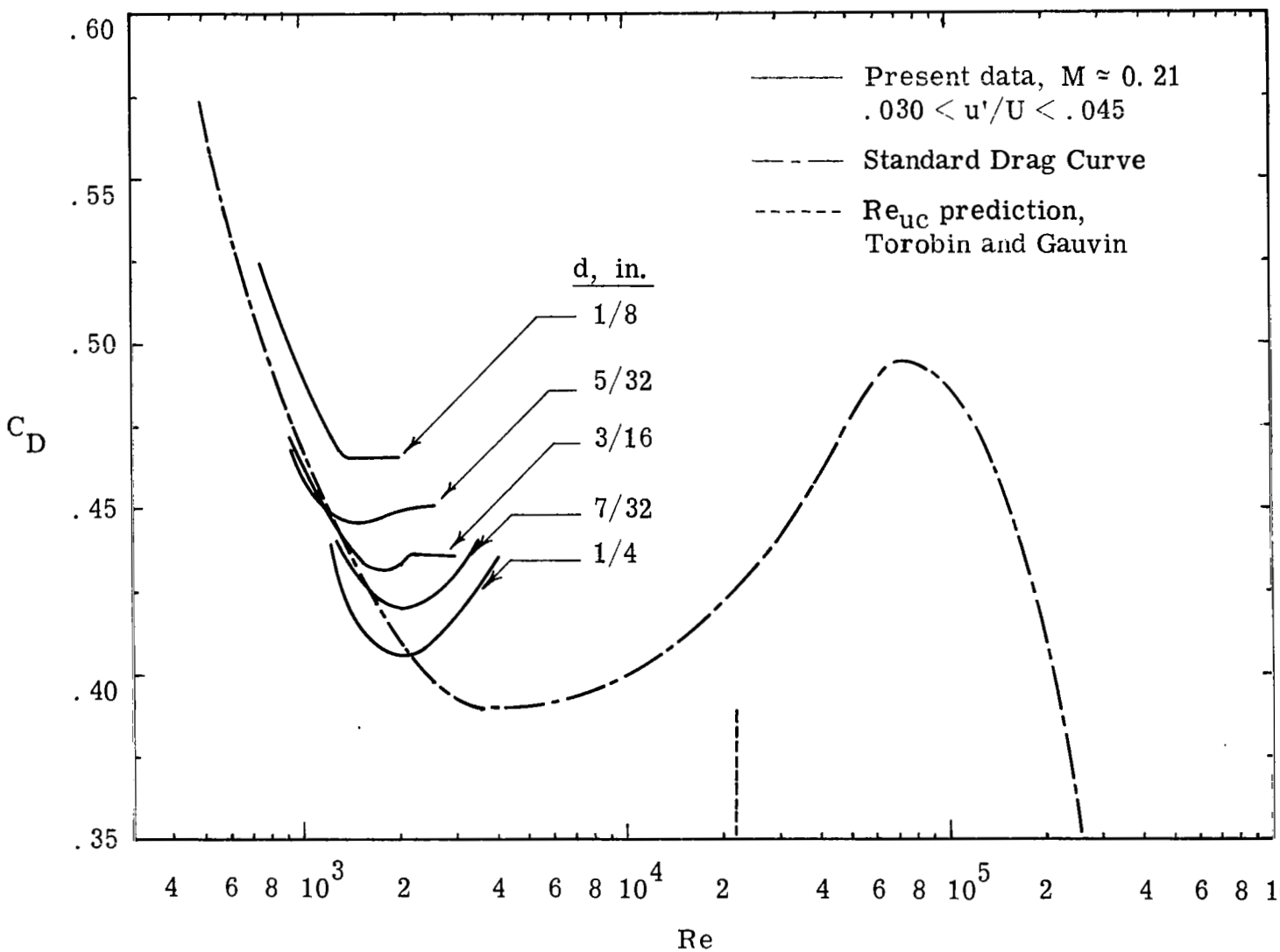

Figure 30. Drag Coefficient of Spheres in Turbulent Flow; M ≈ 0. 21, . 030 < u'/U < . 045.

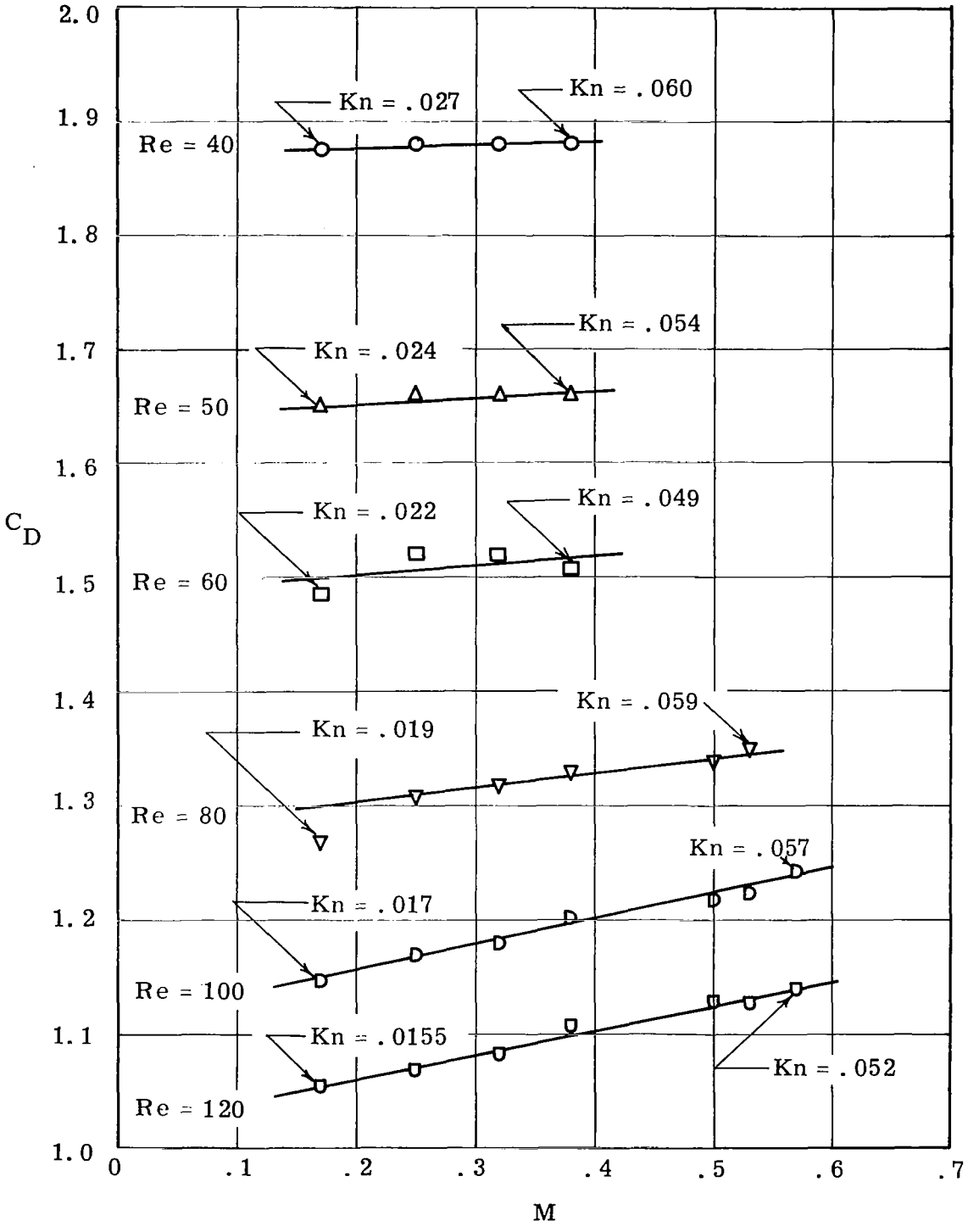

Figure 31. Effect of Mach Number on Drag Coefficient; $40 \leq Re \leq 120$.

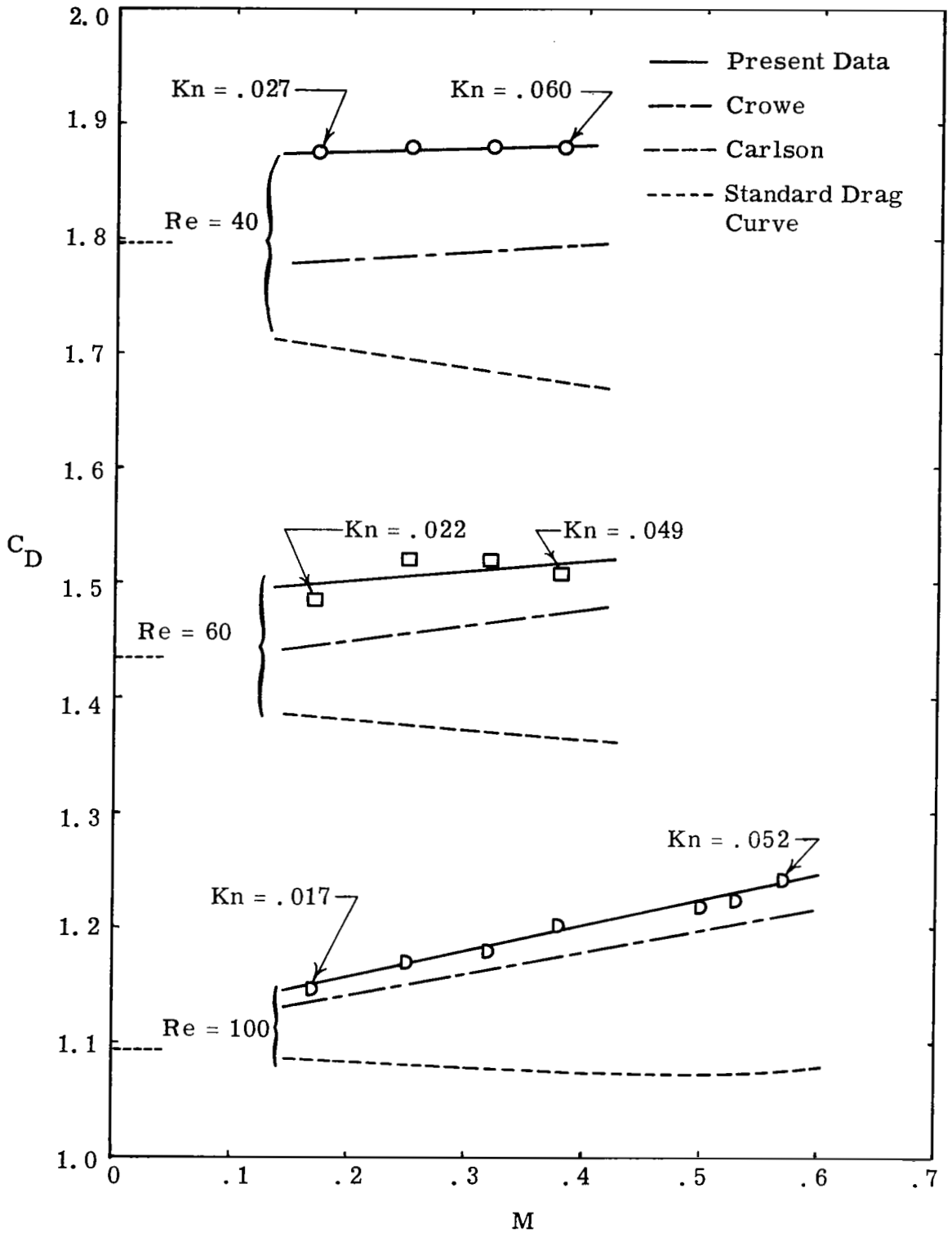

Figure 32. Effect of Mach Number on Drag Coefficient; Re = 40, 60, 100

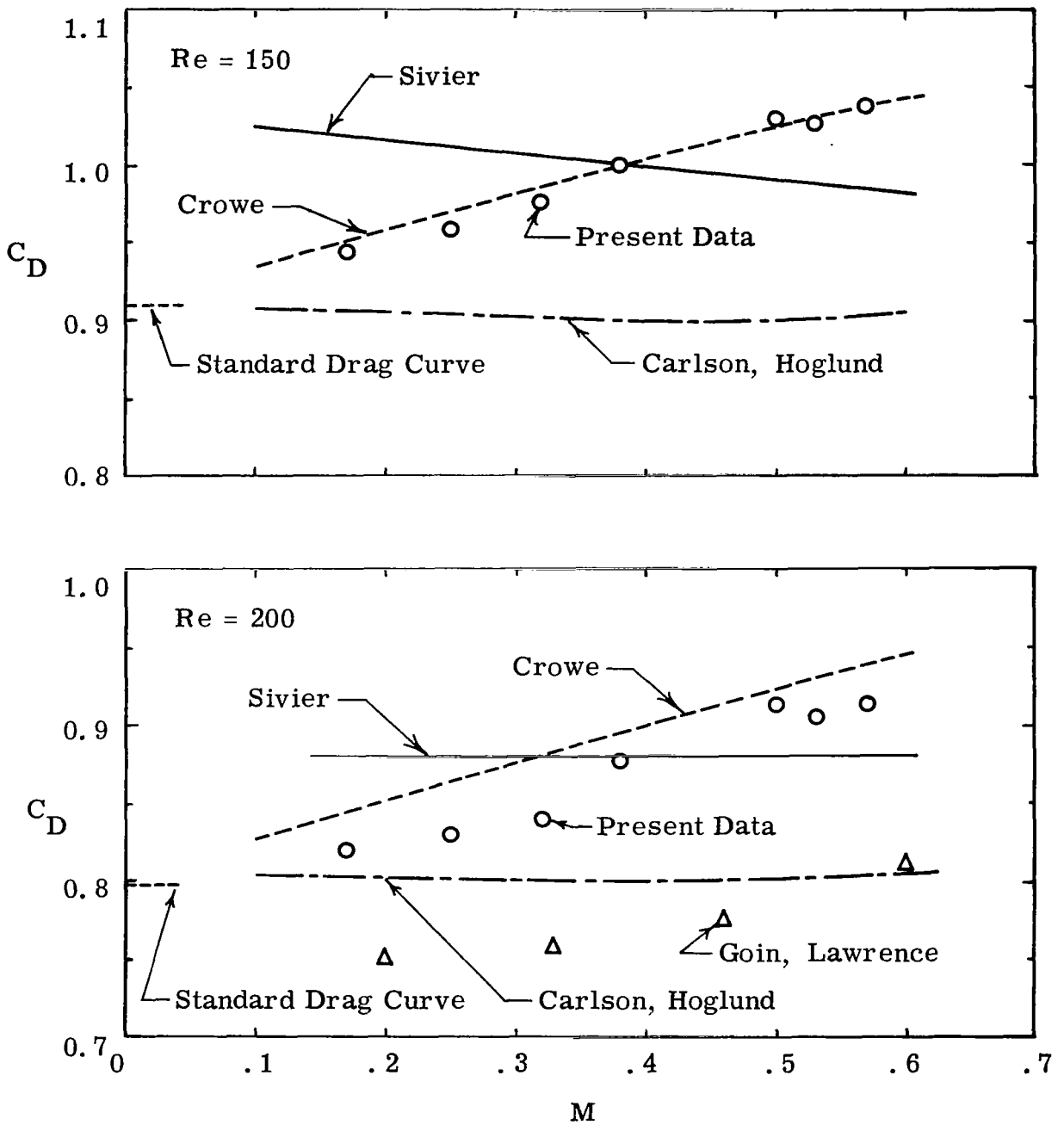

Figure 33. Effect of Mach Number on Drag Coefficient; Re = 150, 200.

REFERENCES

1. Carlson, D. J. and Hoglund, R. F., Particle Drag and Heat Transfer in Rocket Nozzles," AIAA J., Vol. 2, 1964, pp. 1980-1984.

2. Crowe, C. T., "Dynamics of Two Phase Flow in Rocket Nozzles," Fourth Quarterly Technical Progress Report, United Technology Corporation, Contract No. NOw-61-0760-c, May 26, 1962.

3. Torobin, L. B. and Gauvin, W. H., "The Drag Coefficients of Single Spheres Moving in Steady and Accelerated Motion in a Turbulent Fluid," AIChE. J., Vol. 7, 1961, pp. 615-619.

4. Clamen, A. and Gauvin, W. H., "Effects of Turbulence on the Drag Coefficients of Spheres in a Supercritical Flow Regime," AIChE. J., Vol. 15, 1969, pp. 184-189.

5. Cajori, F., Newton's Principia, University of California Press, Berkeley, California, 1946, pp. 355-366.

6. Torobin, L. B. and Gauvin, W. H., "Fundamental Aspects of Solids-Gas Flow, Part I: Introductory Concepts and Idealized Sphere Motion in Viscous Regime," Can. J. Chem. Eng., Vol. 37, 1959, pp. 129-141.

7. Torobin, L. B. and Gauvin, W. H., "Fundamental Aspects of Solids-Gas Flow, Part II: The Sphere Wake in Steady Laminar Fluids," Can. J. Chem. Eng., Vol. 37, 1959, pp. 167-176.

8. Torobin, L. B. and Gauvin, W. H., "Fundamental Aspects of Solids-Gas Flow, Part III: Accelerated Motion of a Particle in a Fluid," Can. J. Chem. Eng., Vol. 37, 1959, pp. 224-236.

9. Torobin, L. B. and Gauvin, W. H., "Fundamental Aspects of the Solids-Gas Flow, Part IV: The Effects of Particle Rotation, Roughness and Shape," Can. J. Chem. Eng., Vol. 38, 1960, pp. 142-153.

10. Torobin, L. B. and Gauvin, W. H., "Fundamental Aspects of Solids-Gas Flow, Part V: The Effects of Fluid Turbulence on the Particle Drag Coefficient," Can. J. Chem. Eng., Vol. 38, 1960, pp. 189-200.

11. Torobin, L. B. and Gauvin, W. H., "Fundamental Aspects of Solids-Gas Flow, Part VI: Multiparticle Behavior in Turbulent Fluids," Can. J. Chem. Eng., Vol. 39, 1961, pp. 113-120.

12. Roos, F. W., "An Experimental Investigation of the Unsteady Flows about Spheres and Disks," Ph. D. Thesis, The University of Michigan, Ann Arbor, Michigan, 1968.

13. Lamb, H., Hydrodynamics, 6th ed., Dover Publications, Inc., New York, 1945, p. 609.

14. Jenson, V. G., "Viscous Flow Around a Sphere at Low Reynolds Numbers (< 40)," Proc. Roy. Soc. (London), Ser. A, Vol. 249, 1959, pp. 346-366.

15. Taneda, S., "Studies of Wake Vortices (III), Experimental Investigation of the Wake Behind a Sphere at Low Reynolds Numbers," Rept. Research Institute of Applied Mechanics of Japan, Vol. 4, 1956, pp. 99-105.

16. Margarvey, R. H. and Bishop, R. L., "Transition Ranges for Three-Dimensional Wakes," Can. J. Phys., Vol. 39, 1961, pp. 1418-1422.

17. Nemenyi, P., "The Different Approaches to the Study of Propulsion of Granular Materials and the Value of their Coordination," Trans. Am. Geophys. Union, Vol. 21, 1940, pp. 633-647.

18. Lunnon, R. G., "Fluid Resistance to Moving Spheres," Proc. Roy. Soc. (London), Ser. A, Vol. 118, 1928, pp. 680-694.

19. Schmidt, F. S., "Zur beschleunigten bewegung kügelformiger Körper in widerstehenden mitteln," Ann. Physik, Ser. IV, Vol. 61, 1920, pp. 633-664.

20. Liebster, H., "Uber den Widerstand von Kugeln," Ann. Physik, Vol. 82, 1927, pp. 541-562.

21. Sivier, K. R., "Subsonic Sphere Drag Measurements at Intermediate Reynolds Numbers," Ph. D. Thesis, The University of Michigan, Ann Arbor, Michigan, 1967.

22. Möller, W., "Experimentelle Untersuchungen zur Hydrodynamik der Kugel," Z. Physik, Vol. 39, 1938, pp. 57-80.

23. Kendall, J.M., Jr., "The Periodic Wake of a Sphere," Jet Propulsion Laboratory, California Institute Technology, Space Programs Summary No. 37-25, Vol. 4, 1964, pp. 251 ff.

24. Winny, H.F., "The Vortex System Generated behind a Sphere Moving through a Viscous Fluid," Aeronautical Research Council R and M, No. 1531, 1932.

25. Schmiedel, J., "Experimentelle Unterschungen über die Fallbewegung von Kugeln und Scheiben in reibenden Flüssigkeiten," Z. Physik, Vol. 29, 1928, pp. 593-610.

26. Morkovin, M.V., "Flow Around a Circular Cylinder— A Kaleidoscope of Challenging Fluid Phenomena," Symposium on Fully Separated Flows, American Society of Mechanical Engineers, New York, 1964, pp. 102-118.

27. Roshko, A., "Experiments on the Flow Past a Circular Cylinder at Very High Reynolds Number," J. Fluid Mech., Vol. 10, 1961, pp. 345-356.

28. Son, J.S. and Hanratty, T.J., "Velocity Gradients at the Wall for Flow around a Cylinder at Reynolds Number from 5×10^3 to 10^5," J. Fluid Mech., Vol. 35, 1969, pp. 353-368.

29. Achenbach, E., "Distribution of Local Pressure and Skin Friction around a Circular Cylinder in Cross-Flow up to Re = 5×10^6," J. Fluid Mech., Vol. 34, 1968, pp. 625-639.

30. Garner, F.H., "Mechanics of Drops and Bubbles in Diffusion Processes," Chem. Ind. (London), 1956, pp. 141-145.

31. Ermisch, H., Abh. d. Aer. Inst. Aachen, Heft 6, Vol. 18, 1927, p. 18 ff.

32. Schiller, L. and Linke, W., "Pressure and Frictional Resistance of a Cylinder at Reynolds Numbers 5,000 to 40,000," NACA TM 715, 1933.

33. Oseen, C.W., "Über die Stokes' sche Formel und über eine verwandte Aufgabe in der Hydrodynamik," Ark. Mat. Astr. Fys., Vol. 6, No. 29, 1910, pp. 1-20.

34. Goldstein, S., "The Steady Flow of a Viscous Fluid Past a Fixed Spherical Obstacle at Small Reynolds Numbers," Proc. Roy. Soc. (London), Ser. A, Vol. 123, 1929, pp. 225-235.

35. Maxworthy, T.J., "Accurate Measurements of Sphere Drag at Low Reynolds Numbers," J. Fluid Mech., Vol. 23, 1965, pp. 369-372.

36. Kawaguti, M., "The Critical Reynolds Number for the Flow Past a Sphere," J. Phys. Soc. Japan, Vol. 10, 1955, pp. 694-699.

37. Kawaguti, M., "An Approximate Solution of the Navier-Stokes Equations for Slow Flow of a Viscous Fluid about a Sphere," Rept. Inst. Sci. Technol., Tokyo, Vol. 8, 1954, pp. 1-3.

38. Hamielec, A.E., Hoffman, T.W., and Ross, L.L., "Numerical Solution of the Navier-Stokes Equation for the Flow Past Spheres: Part I. Viscous Flow Around Spheres with and without Radial Mass Efflux," AIChE J., Vol. 13, 1967, pp. 212-219.

39. Schaaf, S.A. and Chambré, P.L., Flow of Rarefied Gases, Princeton Aeronautical Paperback, Princeton University Press, Princeton, New Jersey, 1961.

40. Brooks, W.B. and Reis, G.E., "Drag on a Right Circular Cylinder in Rarefied Flow at Low Speed Ratios," SCR-518, Sandia Corporation, Albuquerque, New Mexico, 1962.

41. Allen, H.S., "The Motion of a Sphere in a Viscous Fluid," Phil. Mag., Ser. 5, Vol. 50, 1900, pp. 323-338, 519-534.

42. Arnold, H.D., "Limitations Imposed by Slip and Inertia Terms upon Stokes' Law for the Motion of Spheres through Liquids," Phil. Mag., Ser. 6, Vol. 22, 1911, pp. 755-775.

43. Wieselsberger, C., "Weitere Feststellungen über die Gesetze des Flüssigkeits-und Luftwiderstandes," Z. Physik, Vol. 23, 1922, pp. 219-224.

44. Bacon, D.L. and Reid, E.G., "The Resistance of Spheres in Wind Tunnels and in Air," NACA Rept. 185, 1923.

45. Liebster, H. and Schiller, L., "Kinematographische Messungen der Fallbewegung von Kugeln in zäher Flüssigkeit, auch in nächster Nähe einer Wand," Physik Z., Vol. 25, 1924, pp. 670-672.

46. Lunnon, R.G., "Fluid Resistance to Moving Spheres," Proc. Roy. Soc. (London), Ser. A, Vol. 110, 1926, pp. 302-326.

47. Flachsbart, O., "Neue Untersuchungen über den Luftwiderstand von Kugeln," Z. Physik, Vol. 28, 1927, pp. 461-468.

48. Schmiedel, J., "Experimentelle Untersuchungen über die Fallbewegung von Kugeln und Scheiben in reibenden Flüssigkeiten," Physik Z., Vol. 29, 1928, pp. 593-610.

49. Millikan, C.B. and Klein, A.L., "The Effect of Turbulence: An Investigation of Maximum Lift Coefficient and Turbulence in Wind Tunnels and in Flight," Aircraft Eng., Vol. 5, 1933, pp. 169-174.

50. Oseen, C.W., "Uber den Gultigkeitsbereich der Stokesschen Widerstandsformel," Ark. Mat. Astr. Fys., Vol. 9, No.16, 1913, pp. 1-15.

51. Fuchs, N.A., The Mechanics of Aerosols, Pergamon Press Limited, Oxford, England, 1964, p. 33.

52. Putnam, A., "Integrable Form of Droplet Drag Coefficient," ARS J, Vol. 31, 1961, pp. 1467-1468.

53. Schiller, L. and Nauman, A., "Über die grundlegenden Berechnungen bie der Schwerkraftaufbereitung," Z. Deut. Ing., Vol. 77, 1933, pp. 318-320.

54. Langmuir, I., "Mathematical Investigation of Water Droplet Trajectories," Report RL-225, General Electric Company, Schenectady, New York, 1944.

55. Dryden, H.L., Schubauer, G.B., Mock, W.C., Jr., and Skramstad, H.K., "Measurements of Intensity and Scale of Wind Tunnel Turbulence and their Relation to the Critical Reynolds Number of Spheres," NACA Rept. 581, 1937.

56. Taylor, G.I., "Statistical Theory of Turbulence V Effect of Turbulence on a Boundary Layer. Theoretical Discussion of Relationship between Scale of Turbulence and Critical Resistance of Spheres," Proc. Roy. Soc. (London), Ser. A, Vol. 156, 1936, pp. 307-317.

57. Schlichting H., Boundary Layer Theory, 4th ed., McGraw-Hill Book Company, Inc., New York, 1960, p. 537.

58. Delany, N.K. and Sorensen, N.E., "Low Speed Drag of Cylinders of Various Shapes," NACA TN 3038, 1953.

59. Schubauer, G.B. and Dryden, H.L., "The Effect of Turbulence on the Drag of Flat Plates," NACA Rept. 546, 1935.

60. Hegge Zijnen, B.G. van der, "Heat Transfer from Horizontal Cylinders to a Turbulent Air Flow," Appl. Sci. Res., Sec. A, Vol. 7, 1958, pp. 205-223.

61. Hinze, J.O., Turbulence, McGraw-Hill Book Company, Inc., New York, 1959, p. 559.

62. Ahlborn, F., "Turbulenz und Mechanismus des Widerstandes an Kugeln und Zylindern," Z. Tech. Physik, Vol. 12, 1931, pp. 483-491.

63. Hoerner, S.F., Fluid-Dynamic Drag, published by the author, Midland Park, New Jersey, 1958, Chapt. 3, 15, 16.

64. Kuethe, A.M. and Schetzer, J.D., Foundations of Aerodynamics, John Wiley and Sons Inc., New York, 1959, 2nd ed., p. 204.

65. Goin, K.L. and Lawrence, W.R., "Subsonic Drag of Spheres at Reynolds Numbers from 200 to 10,000," AIAA J., Vol. 6, 1968, pp. 961-962.

66. Schaaf, S.A., "Recent Progress in Rarefied Gasdynamics," ARS J., Vol. 30, 1960, pp. 443-447.

67. Millikan, R.A., "The General Law of Fall of a Small Spherical Body Through a Gas, and its Bearing upon the Nature of Molecular Reflection from Surfaces," Phys. Rev., Vol. 22, 1923, pp. 1-23.

68. Kane, E.D., "Sphere Drag Data at Supersonic Speeds and Low Reynolds Numbers," J. Aeronaut. Sci., Vol. 18, 1951, pp. 259-270.

69. Aroesty, J., "Sphere Drag in a Low-Density Supersonic Flow," Proceedings on the Third International Symposium on Rarefied Gas Dynamics, Paris, 1962, pp. 261-277.

70. Skreekarth, A.K., "Drag Measurement on Circular Cylinders and Spheres in a Highly Rarefied Gas Stream at a Mach Number of Two," ARS J., Vol. 32, 1962, pp. 748-754.

71. May, A. and Witt, W.R., "Free Flight Determination of the Drag Coefficient of Spheres," J. Aeronaut. Sci., Vol. 20, 1953, pp. 635-638.

72. Ashkenas, H., "Low-Density Sphere Drag with Equilibrium and Nonequilibrium Wall Temperature," Proceedings of the Third International Symposium of Rarefied Gas Dynamics, Paris, 1962, pp. 278-290.

73. Crowe, C.T., "Drag Coefficient of Particles in a Rocket Nozzle," AIAA J., Vol. 5, 1967, pp. 1021-1022.

74. Sivier, K.R., "Magnetic Field Properties Related to the Design of a One-Component Magnetic Support-and-Balance System," NASA CR-1352, 1969.

75. Sivier, K.R. and Henderson, M., "One Component, Magnetic Support and Balance System for Wind Tunnel Models," NASA CR-1353, 1969.

76. Franzen, W., "Generation of Uniform Magnetic Fields by Means of Air-Core Coils," Rev. Sci. Instr., Vol. 33, 1962, pp. 933-938.

77. Roshko, A., "On the Development of Turbulent Wakes from Vortex Streets," NACA Rept. 1191, 1954.

78. Kolmogoroff, A.N., "The Local Structure of Turbulence in Incompressible Viscous Fluid for Very Large Reynolds Numbers," Compt. Rend. Acad. Sci., URSS, Vol. 30, 1941, pp. 301-305.

79. Sato, H., "Experimental Study of the Spectrum of Isotropic Turbulence, II," J. Phys. Soc. Japan, Vol. 7, 1952, pp. 392-396.

80. Liepmann, H.W., Laufer, J., and Liepmann, K., "On the Spectrum of Isotropic Turbulence," NACA TN 2473, 1951.

81. Kármán, Th. von, "Progress on the Statistical Theory of Turbulence," Proceedings of the National Academy of Science, U.S., Vol. 34, 1948, pp. 530-540.

NASA-Langley, 1970 —— 12 E-5516